DECADAL HINDCAST OF HYDRODYNAMICS AND BARRIER ISLAND MORPHOLOGY

by

CARALINE R. MILLER

(Under the Direction of Matthew V. Bilskie)

ABSTRACT

Storm surge poses a major risk in the northern Gulf of Mexico, causing inundation and erosion of low-lying barrier islands. This reduces the flood protection that barrier islands provide to the mainland. Hydrodynamics and morphology were simulated at Dauphin Island, Alabama, and Petit Bois Island, Mississippi, between 2005 and 2020. Tropical cyclone-driven hydrodynamics were simulated using ADCIRC+SWAN. Then, storm-induced morphological changes and natural recovery were simulated using XBEACH and EDGR process-based morphologic models. The resulting elevation was used for the following storm simulation. Averaged across all storms, differences at the mainland were 2.2 and 0.9 cm, and differences near the islands were 1.2 and 6.4 cm. The maximum difference in peak wave height was 84.1 cm greater at the barrier islands than the mainland. Understanding how using different representations of barrier island morphology impacts simulated hydrodynamics can help improve engineering design and restoration planning on the mainland and the islands.

INDEX WORDS: Tropical Cyclones, Storm Surge, Barrier Islands, Morphology

DECADAL HINDCAST OF HYDRODYNAMICS AND BARRIER ISLAND MORPHOLOGY

by

CARALINE R. MILLER

BS, TULANE UNIVERSITY, 2021

A Thesis Submitted to the Graduate Faculty of The University of Georgia in Partial Fulfillment of the Requirements for the Degree

MASTER OF SCIENCE

ATHENS, GEORGIA

2023

DECADAL HINDCAST OF HYDRODYNAMICS AND BARRIER ISLAND MORPHOLOGY

by

CARALINE R. MILLER

Major Professor:	MATTHEW V. BILSKIE
Committee:	DAVINA L. PASSERI
	DAVID E. STOOKSBURY

Electronic Version Approved:

Ron Walcott
Vice Provost for Graduate Education and Dean of the Graduate School
The University of Georgia
December 2023

DEDICATION

Primarily, this one is for me. From moving across the country, settling into a new home, entering a new field, and never having opened MATLAB less than two years ago, to earning an MS in Engineering, I’m proud of the work I’ve done. Of course, this would not have been possible without the support of my family (chosen family included). I appreciate you all showing compassion when times were tough, and celebrating with me when things went well. Thank you to my parents for being proud of my achievements, even though you maybe don’t fully understand what this degree is about or what all the words in the title mean. Thank you to my sister Annabel for reminding me that I’m still cool, even though she’s definitely the cool sibling. Thank you to the Dunbar family for welcoming me as part of the family, and keeping me humble. And thank you to my partner Kolbi for the love, support, hours of being my sole audience member when I practice presentations, and for being my biggest fan.

ACKNOWLEDGEMENTS

I'd like to thank my advisor, Dr. Matthew Bilskie, for taking a chance on an ecology major and believing in me and my abilities throughout my two years at UGA. I'm so lucky to have had a supportive advisor who always pushes me to be my best self academically, professionally, and personally. Dr. Davina Passeri of USGS has also offered incredible support, and without the many hours she spent running morphological models this work would not have been possible. I appreciate the contributions of Dr. David Stooksbury as a member of my committee. I also want to thank Dr. Lizzie King for keeping me in touch with my passions and introducing me to some new ones.

I am endlessly grateful for the friendship and support of my lab mates in the COAST Lab and all of IRIS, especially Becca, Lina, Bobby, Oscar, Ada, Nashid, Adi, Sheppard, Hunter, and Alex. You all made the COAST Lab the most fun, tight-knit, and academically supportive lab I could have asked for. Becca deserves an extra shout-out for raving about the COAST Lab before I joinedand for being my closest friend and "work wife" here at UGA. I'll miss y'all and I can't wait to see where our careers take us.

This work was funded by NOAA's National Centers for Coastal Ocean Science Competitive Research Program and Research under award NA20NOS4780193 and completed in collaboration with USGS.

TABLE OF CONTENTS

Page

CHAPTER

APPENDICES

LIST OF TABLES

LIST OF FIGURES

CHAPTER 1

INTRODUCTION

Storm surge, often due to tropical cyclones (TCs), is one of the deadliest natural disasters globally, causing about 2.6 million casualties over the past ~200 years (Needham et al., 2015). Low-lying coastal cities are particularly at risk of storm surge-induced inundation because of their large population size and density, and extensive infrastructure (Lindsey, 2022; Mudd et al., 2014). Increasing coastal populations and urbanization in the United States (Kerr et al., 2013) puts more people and infrastructure at risk of being impacted by storm surges (Adams et al., 2010; Lindsey, 2022). Over time, storm surge magnitude (Wamsley et al., 2010) will increase nonlinearly due to increasing sea levels (Bilskie et al., 2016) and TC frequency (Davis et al., 2019; McTaggart-Cowan et al., 2007). Therefore, further research is necessary in order to protect communities, ecosystems, and infrastructure from storm surge-driven damage (Kerr et al., 2013).

Barrier islands are small islands that run parallel to the mainland. They provide numerous ecosystem services and socioeconomic benefits, such as attenuating wind waves, reducing storm surge during severe weather (Bilskie et al., 2016), and creating bays that act as nurseries for commercially valuable species (Miller-Way et al., 1996). During storm events, high-velocity water interacts with barrier islands, causing erosion, breaching, and inundation (Coogan et al., 2019). In the Northern Gulf of Mexico (NGOM), TCs are fairly common (Chen et al., 2008) and constitute a major driver of morphological change on low-lying barrier islands (Rosati & Stone, 2009). When the area and/or volume of barrier islands decreases, the islands’ ability to attenuate wave energy and surge also decreases (Dietrich, Westerink, et al., 2011). This reduces the amount of protection that these islands provide to the mainland, resulting in increased environmental and economic damage. As the area of barrier islands decreases due to erosion and sea level rise (SLR), hydrodynamics on the mainland may be affected (Bilskie et al., 2014). Including changes in barrier island morphology over time in hydrodynamic models may improve the accuracy of simulated peak water levels (Bilskie et al., 2014).

Including morphological changes to barrier islands in hydrodynamic models has implications in land development, infrastructure design, and restoration planning. Accurately modelling the magnitude and extent of storm surge-induced inundation allows practitioners to more effectively design homes, sea walls, levees, dune nourishment projects, and other coastal infrastructure. Engineers should understand the risk associated with the location of their design and account for the magnitude and frequency of storm surge impacts. For protective infrastructure, knowing the threat that must be protected against in the present and throughout the project's lifespan is necessary. Specifically, in the NGOM, knowing the level of storm surge that will occur under current and future morphological and SLR scenarios is crucial. Accounting for storm-driven morphological changes, and changes between TCs, may improve the results of long-term hindcasts.

This research addresses the following research objectives:

1. Do storm-driven morphological impacts to barrier islands affect mainland flood hazard?
2. Does simulating storm-driven morphological change and post-storm beach and dune recovery on barrier islands between tropical cyclones improve long-term hydrodynamic hindcasts?

CHAPTER 2

LITERATURE REVIEW

Storm Surge

Storm surge due to TCs and less severe storms can have devastating social, economic, and environmental impacts on coastal communities (Mudd et al., 2014; Needham et al., 2015; Resio et al., 2017). Storm surges are primarily caused by high winds and low pressure (S. Wang et al., 2008). These conditions push water toward the coast (Chen et al., 2008; Needham & Keim, 2011), increase the water surface elevation (WSE) (Resio & Irish, 2015; Sebastian et al., 2014), and can cause overland flooding (Brown et al., 2010; Bunya et al., 2010). Storm surge is “the phenomenon of rising coastal water levels due to the cumulative effect of processes such as wind-driven setup and currents, geostrophic effects, wave setup, wave runup and breaking, atmospheric pressure changes, precipitation (freshwater flooding), and astronomical tides” (Kerr et al., 2013). The high winds that cause storm surge also create larger than usual waves, exacerbating storm surge. When peak surge coincides with high tide, the water elevation is further increased.

Climate change causes SLR and increased air and water temperatures (Onea & Rusu, 2017), which contribute to increased storm surge risk (Kerr et al., 2013). TCs are predicted to become more frequent (Davis et al., 2019; McTaggart-Cowan et al., 2007) and intense in the future due to higher mean sea surface temperature (SST) (Mudd et al., 2014; Onea & Rusu, 2017). Higher intensity storms are characterized by greater wind speeds and central pressure deficits, which correlate to larger storm surges (Irish et al., 2009). Additionally, as mean sea level (MSL) increases due to SLR (Bilskie et al., 2014; Bilskie, Hagen, Alizad, et al., 2016; Lindsey, 2022; Taylor et al., 2015), storm surge magnitudes are expected to increase nonlinearly, at a faster rate than the base water level (Bilskie et al., 2016). In turn, these effects will have nonlinear feedbacks on barrier island morphology, resulting in increased dune erosion, overwash and breaching (Passeri, Bilskie, et al., 2018; Passeri et al., 2020).

Physical Processes

Hurricanes are characterized by maximum sustained wind speed of at least 119 km/h (74 mph) (*Saffir-Simpson Hurricane Wind Scale*, 2012), resulting in severe storm surge. Storm surge can also occur during less severe TCs or minor storms. Sebastian et al. (2014) found that a 15% increase in wind speeds causes a 23±3% increase in storm surge height, indicating a positive, nonlinear relationship between wind speed and storm surge.

Storm surge is most directly determined by the long-term sustained wind speed of a TC rather than the wind speed at landfall; wind speeds at or immediately before landfall may differ than the longer-term sustained wind speed, leading to inaccurate storm surge predictions (Needham & Keim, 2011). For example, Hurricane Katrina (2005) reached a Category 5 on the Saffir-Simpson Hurricane Wind Scale, then rapidly decreased in intensity to a Category 3 as the storm approached the Gulf Coast (Chen et al., 2008; McTaggart-Cowan et al., 2007). Due to the rapid deintensification and the use of these immediately pre-landfall wind speeds to predict storm surge, storm surge was massively under-predicted (McTaggart-Cowan et al., 2007). The maximum storm surge of approximately 8.5 m observed during Hurricane Katrina (2005) more closely reflects the expected magnitude of a storm surge resulting from a Category 5 hurricane, rather than a Category 3 (Needham & Keim, 2011). Similarly, rapid intensification of a storm as it approaches landfall does not always increase storm surge because winds need time to build up force on a water body to significantly raise WSE (Needham & Keim, 2011).

Storm surge magnitude is impacted by the speed at which a TC as a whole approaches land, referred to as forward speed (Needham & Keim, 2011). Storms with slower forward speeds produce greater storm surge because strong winds act on the same area of water for a longer duration, exerting more force on the water and increasing WSE. Similarly, larger TCs tend to produce higher storm surges because they sustain high wind speeds for a longer duration and over a larger area than smaller radius storms (Needham & Keim, 2011). The greater fetch of larger storms increases wave height during severe weather events, further increasing peak water levels (Musinguzi et al., 2022). In the absence of obstructions such as barrier islands, fetches are maximized and more effectively increase wave and storm surge height (Bilskie, Hagen, Alizad, et al., 2016).

The counterclockwise rotation of TCs in the northern hemisphere causes greater storm surge and wave heights on the right side of the eye (Hope et al., 2013; Irish et al., 2009) because the winds here are moving shoreward, and away from the shore on the left side of the storm (Chen et al., 2008; Needham & Keim, 2011). This phenomenon was observed during Hurricane Katrina (2005) in Bay St. Louis, Mississippi (Chen et al., 2008), which experienced higher WSE than in western Louisiana because of its location to the east of the storm path. Forward speed of the TC contributes to storm surge on both sides of the eye, though the winds blowing in the offshore direction to the left of the eye partially counteract this force (Needham & Kiem, 2011).

Studies have found positive linear relationships between storm surge height and TC central pressure deficit (Mudd et al., 2014; Resio et al., 2013); the lack of force exerted downward by atmospheric pressure allows the water to rise more easily in the presence of high winds (Bunya et al., 2010; Cid et al., 2014). The low central pressure of TCs increase storm surge magnitudes by approximately 1 cm per millibar of pressure (Welander, 1961). Storm surge attributed to low pressure alone for Hurricane Camille (1969), which had a record-high central pressure deficit of 108 millibars, was 1.08 meters (Needham & Keim, 2011). This accounted for a tangible proportion, approximately 14%, of the total 7.5-meter surge height (Needham & Keim, 2011).

TC intensity, often quantified by wind speed (*National Hurricane Center*, 2022; *Saffir-Simpson Hurricane Wind Scale*, 2012) or central pressure deficit (Resio et al., 2013; Taylor et al., 2015) is affected by short-term changes in climate (Cid et al., 2014) such as El Niño and is expected to increase due to long-term climate change (Cid et al., 2014; Mudd et al., 2014; Resio & Irish, 2015). Global warming due to climate change is predicted to increase SST. Mudd et al. (2014) found a significant increase in hurricane intensity when increases in SST alone were considered, though "the scientific community's understanding is still developing as to how relative changes in SST will affect overall intensity and tropical cyclogenesis". When TCs have higher intensity and a greater pressure deficit, the maximum potential storm surge height increases (Irish et al., 2009; Needham & Keim, 2011). Therefore, storm surge magnitudes are expected to increase as climate change and sea surface warming progress (Mudd et al., 2014; Resio & Irish, 2015). Additionally, severe TC frequency is predicted to increase in the future in the Gulf of Mexico (GOM) (Resio & Irish, 2015), in part due to increased SST, further increasing storm surge risk in coastal communities.

Geographic Influences

Geographic factors, such as the bathymetry of the continental shelf, the shape of the coastline, and the presence of barrier islands or other obstructions, impact storm surge height

(Needham & Keim, 2011). Storm surge is mitigated by obstructions such as barrier islands (Bilskie et al., 2014; Bilskie, Hagen, Alizad, et al., 2016; Needham & Keim, 2011; Sebastian et al., 2014), built infrastructure (Needham & Keim, 2011), and coastal wetlands (Akbar et al., 2017; Wamsley et al., 2010), which restrict shoreward water movement. Simulations of Hurricane Ike (2008) show that the height and volume of surge are greater at points on the mainland not sheltered by barrier islands compared to those sheltered by barrier islands because the islands caused the water to "pile up" on their seaward side (Sebastian et al., 2014). When these barrier islands have higher dune elevations, they can better protect the mainland from storm surge because they experience less overtopping (Bilskie, Hagen, Alizad, et al., 2016). Barrier islands also decrease the effective fetch acting on the water (Bilskie, Hagen, Alizad, et al., 2016), which decreases the storm surge magnitude on the mainland, as storm surge is a primarily wind-driven process (S. Wang et al., 2008).

Aside from protection from storm surge, barrier islands also attenuate wave height and force (Dietrich, Westerink, et al., 2011), which is especially beneficial during severe weather because waves are also wind-driven (Swain, 1997) and add to storm surge magnitude (Bunya et al., 2010; Dietrich, Tanaka, et al., 2011). When barrier islands are breached, such as Dauphin Island during Hurricane Katrina (2005) (Morton, 2008), they offer less protection from waves and storm surge, resulting in greater marsh erosion, damage to fisheries, and greater inundation on the mainland (Alizad et al., 2018; Passeri, Hagen, Medeiros, et al., 2015). While provide these benefits to the mainland, they must bear the brunt of the storm surge with minimal protection.

Built (grey) infrastructure, such as levees and floodgates, and nature-based (green) infrastructure such as barrier islands, wetlands, dunes, and oyster reefs, slow and/or block water when storm surge occurs (Alizad et al., 2018; Dietrich, Westerink, et al., 2011; Passeri et al., 2021). Built features can help attenuate storm surge on a local scale by blocking certain inlets or areas of shoreline and directing water elsewhere (Resio & Irish, 2015; Vuik et al., 2016), while nature-based features attenuate storm surge (Bunya et al., 2010) by increasing bottom friction, increasing wind drag (Akbar et al., 2017; Alizad et al., 2018; Dietrich, Westerink, et al., 2011), decreasing the effective fetch (Bilskie et al., 2016), and attenuating wave height (Alizad et al., 2018; Bunya et al., 2010). When grey infrastructure is used, storm surge often reaches peak heights against levees and other structures (Westerink et al., 2008). For example, the New Orleans area levee system impedes flow and causes localized ponding during surge events, altering hydrodynamics but not always reducing storm surge or inundation height (Westerink et al., 2008).

When barrier islands, oyster reefs, or coastal wetlands are present, the area of open water decreases; this decreases the fetch that acts on the water, lessening storm surge (Costanza et al., 2008). Bottom friction is higher on landforms such as beaches, marshes, and other vegetation compared to open water (Arcement & Schneider, 1989). This decreases storm surge by increasing the about of force that must be exerted on the water surface to produce a given WSE (Resio & Westerink, 2008; Vuik et al., 2016). For example, the barrier islands near Galveston Bay, Texas, reduced surge magnitudes by about 1 meter, and significant wave heights by about 5 meters, on the mainland during Hurricane Ike (2008) (Sebastian et al., 2014). For marshes, simulations show that 1 m of storm surge can be attenuated for between 14.5-20 km of marsh (Alizad et al., 2018); during Hurricane Andrew (1992), 4.7 cm of storm surge were attenuated for every km of marsh (Costanza et al., 2008), equivalent to 1 m of attenuation for every 21.3 km of marsh. In addition to increasing the base water level, SLR contributes to a decrease in land area and wetland productivity, reducing the surge attenuation potential of barrier island systems, causing positive nonlinear relationships between SLR and storm surge (Smith et al., 2010).

Needham & Keim (2011) explain that in shallow areas, deep water currents cannot carry away excess water, causing the WSE to increase due to the influx of excess water. For steeply sloping continental shelves, the approaching TC spends relatively little time above shallow water, therefore storm surge has a lower magnitude compared to slightly sloped continental shelves. When the continental shelf has a smaller (flatter) slope, an approaching TC reaches the transition between deep and shallow water farther from the coast, and therefore spends more time above a shallow water region (Figure 2.1) (Chen et al., 2008). Figure 2.1 suggests that the relatively flat, shallow bathymetry beneath Hurricane Katrina (2005) contributed to its high surge heights.

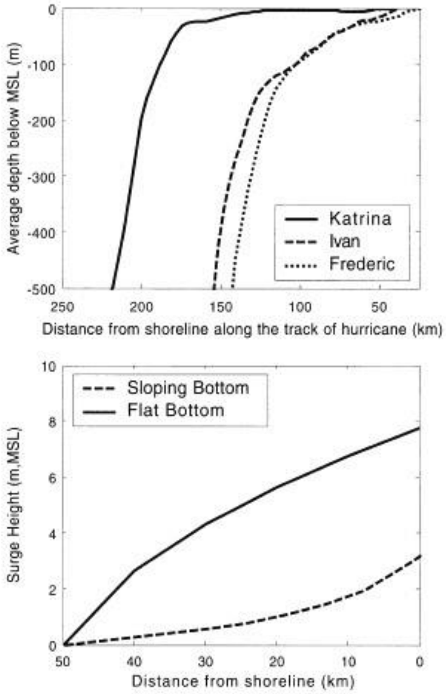

Fig. 16 Averaged topographic profiles along the paths of Katrina, Ivan, and Frederic (*top*) and the storm-surge profiles over a shallow flat seabed and a sloping continental shelf (*bottom*)

Figure 2.1: Water depth versus the distance from shore for Hurricanes Katrina (2005), Ivan (2004), and Frederic (1979) (top) and the surge height compared to distance from shore for flat and sloping bathymetry (bottom) (Chen et al., 2008).

This is shown by Chen et al. (2008), who simulated a synthetic Hurricane Katrina-strength TC that followed the track of Hurricane Frederic (1979) and made landfall near Mobile Bay, Alabama rather than New Orleans, Louisiana. The abandoned deltaic flats surrounding Mississippi River Delta, where Hurricane Katrina (2005) made landfall, are slightly sloped, while Mobile Bay has a comparatively steep continental shelf. Hurricane Katrina (2005) resulted in an 8.53 m peak storm surge (Needham et al., 2015) while the synthetic storm with the same wind speed, forward speed, and radius, that made landfall in Alabama resulted in a maximum storm surge of 6.5 m at the head of Mobile Bay, Alabama (Chen et al., 2008). Storm surge estimates for this synthetic storm reach as low as four meters lower than the modelled surge for Hurricane Katrina (2005) (Chen et al., 2008). Although differences in coastal geometry and the presence of barrier islands and obstructions likely contributed to this difference (Needham & Keim, 2011), the bathymetry likely played a major role (Chen et al., 2008).

Wider and more homogenous continental shelves and estuaries tend to have lower storm surge than narrower ones because there is more potential for water to move parallel to the shore rather than toward the shore (Chen et al., 2008). For example, the greater New Orleans area has a very complex coastline with numerous lakes, inlets, and wetlands, which restricts longshore flow and contributes to greater storm surge (Westerink et al., 2008) such as that observed during Hurricane Katrina (2005) (Chen et al., 2008). In contrast, Mobile Bay, Alabama has minimal nearby flow restrictions; Chen et al. (2008) simulated a synthetic, Katrina-strength storm that followed Hurricane Frederic's (1979) path and observed lower storm surge magnitudes than were observed during Hurricane Katrina (2005).

Storm Surge on the NGOM Coast

The Mississippi and Alabama coast is located in the NGOM, which experiences the highest storm surge magnitudes in the western North Atlantic and the second highest frequency of both high-magnitude (≥5 m) and low-magnitude (≥1 m) surges globally (Needham et al., 2015). This is due to a combination of having a high frequency of TCs (Chen et al., 2008), and wide and gently sloping continental shelves (Luettich et al., 2013). Because TC genesis requires warm SST (Needham & Kiem, 2011), the subtropical location of the NGOM is conducive to hurricanes and tropical storms; severe TCs typically occur several times a year in this region (*National Hurricane Center*, 2022). Both the intensity and frequency of TCs are expected to increase in the future due to climate change (Resio & Irish, 2015), consequently increasing storm surge frequency and magnitude (Bilskie, Hagen, Alizad, et al., 2016).

The shallow bathymetry of the GOM, particularly near the outlet of the Mississippi River, causes high storm surge magnitudes on the NGOM coast (Chen et al., 2008; Resio & Westerink, 2008). The GOM is characterized by a relatively flat continental shelf, with a shallow water region that extends far from the coast in most places (Chen et al., 2008). Specifically, the eastern portion of the NGOM (Alabama and the Florida panhandle) have much more steeply sloping continental shelves than the western portion (Mississippi, Louisiana, and Texas) (Chen et al., 2008). The GOM is relatively large and contains few islands and obstructions; these conditions allow powerful winds with large fetches (Bilskie, Hagen, Alizad, et al., 2016). Because storm surge and wind speed are positively correlated (Sebastian et al., 2014), these conditions often result in high storm surge magnitudes.

Storm surge has particularly devastating effects on the NGOM coast because of the low-lying, flat topography (Resio & Irish, 2015). The southeastern US is characterized by slightly sloping shorelines (Doran et al., 2017), with low-gradient beaches and wetlands separating the land from the sea (S. Wang et al., 2008). This causes more devastating coastal flooding due to wind-driven surge (Bunya et al., 2010) compared to if a surge of the same magnitude impacted a shoreline with a greater slope (Chen et al., 2008). Relative SLR is also higher than global averages in the NGOM due to subsidence (Lindsey, 2022), which raises the base sea level and consequently the storm surge magnitude (Smith et al., 2010). Under SLR, barrier island erosion and the rate of overall morphological change are expected to increase (Gutierrez et al., 2011; Irish et al., 2010). The reduction in area and elevation of barrier islands will change the flow path of water during extreme events, and reduce the amount of surge that the islands are able to attenuate. During extreme events, this leads to an increase in peak surge that is greater than the level of SLR by up to 80% on the mainland and in bays behind the barrier islands (Bilskie et al., 2014).

The increase in surge magnitude and frequency caused by SLR will accelerate barrier island erosion (Gutierrez et al., 2011), causing a nonlinear increase in the magnitude of storm surge that the islands, and the mainland behind the islands, will experience. This is further exacerbated by marsh degradation and a decrease in marsh area attributable to SLR; with less marshland, the inland area is less protected from storm surge (Alizad et al., 2018). These phenomena result in a positive, nonlinear relationship between SLR and storm surge height, where increases in storm surge magnitude exceed the increase in sea level (Bilskie et al., 2014; Bilskie, Hagen, Alizad, et al., 2016; Resio & Irish, 2015).

Summary & Further Research

Storm surge is a wind-driven, temporary increase in sea level above the astronomic tides during extreme weather (Kerr et al., 2013). Surge magnitudes tend to increase in magnitude as wind speeds, central pressure deficit, and storm radius increase (Resio et al., 2013; Sebastian et al., 2014). Storm surges can cause major flooding in coastal areas, particularly in low-lying coastal regions such as the NGOM coast (Dullaart et al., 2020). Their heights and extents vary with storm radius, intensity, forward speed, and landfall location (Chen et al., 2008; Needham & Keim, 2011). The nearshore bathymetry influences storm surge height on a more local scale, with shallow, open water causing the greatest storm surge magnitudes (Bilskie, Hagen, Alizad, et al., 2016; Chen et al., 2008; Needham & Keim, 2011). Storm surge has particularly severe impacts on the NGOM coast because of the gently sloping continental shelf and low-lying topography (Bilskie et al., 2014; Bilskie, Hagen, Alizad, et al., 2016; Resio & Westerink, 2008). In the NGOM, TC frequency and intensity are predicted to increase due to climate change (Mudd et al., 2014), along with storm surge (Resio & Irish, 2015). Together with urbanization, marsh degradation, barrier island erosion, and SLR impacting the region, it is likely that storm surge severity and frequency will increase in the future. These increased sea levels, and intensified storm surges under SLR, will cause further barrier island erosion (Plant et al., 2016). Therefore, it is important to understand, study, and model storm surge, particularly along the Mississippi and Alabama coasts.

While advances in understanding and modelling storm surge have been made in the past decades, further improvement and research is needed. Modelling storm surge on and around complex coastlines, wetlands, and islands continues to have relatively high error (Westerink et al., 2008). This model error has been diminished due to increased mesh resolution and computational efficiency (Bilskie, Hagen, Medeiros, et al., 2016), but can still be improved upon. Forecasting storm surge magnitude, extent, and timing in real-time during storm events also has high error, and grave implications for inaccurate predictions (Resio et al., 2017). Accounting for nonlinear impacts of climate change on TC and storm surge inundation frequency and magnitude is a developing field. While general trends between SLR, SST, and storm surge/TC activity have been established (Mudd et al., 2014), localized impacts should be further studied.

Barrier Island Morphology

Barrier islands are long, narrow islands that run parallel to the coast of the mainland. Barrier islands provide multiple ecological, environmental, economic, and social benefits to the mainland, bays, and sounds that they protect, in addition to ecosystems on the island themselves. Barrier islands reduce the fetch of wind that acts on the open water, reducing the potential magnitude of wind-driven surge that the mainland behind the islands experience (Bilskie, Hagen, Alizad, et al., 2016). In addition, barrier islands alter the flow path of storm surge nearshore (Bilskie et al., 2014). A study by Sebastian et al. (2014) found that barrier islands reduced the conveyance of the forerunner into Galveston Bay because the islands caused the surge to “pile up” on their seaward side. Because barrier islands often absorb much of the wave and surge energy during TCs, they tend to have high rates of sediment transport and erosion (Goff et al., 2010), making them highly dynamic. As islands change in size, elevation, and location, their protective abilities change in magnitude and location (Bilskie et al., 2014).

Increasing coastal populations and urbanization in the United States (Kerr et al., 2013) puts more people and infrastructure at risk of being impacted by storm surges (Adams et al., 2010). Barrier islands’ abilities to protect against storm surges and waves (Hope et al., 2013) make them an important form of natural infrastructure that protects the coast. Breaches, inundation, and erosion, often resulting from TCs and other extreme weather, reduce barrier islands’ protective abilities (Bilskie et al., 2014). Climate change and SLR will likely accelerate the rate of morphological change (Plant et al., 2016), likely increasing storm surge magnitudes on the mainland in the future.

Using numerical models to resolve nearshore hydrodynamics has improved substantially in recent years, though simulations in areas with barrier islands can be improved upon. For example, smaller barrier islands are occasionally ignored due to computational limitations (Bilskie et al., 2015). ADCIRC cannot model sediment transport (Akbar et al., 2017), and ADCIRC nor ADCIRC+SWAN can model coastal morphology (Sebastian et al., 2014), meaning that changes to topography, bathymetry, and coastal morphology must be either neglected, or loosely coupled based on observed data or the results of other models (e.g. Delft3D) (Passeri et al., 2020). The potential implications of barrier island morphology under climate change and SLR, coupled with the relatively poor ability to model hydrodynamics on and around barrier islands, necessitates further study of barrier islands using numerical models.

History of NGOM Barrier Island Morphology

Coogan et al. (2019) describe Dauphin Island as a low-lying (average elevation of 2-3 m), narrow (100-1800 m wide), micro-tidal barrier island in the NGOM. This area is geologically complex, with spatially variable barrier island types, and is characterized by frequent TC activity (Rosati & Stone, 2009). The low elevations of the barrier islands along the coasts of Louisiana, Mississippi, and Alabama make them particularly susceptible to storm surge-induced inundation and breaching during extreme events (Coogan et al., 2019; Resio & Irish, 2015). In general, the NGOM coast is sediment-starved and is slowly subsiding at a rate of up to 10-15 mm/yr (Coogan et al., 2019). Although morphological changes are more rapid and visible during extreme conditions, gradual morphological change occurs during quiescent periods between major storm events. Passeri et al. (2016) conducted a thorough study of the effects of SLR on tidal hydrodynamics and barrier island morphology in the NGOM. The Mississippi/Alabama coast is characterized by diurnal, microtidal tide action (Seim et al., 1987). They found that the tides at Grand Bay (Figure 2.2) are ebb-dominant, meaning the net morphological effect is seaward sediment transport. This is causing erosion in marshes along the northern coast of Grand Bay (Jenkins et al., 2023). In contrast, the tides at Weeks Bay are flood-dominant, bringing sediment toward the mainland. Fair weather waves cause minimal morphological change, as the average wave height is approximately 0.5 meters (Seim et al., 1987).

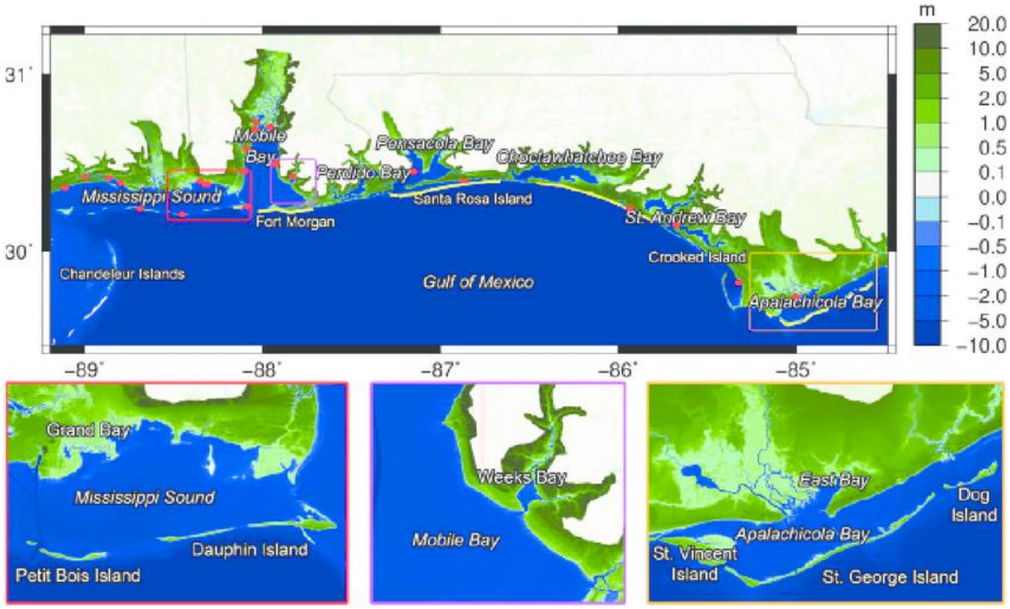

Figure 2.2: Map of Grand Bay and Weeks Bay (in red and purple boxes, respectively) relative to the Gulf coast (Passeri et al., 2016)

Barrier islands along the MS and AL coasts have been consistently migrating westward for at least the past 175 years (Morton, 2008; Passeri et al., 2016). The westernmost points of Dauphin and Petit Bois Islands have migrated west at a rate of 55.3 m/yr and 34.5 m/yr, respectively, for the period between 1848-1986 (Rosati & Stone, 2009). The eastern end of Dauphin Island, AL, is more stable than the less-developed western portion of the island; because of the relative stability of the east side of the island and the westward migration trend, the island is elongating over time (Rosati & Stone, 2009). Dauphin Island breached during

Hurricane Katrina (2005) (Morton, 2008), and is now more susceptible to overwash and inundation in this area (Coogan et al., 2019). Petit Bois Island, Mississippi is experiencing a net loss of land area at a rate of approximately 2.0 hectares per year (Byrnes et al., 1991). Simultaneously, central Petit Bois Island is accumulating sediment from offshore sources (Rosati & Stone, 2009). Overall, barrier islands on coastal MS and AL are highly dynamic, particularly during storm events; even in fair weather, they are consistently migrating westward and changing in area and shape.

Response to Extreme Conditions

Hurricanes are considered a dominant driver of morphological change on barrier islands (Rosati & Stone, 2009). Breaching and sediment transport on and around barrier islands are accelerated when they experience highly energetic conditions. Breaching that may occur during storms reduces the protection that the mainland and back bays receive, increasing potential for erosion and increased wave heights and water levels (Bilskie et al., 2014).

A case study of the effects of Hurricane Nate (2017) on Dauphin Island, Alabama analyzed inundation and overwash on the island (Coogan et al., 2019). During Hurricane Katrina (2005), Dauphin Island was breached; in 2011 following the Deepwater Horizon Oil Spill, a rock wall barrier was placed across the breach to promote accretion. Coogan et al. (2019) found that the area surrounding this breach experienced the most overwash during Hurricane Nate (2017). 66% of the island experienced some degree of overwash; about half of the area that experienced overwash had overwash fans, which were largely caused by low-elevation gaps in the dune used for driveways (Coogan et al., 2019). Every island transect studied experienced a net loss of sediment, though sediment deposition was observed on the roads on the eastern portion of the island. Much of the sand that eroded from the foredune is hypothesized to have been transported offshore. Hurricane Nate (2017) was a relatively weak Category 1 hurricane, therefore other TCs can be expected to have similar, if not more severe, morphological outcomes.

Storm Surge

Barrier islands absorb and attenuate much of the energy of oncoming storm surges, resulting in complex hydrodynamic and morphological processes (Alizad et al., 2018; Dietrich, Westerink, et al., 2011). The elevation of the island relative to the storm surge magnitude tends to dictate the barrier island’s response to the surge (Rosati & Stone, 2009). The dune height on the barrier island helps decrease surge behind the island, while surge tends to cause erosion (Sallenger, 2000), creating a feedback between morphological and hydrodynamic processes if the dune does not have sufficient time to recover prior to the next surge event. Bilskie et al (2016) analyzed Choctawhatchee Bay under various SLR conditions, and found that when primary dune height near the Bay’s inlet was reduced by about 3 m, there was a “drastic increase” in surge within the Bay. Including changes in land elevation over time such as this alters simulated storm surge magnitude, whereas a static model would often underpredict peak water levels (Bilskie et al., 2014). In addition to the force of the water on the foredune, barrier islands can also experience surge from the bay side of the island when ponding occurs after storm events (Passeri, Bilskie, et al., 2018; Passeri, Long, et al., 2018).

Waves

Though storm surge is the primary driver of morphological change, waves also cause morphological change, especially during periods of increased water elevations (Rosati & Stone, 2009). During extreme events, the NGOM coast can experience very high wave heights, such as up to 15 meters observed during Hurricane Gustav (2008) (Dietrich, Westerink, et al., 2011). In order for sediment to become mobilized, a combination of sufficiently high water elevations and powerful waves is necessary (Rosati & Stone, 2009); TC-induced storm surge typically provides these conditions that are conducive to morphological change. Storm surge often leads to inundation and breaching, which can lead to propagation of larger waves (Alizad et al., 2018) and further sediment transport and morphological change.

Morphological Responses to Climate Change

Climate change is associated with SLR, higher SST (Onea & Rusu, 2017), and increased TC frequency and intensity (Davis et al., 2019; McTaggart-Cowan et al., 2007). SLR alone poses a threat to low-lying land since the base water level is increased, and accretion rates often cannot keep pace with the rate of SLR (Plant et al., 2016). Bilskie et al. (2014) state that it is "only intuitive" that SLR will accelerate shoreline and barrier island morphological change. These changes are exacerbated by landscape changes caused by SLR, such as marsh drowning (Day et al., 1995) or flooding of jetties or other infrastructure, which increase the potential fetch (Bilskie, Hagen, Alizad, et al., 2016), and reduce bottom friction and wave attenuation abilities of the islands (Bilskie et al., 2014). Anthropogenic changes to the landscape such as development and creation of wave-breaking infrastructure can exacerbate, or reduce, these effects. In addition to the effects of SLR alone, the increase in TC frequency and intensity increases the storm surge risk that the islands experience since severe surges will increase in magnitude and occur more often (McTaggart-Cowan et al., 2007).

Numerical Modelling

Due to the complex physics of nearshore hydrodynamics, numerical models are often needed to accurately predict water levels, especially during severe weather or along complex coastlines. Even when using numerical models, there are many variables that must be manipulated and input correctly to accurately define the physical system and predict water levels

(Bunya et al., 2010). Model accuracy tends to decrease when modelling highly energetic conditions during extreme events (Rusu et al., 2008); complex wind fields and high-energy conditions associated with TCs makes modelling water levels near the coast especially challenging during TCs (Swain, 1997). It is important to note that numerical models represent the most complete knowledge of hydrodynamic processes at the time they are made, and may not include all of the involved variables in actual hydrodynamic processes.

ADCIRC+SWAN

The ADvanced CIRCulation (ADCIRC) hydrodynamic model solves the shallow water equations in either two- or three-dimensions (Luettich, 2018). ADCIRC can be paired with the Simulating WAves Nearshore (SWAN) model to simulate nearshore wind-generated waves. ADCIRC+SWAN is well-suited to simulate water elevations and wave activity during both fair weather and extreme conditions such as TCs (Hope et al., 2013; Luettich, 2018). Both the uncoupled ADCIRC and the coupled ADCIRC+SWAN models are sufficient for representing hydrodynamic processes (Luettich et al., 2013). Using ADCIRC and ADCIRC+SWAN to model hydrodynamic conditions caused by severe weather and TCs is common practice, though it presents several challenges.

Model outputs such as sea level, wave height and period, and storm surge depend heavily on the quality of the meteorological inputs such as wind and barometric pressure (Menendez et al., 2014). Poor meteorological inputs are often a primary source of error in storm surge modelling (Weaver & Luettich, 2010). Model performance typically decreases when high-energy peak winds occur (Kerr et al., 2013; Onea & Rusu, 2017) because the physical system responds differently to fair-weather versus highly energetic conditions (Rusu et al., 2008). Therefore, it is important to use high-quality, thoroughly validated, and high-resolution data for optimal model performance, especially during extreme conditions (Menendez et al., 2014).

Due to their low annual exceedance probabilities and small sample size, TC hindcast studies often have high uncertainty (Resio et al., 2009). In order to decrease uncertainty and increase sample size, many researchers utilize include synthetic storms. Synthetic storms can be created using theoretical meteorological forcing values, often based on actual storm data, in order to study alternative situations (e.g. Chen et al., 2008; Irish et al., 2009). This allows researchers to study how specific variables such as wind speed, storm size, landfall location, etc. impact model outputs (Irish et al., 2009). Synthetic storms can also be used to create hypothetical future storms by incorporating meteorological changes due to climate change such as, anticipated morphological changes such as shoreline location or bathymetry (Bilskie et al., 2014), or SLR (Taylor et al., 2015). The efficiency of numerical models allows many simulations to be completed in a relatively short amount of time (e.g., Sebastian et al., 2014).

Long-Term Hindcasts

Hindcasts can be used to help validate numerical models by simulating a previous storm or time period with thorough data with the model, and comparing model results to observed conditions. These hindcasts can be as short as the duration of one hurricane (e.g. Kerr et al., 2013) and span up to several decades (e.g. Sotillo et al., 2005). Known meteorological data (e.g. winds, barometric pressure) are input into the model, then the model outputs (e.g. wave height, water level, peak storm surge time, etc.) are compared to real-time observations such as those by the National Data Buoy Center (NDBC). The model is then calibrated as needed until the observed and modeled results show good agreement; then, the model is considered accurate and can be used for similar observed or synthetic events. Often, the model must be iteratively calibrated and validated several times to achieve optimal agreement. Long-term hindcasts can yield accurate results; for a long-term wave height hindcast in the Black Sea, ADCIRC+SWAN achieved an R^2 of 0.92, a 0.12-meter bias, and a 0.36 SI between observed and modelled values (Akpınar & Bingölbali, 2016). Hindcasts can only be validated using variables with observational data during the event. However, proxies for variables that were not directly measured can also yield adequate validation and/or error statistics (Kirk et al., 2022).

Accuracy of Model Outputs

Many studies report fairly accurate model results for both uncoupled and coupled ADCIRC(+SWAN) models. Typically, these studies use Root Mean Squared Error (RMSE), R^2, normalized bias (MN Bias), and/or scatter index (SI) to quantify model error. Discrepancies between observed and modelled data may occur due to inaccurate input data or poor mesh resolution (Akbar et al., 2017; Brown et al., 2010), or due to inaccurate observations. The accuracy of model predictions for different variables (e.g. water levels, wave height, wave period) varies with wind intensity; for example, S. Wang et al. (2008) found that peak wind speed and surge height were underestimated as conditions become more energetic.

Water Levels

Accurate water level predictions can be achieved (Dietrich, Tanaka, et al., 2011; Y. Wang et al., 2018) in both deep and shallow water (Dietrich et al., 2013) and during severe weather (Kerr et al., 2013). Hope et al. (2013) found good agreement between ADCIRC+SWAN results and observed water level data, with an $R^2 > 0.9$, an SI of 0.1463, and an MN Bias of -0.0114 meters.

Despite challenges for highly energetic systems, ADCIRC+SWAN is an accurate predictor of hydrodynamic conditions during severe weather. ADCIRC has been shown to simulate both peak and lower-magnitude storm surges with fairly low bias (Resio et al., 2017; Westerink et al., 2008). Kerr et al. (2013) accurately modelled peak storm surge for hurricanes Ike (2008) and Rita (2005) using ADCIRC+SWAN, though other studies (Cid et al., 2014; Davis et al., 2019; S. Wang et al., 2008) found that storm surge was underestimated during extreme events. For example, Davis et al. (2019) found an RMSE <0.5 meters, and still considered the results “acceptable”. For peak water levels during four hurricanes, a separate study found R^2 values that ranged from 0.77-0.93 (Dietrich, Tanaka, et al., 2011). Westerink et al. (2008) used ADCIRC to hindcast storm surge during hurricanes Betsy (1965) and Andrew (1992); for Hurricane Betsy, the mean error was 0.58 meters, and for Andrew it was 0.29 meters (0.43 and 0.27 meters without outliers, respectively). Predicting peak surge timing using ADCIRC+SWAN can be improved upon (Akbar et al., 2017; Y. Wang et al., 2018). In some cases, storm surge magnitude may be accurately predicted, but the timing of the peak surge may be incorrect due to a combination of factors, such as improper bottom friction or hydraulic conductivity estimates nearshore (Akbar et al., 2017).

Wave Characteristics

Waves are a major contributor to total water levels, accounting for up to 30% of the surge in localized areas during TCs such as Hurricane Isabel (2003) (Weaver & Luettich, 2010). Therefore, it is important to evaluate model performance for wave height in both fair-weather and severe conditions. ADCIRC cannot model short waves; pairing ADCIRC with a nearshore wave model such as SWAN can increase the accuracy of the model, particularly in coastal areas most effected by wind waves (Musinguzi et al., 2022). Oftentimes, neglecting short waves can lead to underestimation of WSE (Musinguzi et al., 2022).

During high wind conditions, ADCIRC(+SWAN) studies report varying accuracy and bias for wave height outputs. Onea & Rusu (2017) found that ADCIRC+SWAN tends to underestimate peak wave heights for waves experiencing highly energetic conditions (Rusu et al., 2008). On the other hand, Kerr et al. (2013) found that coupled hydrodynamic circulation models that include waves (e.g. ADCIRC+SWAN) tend to overpredict water levels. Another study determined that an uncoupled ADCIRC model slightly underestimated storm surge and wave height for Hurricane Irma (2017), but still produced fairly accurate results; a coupled ADCIRC+SWAN model performed better for the same initial conditions, partially because of the explicit inclusion of waves (Musinguzi et al., 2022). ADCIRC+ SWAN can also accurately model significant wave height in complex estuaries and wetlands such as the Biloxi Marsh (Hope et al., 2013). For high frequency waves, ADCIRC+SWAN is a fairly accurate model, estimating frequencies over 0.35 Hz correctly in a study by Björkqvist et al. (2019). Despite conflicting findings of over- and underestimation of wave heights and water levels, the literature reports that ADCIRC+SWAN is an accurate and efficient model to predict waves during TCs (Dietrich et al., 2013), and has been frequently used for this purpose (Davis et al., 2019; Hope et al., 2013).

Limitations during Extreme Conditions

Modeling waves and sea level during extreme events accurately is highly dependent on the quality of the meteorological forcings (Menendez et al., 2014). Meteorological inputs must have high spatial and temporal resolution in order to detect and include rapidly developing, short duration, or small storms (S. Wang et al., 2008). Using data at the smallest available spatial and temporal scales, especially near complex or rapidly changing features such as barrier islands, steep coastlines, or estuaries, results in the best model outputs (Cid et al., 2014). However, low quality and temporal resolution of input wind data is a common issue for hydrodynamic models that should be addressed (Onea & Rusu, 2017). The downside to using finer spatial and temporal scales is the increase in necessary computational power to run the simulation; to avoid this, researchers often use unstructured meshes.

Calibration and validation of model outputs is also difficult during extreme weather because data collection instruments may be damaged or malfunction due to the high winds and energetic conditions (Hope et al., 2013). For example, some meteorological gauges were lost and destroyed during Hurricane Katrina in 2005 (*National Data Buoy Center*, 2023), necessitating replacement and strengthening of these buoys in order to improve data quality and quantity, especially during severe weather (Hope et al., 2013). Despite these challenges, using numerical models is a practical way to study these large-scale, relatively infrequent, events.

Model Forcings & Inputs

Wind is a primary driver of waves and storm surge (Bunya et al., 2010), and is an important ADCIRC+SWAN input for modelling storm surge and water levels during severe weather. Wind and barometric pressure, which are closely related, are the most important variables to consider when studying storm surge (Irish et al., 2009). Use of finer-resolution meteorological forcings during storms results in a better representation of both wind fields and storm surges (Dullaart et al., 2020). For small-radius or rapidly forming TCs, and during early TC genesis, high-resolution wind fields are especially important because of the relatively small spatial and temporal scale at which wind speed and direction change (Dullaart et al., 2020). The quality of observed and reanalysis wind data is consistently improving (Hersbach et al., 2020; Olauson, 2018), although further improving wind fields' spatial and temporal resolution would help improve storm surge hindcasts (Dietrich et al., 2013).

Reanalyses are “datasets devoted to reproduce past atmospheric fields as accurately as possible” (Menendez et al., 2014), and are some of the most widely used datasets for climate research (Buizza et al., 2018). Reanalyses combine observed data and thoroughly validated models to provide estimated climatic conditions on small spatial and temporal scales (Menendez et al., 2014; Valmassoi et al., 2022). Observed wind data is collected by remote sensing and on-site gauges periodically at many locations globally; reanalysis datasets are created by interpolating between these known points in space and time, creating consistent “maps without gaps” (Hersbach et al., 2020). A benefit of reanalysis data includes its potential to be used over long time scales (Menendez et al., 2014) and in places with limited on-site observations (Valmassoi et al., 2022). Reanalysis wind products are ideal for places with inconsistent data collection, both spatially and temporally, because of the detailed interpolation between points in space and time, as well as the consistency and long temporal records of past wind data available via reanalysis (Olauson, 2018).

Continuous efforts have been made to increase the reliability, accuracy, and resolution of reanalysis meteorological products since their conception (Bunya et al., 2010). Due to constant improvements to interpolation methods, remote sensing measurement accuracy, and the increased presence of tide gauges and buoys, reanalyses have become a very reliable source for large-scale meteorological data. Reanalysis products such as European Re-Analysis 5 (ERA5) undergo extensive calibration & validation based on buoy measurements, weather stations, and other in-situ measurement methods (Björkqvist et al., 2019; Bunya et al., 2010) prior to their official release to the public (Hersbach et al., 2020). Despite using the best available data and technology, actual wind speeds are generally higher than reanalysis predictions (Islek et al., 2021). The spatial resolution is not yet fine enough to resolve local variations, making reanalysis products an inadequate tool to estimate longer-term (months-years) average wind speeds (Olauson, 2018) and small spatial-scale events like TCs (Dullaart et al., 2020).

ERA5

ERA5 is a meteorological reanalysis dataset released by the European Centre of Medium-Range Weather Forecasts (ECMWF) and Copernicus, with a time range of 1950-present (Bell et al., 2021). ERA5 is a very accurate product, with significant improvements made over the five generations of ERA, including increased spatial and temporal resolution (Dullaart et al., 2020). Gaps in measured data are filled by short-term (9-hour) forecasts, which are archived in 1-hour time steps. The end of one nine-hour forecast is used as the starting point for the next; these forecasts are repeatedly verified with observed data and re-calibrated until sufficient agreement is reached between the observations and the forecasts (Hersbach et al., 2020). ERA5 and previous versions have been used globally to study long-term wind patterns (Hersbach et al., 2020; Menendez et al., 2014; Olauson, 2018), wave heights and patterns (Islek et al., 2021; Onea & Rusu, 2017), sea levels (Cid et al., 2014), and severe storms (Dullaart et al., 2020; S. Wang et al., 2008). However, ERA5 is not frequently used in the NGOM to model these variables, presenting an opportunity for further research using ERA5 to model TC-induced storm surge (Hersbach et al., 2020).

ERA5 better captures the large pressure deficits and strong winds of TCs (Dullaart et al., 2020) and has a lower SI (Hersbach et al., 2020) compared to previous ERA versions, making it a useful meteorological product to accurately model TCs and their resulting storm surge. For example, a study by Dullaart et al. (2019) studying storm surge magnitudes found that ERA5 yielded very good agreement for Hurricanes Irma (2017) and Florence (2018), but underestimated Hurricane Michael (2018). Because of its novelty, Hersbach et al. (2020)

recommend studying systematic errors between ERA5 and other datasets. For example, the Climate Forecast System Reanalysis (CFSR) dataset tends to cause greater predicted significant wave heights than similar ERA products (Islek et al., 2021). Despite these difficulties and its novelty, ERA5 is a sufficiently complete background wind dataset for TC simulations.

One shortcoming of ERA5, particularly when it is used to study highly spatially variable events such as TCs, is its coarse resolution; despite substantially improving compared to its prior versions (Hersbach et al., 2020), the 31 km spatial resolution and 1-hour timestep of ERA5 (Hersbach et al., 2019) are still insufficient to capture rapidly-forming, small, and/or fast-moving TCs (Bilskie et al., 2022). This can cause underestimations of wind speeds in the immediate vicinity of the storm track. Similarly, ERA5 resolution is often insufficient to capture the vortex pattern of TC winds (Dullaart et al., 2020). To improve wind fields immediately surrounding TCs, background wind fields like ERA5 can be supplemented with vortex models.

Bottom Friction

Bottom friction, also referred to as bottom roughness, represents the amount of drag that the sea floor or ground exerts on the water that passes over it, thereby decreasing the water’s energy. Bottom friction is often quantified by Manning’s n coefficient (Arcement & Schneider, 1989). Bottom friction changes rapidly as one approaches the coast (Dietrich, Tanaka, et al., 2011; Sebastian et al., 2014); deeper water experiences less bottom friction than shallow water areas with sand, marshes, rocks, or other uneven surfaces. Storm surge and water levels are impacted by bottom friction (Bilskie et al., 2014). Storm surge propagates faster and reaches higher magnitudes in areas with lower bottom friction, and in some cases, simulated peak surge timing is early (Akbar et al., 2017). In ADCIRC models, initial Manning’s n values at each node are typically based on land-cover definitions (Bunya et al., 2010). ADCIRC+SWAN models linearly interpolate Manning’s n values spatially, and compute a new bottom roughness at each time step (Dietrich et al., 2022; Hope et al., 2013; Luettich, 2018). Bottom friction has complex interactions with hydrodynamic flow, especially in shallower areas (Hope et al., 2013), making it important to have as thorough and accurate bottom friction data as possible (Cid et al., 2014).

Unstructured Meshes

Model performance depends on a number of factors including mesh resolution, coastline complexity, and water depth (Westerink et al., 2008). Meshes that have finer resolution near the coastline produce the most accurate predictions (Chen et al., 2008; Dietrich, Tanaka, et al., 2011; Dullaart et al., 2020; Irish et al., 2009; Resio et al., 2017; S. Wang et al., 2008). However, using very high mesh resolution throughout the model domain increases computational expense and time; unstructured meshes allow variable resolution across the study area, so that coarse resolution can be used in uniform regions, and finer resolution can be used in complex regions (Dullaart et al., 2020). This improves computational efficiency without sacrificing simulation accuracy.

Linear interpolation of elevation between nodes oversimplifies the coastline, causing coarse meshes to miss more coastal details such as small wetlands, inlets, or floodwalls and overpredict storm surge heights than fine meshes (Dietrich et al., 2013; Westerink et al., 2008). Errors in ADCIRC+SWAN predictions are typically due to poor meteorological input data (Weaver & Luettich, 2010) or excessively coarse mesh resolution (Dietrich et al., 2013). In less complex regions, such as deep, open water, a coarser mesh may be used and still yield accurate results (Björkqvist et al., 2019).

Bathymetry inputs are particularly important for studies that focus on wave breaking and storm surge magnitude (Dietrich, Tanaka, et al., 2011). As with most variables, finer spatial resolution of bathymetric data improves model accuracy (Dietrich, Tanaka, et al., 2011; Dullaart et al., 2020). Bathymetry typically changes rapidly between deep water and the coastline (Dietrich, Tanaka, et al., 2011). It is especially important to use finer mesh resolution in rapidly changing areas, while coarser resolution can be applied in the open ocean where changes are more gradual.

Hydrodynamic processes in areas with complex geometry are still not well-understood (Chen et al., 2008); nonuniformities such as barrier islands impact the magnitude and path of storm surge in ways that are still unpredictable to researchers (Bilskie et al., 2014). Therefore, models of areas with complicated shorelines tend to predict storm surge and waves less accurately than models with uniform coastlines (Menendez et al., 2014). Based on their ADCIRC+SWAN study, Bilskie et al. (2014) concluded that accurately representing small raised features such as dune crests is necessary to simulate storm surge flow paths accurately. Nearshore bathymetry can also alter model predictions of the path, pattern, and magnitude of coastal flooding (Bilskie, Hagen, Alizad, et al., 2016; Passeri, Hagen, Bilskie, et al., 2015). Ensuring proper representation of land elevation via adequately fine mesh resolution is crucial to accurately modelling coastal hydrodynamics.

Due to its highly complex coastline and unique bathymetry and storm surge patterns, the NGOM coast is considered one of the most challenging areas in the world to correctly model storm surge and flooding during severe storms (Westerink et al., 2008). Unstructured meshes are publicly available to be used in hydrodynamic models for locations globally, including the NGOM (Luettich, 2018). Kerr et al. (2013) report that in areas such as coastal Louisiana with a low topographic gradient, models are much more sensitive to wetting and drying. In areas like these, fine mesh resolution and high-resolution inputs should be used, and model definitions of ‘wet’ and ‘dry’ should be carefully calibrated and validated (Kerr et al., 2013).

Uncertainty in Models

Uncertainty in numerical modeling reflects the confidence of a researcher in their result, though the definition of uncertainty is subjective (Merz & Thieken, 2005). Zerger et al. (2002) state that, “uncertainty, in contrast to error, assumes no prior knowledge of data accuracy.” Model error represents a statistically quantifiable difference between an observed, or ‘true’, value and a predicted result. Historically, numerical modelers’ response has been to ignore uncertainty. This excludes valuable information and implies a greater degree of confidence and accuracy in the results of the model than actually exists (Zerger et al., 2002). Due to the nature of numerical models and the complexity of coastal hydrodynamic systems, it is impossible to eliminate uncertainty, and quantifying uncertainty is an inexact science.

Merz & Thieken (2005) describe two types of uncertainty: natural, derived from random variation in physical processes, and epistemic, caused by inadequacies of the model and incomplete knowledge of the study system. Quantifying natural uncertainty is relatively straightforward and involves determining the probability that a certain variable will reach a given value. This is often done by analyzing past behaviors of the variable of interest (Freer et al., 2013). For example, Niedoroda et al. (2010) considered tidal variation as part of their uncertainty measure. Due to the low return period of TCs, there is a low sample size to derive natural uncertainty statistics from for severe weather events at any one study location (Mousavi et al., 2011; Resio et al., 2013). For these low-probability, high-intensity events, uncertainty is even greater (Resio et al., 2013), increasing the need for transparency when communicating uncertainty estimates.

Natural uncertainty varies spatially and temporally. Quantifying natural uncertainty of wind speed or tidal range, for example, is highly site-specific. Spatial scale is important when considering TC return period for a specific area; Resio et al. (2013) recommend a study area no larger than 2x the radius to maximum wind speed (R_{max}) in width. Zerger et al. (2002) found that in a relatively flat area of Australia, flood risk uncertainty was greater than if the area were more topographically heterogeneous. Implications of human-driven climate change including SLR and TC intensification are other sources of natural uncertainty (Freer et al., 2013; Purvis et al., 2008). The climate change models used to obtain these predicted values have both natural and epistemic uncertainty, further increasing the uncertainty associated with these estimates. In general, natural uncertainty can be reduced by obtaining a higher resolution and/or a longer time period of observed data (Freer et al., 2013; Merz & Thieken, 2005; Purvis et al., 2008).

Model error is a major source of epistemic uncertainty. Systematic model errors are biases and inaccuracies that cause the model to behave predictably inaccurately. For example, models tend to overestimate storm surge in complex areas such as estuaries when the resolution is too coarse (Westerink et al., 2008), but underestimate both extreme wind speeds and very high storm surge (Onea & Rusu, 2017; S. Wang et al., 2008). Models also include simplifying assumptions that may skew predictions. For example, using fewer dimensions in models (e.g. 2D depth-averaged versus 3D models) increases uncertainty (Teng et al., 2017) since velocity is assumed constant throughout the water column. Bottom roughness is highly spatially and temporally variable (Freer et al., 2013), and difficult to obtain an exact measurement for. Other simplifications such as element-wide wet/dry algorithms (Purvis et al., 2008; Teng et al., 2017) and linear SLR effects (Taylor et al., 2015) increase the uncertainty associated with the model. Model uncertainty does not diminish over time since it is independent of forecast time, making it slightly simpler to quantify than other sources of epistemic uncertainty (Resio et al., 2017). Model errors, both random and systematic, can be reduced by increasing the number of observations and model runs (Mousavi et al., 2011; Resio et al., 2013) and improving the calibration and validation process. In addition, increasing spatial and temporal of the model can reduce uncertainty, though trade-offs with computational cost and readability limit the extent to which resolution can be improved (Mousavi et al., 2011; Purvis et al., 2008).

Epistemic uncertainty also includes the lack of knowledge of the physical system; quantifying this value is highly subjective. Swain (1997) noted: "Although the [ECMWF WAM] model represents the physics of the wave evolution in accordance with our knowledge today, there can be a number of potentially important effects which are not included in this model." Epistemic uncertainty can be decreased by increasing the duration for which you study a system (Merz & Thieken, 2005) since models tend to produce more accurate results when more data is used to verify and calibrate the model. Researchers often rely on archived data from long-standing organizations such as NOAA to obtain this data. However, many study areas are underrepresented in meteorological data collection and may lack reliable or thorough data that dates back far enough to meet the needs of the project (Menendez et al., 2014). When climate change is accounted for, nonlinear relationships between different (individually uncertain) variables increases the uncertainty associated with future climate estimates (Taylor et al., 2015).

Failure to account for uncertainty can have substantial social, economic, and environmental impacts, especially during TCs. Resio et al. (2013) found that failing to include uncertainty led to an underestimation of storm surge magnitudes by about 20% in the Gulf of Mexico. When the median or ‘most likely’ value is used for a key variable such as SLR, low-probability, high-intensity events may remain unaccounted for, underestimating future conditions

(Freer et al., 2013). Underestimating storm severity can lead to inadequate evacuation planning and infrastructure damage or failure (Zerger et al., 2002), resulting in financial, ecological, and cultural costs. Merz & Theieken (2005) suggest that conservative designs and courses of action are implemented when epistemic uncertainty is high. Explicitly quantifying and communicating uncertainty is crucial for decisionmakers and stakeholders' safety and wellbeing.

Quantifying Uncertainty

Methods for quantifying uncertainty vary throughout the literature. Generally, natural and epistemic uncertainty are calculated separately (Merz & Thieken, 2005) and are combined as one of the final steps in the process. When quantifying uncertainty, "the following steps should be considered: firstly, the sources of uncertainty are to be identified; secondly, uncertainty from different sources need to be quantified (or at least ranked qualitatively) and then prioritised" (Teng et al., 2017); the objective is to establish a probability distribution of potential values. In the hydrodynamic modelling literature, Bayesian, ensemble, and/or other statistical methods are often employed to quantify uncertainty.

Statistical and Bayesian Methods

Uncertainty can be implicitly communicated by presenting probabilistic (describing a range of possible values) rather than deterministic (communicating one most likely value) results. Resio et al. (2017) produced cumulative distribution functions (CDFs) for forecasted storm surge magnitudes. The CDF, f(x), represents the probability that a surge event with a magnitude less than or equal to x will occur. Several CDFs were created for each study location and forecast length. These five CDFs accounted for various uncertainty estimations: forecast error but no model error, forecast and model error, two times the sum of the forecast and model error, forecast and model error plus bias, and two times the sum of the forecast and model error plus bias. The CDF’s slope and maximum value depended on the uncertainty bound applied. The full range of the five CDFs was taken to represent the total uncertainty. The uncertainty decreased as the time before landfall decreased (i.e., the CDFs differed from each other more for the 96-hour forecast than for the 24-hour forecast). Though very simplistic, this method of uncertainty estimation yields more holistic results than a deterministic estimate would.

Using Bayesian methods to estimate uncertainty involves weighting then combining several probability distributions in order to best represent the range of potential values. Merz & Thieken (2005) employ this methodology to quantify the uncertainty of a flood frequency analysis, though the results are applicable to a wide range of topics. This study defines the output, flow volume, as a random variable with a set probability density (Merz & Thieken, 2005). By defining the variable as random, it can be represented by a probability distribution and therefore more easily analyzed. A probability distribution about the mean is then established based on observed data, simulation results, or some arbitrary distribution (e.g. Gaussian). This probability distribution is subjective, and “represents the analyst's degree of belief that the parameter has different values” (Merz & Thieken, 2005).

The ability of the analyst to choose the estimated probability distribution implicitly accounts for some uncertainty. Typically, probability distributions are obtained from several methodologies and/or analyses, then these distributions are weighted and combined to estimate the uncertainty of the given variable. Merz & Thieken point out that models are weighted either based on expert judgement or “by applying a measure of fit between model and observation”; when a particular model has a lower standard deviation or better fit, it is weighted more heavily. The weighted average of the probability distributions is used to represent this final range of potential values, and uncertainty values are derived from that distribution. Methods such as this are well-equipped to quantify natural uncertainty, but often fail to consider epistemic uncertainty, necessitating that they be expanded upon and/or combined with other quantification methods.

Ensemble Methods

Ensemble methods utilize a large number of slightly varied simulations of synthetic events to assess model uncertainty. Slight perturbations to storm characteristics such as central pressure deficit, angle of approach, and R_{max} are used to increase the number of predictions to analyze (e.g., (Niedoroda et al., 2010; Taylor et al., 2015; Teng et al., 2017; Zerger et al., 2002). By conducting multiple simulations of the same time period or event with slightly varied inputs, a range of potential model outcomes can be generated; this is especially useful for stochastic models that lack a predictable probability curve (Zerger et al., 2002). The range of outcomes are plotted and fitted with a probability distribution, from which it is relatively simple to derive uncertainty. Common ensemble methods for determining probabilistic storm surge estimates are Surge Response Functions (SRF), the Joint Probability Method (JPM), and a variation of this method, JPM-Optimal Sampling (JPM-OS).

SRFs are physics-based algebraic expressions of storm surge that are based on the shallow water equations and the results of many storm surge simulations (Taylor et al., 2015). Irish et al. (2009) used SRFs to estimate the maximum potential surge height at a particular location based on several parameters such as forward speed, storm radius, and angle of approach to land. Irish et al. (2009) represent this function with

$$\zeta(x, y) = \phi_{km}([x_o, y], [c_p, R_p], [x, y]) \tag{2.1}$$

"where ϕ_{km} is the dimensional surge response function for track angle k and forward speed m, c_p is the hurricane central pressure, and R_p is the hurricane pressure radius." The result of this function is a continuous probability density function (PDF), from which it is fairly simple to derive uncertainty. This SRF is based on 75 simulations with varied c_p and R_p. Surge estimations using the SRF presented in Equation 2.1 yielded highly accurate results, with RMSE <0.32 m for all SRF predictions when compared to ADCIRC simulations (Irish et al., 2009). By producing a continuous PDF, the probability of each of the full range of potential outcomes is easily interpreted, better informing uncertainty estimations compared to methods that yield a single deterministic value.

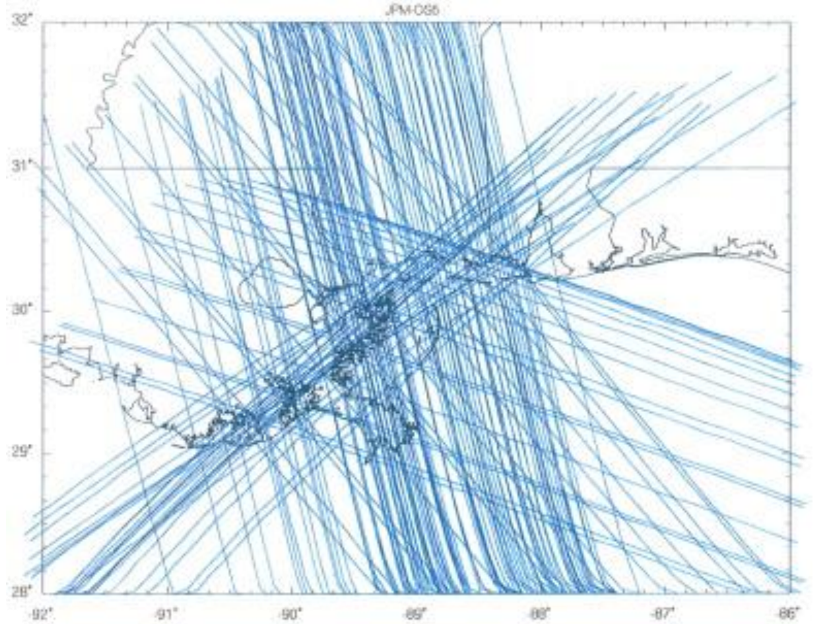

Figure 2.3: Synthetic storm tracks used for a JPM-OS study by Niederoda et al. (2010)

The JPM is the preferred surge hazard assessment method in the USA (Taylor et al., 2015) because of its statistical stability, though it comes with a high computational cost (Niedoroda et al., 2010). To reduce computational cost compared to JPM, JPM-OS was developed. JPM-OS reduces the number of synthetic storms that must be run by selecting a fraction of total possible storms to represent the 'true' results obtained from the full JPM results (Figure 2.3). Niedoroda et al. (2010) weighted each of these representative storms based on their distance from some coastal reference point. In this case, central pressure deficit, distance from the landfall location, and the storm radius were the main determinants of surge response. The model did not include tides or random variations in Holland b parameter, which were accounted for in the uncertainty function (Niedoroda et al., 2010).

Taylor et al. (2015) propose a modified JPM-OS that makes use of SRFs to reduce the number of simulations needed, and therefore the computational cost required. Inputs to SRFs include the storm's central pressure, R_{max}, forward velocity, and track angle, among others. The use of SRFs in addition to JPM-OS further increase epistemic uncertainty beyond what exists for JPM-OS alone because of the extra simplifying assumptions. Natural uncertainty is low for parts of this study because the field measurements used as inputs for the model are accurate and thorough, and no forecasts are involved. When SLR is introduced, uncertainty increases since future SLR is unknown. Taylor et al. (2015) assumed a normal distribution about the uncertainty, which is calculated by summing the standard deviation of major constituents:

$$\varepsilon_z^2 = \varepsilon_{tide}^2 + \varepsilon_{waves}^2 + \varepsilon_{winds}^2 + \varepsilon_{model}^2 + \varepsilon_{SRF}^2 + \varepsilon_{SLR}^2 + \varepsilon_{residual}^2 \qquad (2.2)$$

where ε_z is total epistemic uncertainty. Niedoroda et al. (2010) used a similar equation, accounting for slightly different variables. A total uncertainty value of 0.7 m is assumed for "tide, wave, wind, computational model, and residual sources" based on a prior study by Resio et al. (2013). This uncertainty quantification method is proposed because current approaches sum SLR and storm surge magnitudes, neglecting dynamic and non-linear feedbacks between sea level and storm surge. This method yields accurate results, with $R^2 \geq 0.73$ at all 73 open ocean locations measured, and $R^2 \geq 0.80$ at 84% of these locations. For bay locations measured, $R^2 \geq 0.70$ at 89% and $R^2 \geq 0.80$ at 26% of locations measured. Calculating the error of each variable and model simplification individually based on JPM-OS storm selection criteria then summing them proves to be an accurate method for quantifying uncertainty (Irish et al., 2011; Song et al., 2012).

Sensitivity analysis is a smaller-scale ensemble method that studies the effects of small perturbations to a simulation’s inputs on the simulation’s outputs (Zerger et al., 2002). Initial conditions, boundary conditions, or topography are typically manipulated (Teng et al., 2017). Sensitivity analyses can be conducted locally, where one variable at a time is perturbed by a small amount, or globally, where variables are simultaneously varied through their entire feasible range (Teng et al., 2017). Local sensitivity analysis can determine which variables impact the model most, especially in reference to a specific region or landform. On the other hand, a global sensitivity analysis is a relatively fast method to obtain the full potential range of modeled outcomes. Teng et al. (2017) emphasize that sensitivity analysis is an imperfect process, where different methods may lead to slightly different results.

Summary & Conclusion

As climate change increases the frequency and severity of TCs (Davis et al., 2019; McTaggart-Cowan et al., 2007; Resio & Irish, 2015) and causes further SLR (Onea & Rusu, 2017), storm surge risk is increasing nonlinearly (Bilskie et al., 2014; Kerr et al., 2013). Naturally occurring features such as barrier islands, coastal wetlands, and oyster reefs attenuate waves and reduce water elevations during surge events force (Dietrich, Westerink, et al., 2011), protecting the mainland from storm surge-induced inundation and damage (Sebastian et al., 2014). Barrier islands are highly dynamic systems (Cowell et al., 2003), susceptible to sediment transport and substantial morphological changes in relatively short periods of time (Rosati & Stone, 2009); this alters their protective capacity on decadal time scales.

Numerical models such as ADCIRC+SWAN are used to simulate hydrodynamic impacts during TCs by solving the shallow water equations and simulating nearshore wind waves (Luettich, 2018). ADCIRC+SWAN produces accurate results for peak water levels and wave heights under highly energetic conditions (Dietrich et al., 2013), including hurricanes (Davis et al., 2019). Numerical models have inherent uncertainty that can be reduced by increasing the amount and resolution of input data (Menendez et al., 2014; Onea & Rusu, 2017), conducting model calibration and validation, and by reducing the number of simplifying assumptions that are made (Teng et al., 2017). However, these improvements require both computational power and time that are often unavailable. Researchers typically fail to explicitly report uncertainty in their model results (Zerger et al., 2002), which can lead to a misinterpretation of data that can have potentially fatal outcomes in TC evacuation scenarios. Quantifying uncertainty is an inexact science that is often done by using statistical methods (e.g. Resio et al., 2017) and/or by estimating uncertainty of each individual variable then combining those uncertainty values (e.g. Taylor et al., 2015).

As TCs become more frequent and intense, it is increasingly important to study how TCs impact barrier island morphology and, consequently, their ability to protect the mainland from storm surge. Understanding the uncertainty of both hydrodynamic and morphological models that are used to predict morphological change is crucial for improving land management outcomes and clearly communicating results to stakeholders.

CHAPTER 3

METHODS

A 15-year ADCIRC+SWAN hindcast of TC activity in the NGOM between 2005-2020 was performed for Dauphin Island, Alabama and Petit Bois Island, Mississippi. The simulated ADCIRC+SWAN WSE and wave height, direction, and period were used as boundary conditions for simulations of storm-driven morphological change. An integrated modeling approach using three models was applied to simulate barrier island morphologic evolution at Dauphin and Petit Bois Islands during quiescent and storm periods. The resulting DEM was interpolated onto the NGOM-Real Time (NGOM-RT) ADCIRC+SWAN mesh for the next simulation. In addition to updating the DEM between runs, the hindcasted storms were also run on a Post-Ivan (2004) DEM (Seymour, 2020), and the most up-to-date LiDAR data available, both interpolated onto the Post-Ivan NGOM-RT mesh.

Storm Selection

The beginning of the study period was chosen to begin after Hurricane Ivan (2004), in part because of the detailed and accurate Post-Ivan DEM (Seymour, 2020). Storms were selected based on the following criteria: passed through a 200 km radius of Dauphin or Petit Bois Island; reached tropical storm status or higher; occurred between 2005-2020; has observed WSE data available at Dauphin Island (NOAA Station #8735180; Figure 3.1) for dates that coincide with the NHC best-track storm duration dates; and caused a tangible increase in WSE at NOAA Station #8735180. From these criteria, 10 storms were selected for inclusion in this study (Table 3.1).

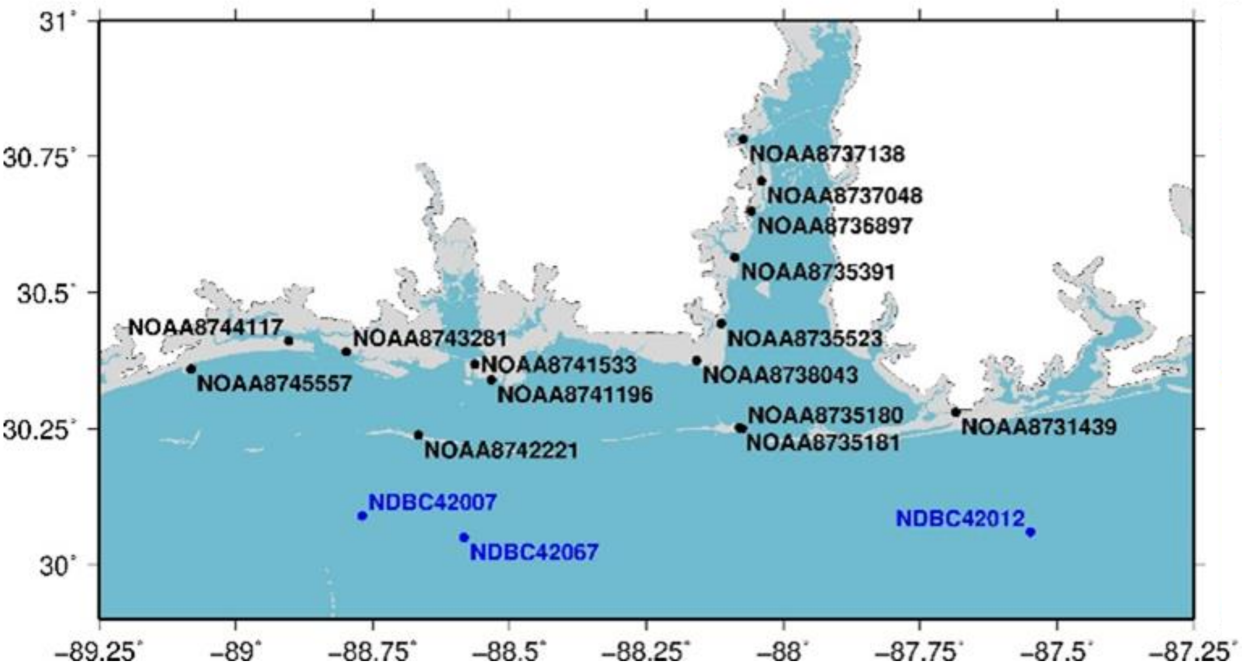

Figure 3.1: Locations of NOAA tide gauges (black) and NDBC buoy (blue) stations. NOAA Station #8735180 is located on eastern Dauphin Island.

#	Storm Name	Year	Classification	Date of NHC data extraction
1	Arlene	2005	Tropical Storm	Aug. 23, 2022
2	Cindy	2005	Cat. 1 Hurricane	Aug. 31, 2022
3	Dennis	2005	Cat. 4 Hurricane	Oct. 4, 2010
4	Katrina	2005	Cat. 5 Hurricane	Oct. 4, 2010
5	Ida	2009	Cat. 2 Hurricane	Jan. 13, 2010
6	Nate	2017	Cat. 1 Hurricane	Apr. 24, 2018
7	Alberto	2018	Tropical Storm	May 3, 2019
8	Gordon	2018	Tropical Storm	May 3, 2019
9	Cristobal	2020	Tropical Storm	May 24, 2021
10	Sally	2020	Cat. 2 Hurricane	May 24, 2021

Table 3.1: Selected storms & the dates that their best track data were obtained

Model Selection & Setup

ADCIRC+SWAN

Hydrodynamic models such as ADCIRC and SWAN are commonly used to model the complex physics of winds, waves, tides, and water levels in both fair weather and extreme conditions (Hope et al., 2013; Luettich, 2018). ADCIRC solves the shallow water equations in two dimensions using unstructured meshes that allow varied spatial resolution (Luettich, 2018). This study utilized the NGOM-RT unstructured mesh developed by Bilskie et al. (2020) (Figure 3.5). The ADCIRC model can predict storm surge, flooding, tides, and wind-driven circulation (Hope et al., 2013; Luettich, 2018). The coupled model, ADCIRC+SWAN, also accounts for nearshore waves (Dietrich et al., 2022), often leading to greater and more accurate WSE predictions than ADCIRC alone (Hope et al., 2013; Musinguzi et al., 2022). ADCIRC+SWAN has been shown to represent significant wave heights during storm conditions accurately (Hope et al., 2013).

This study used a two-dimensional ADCIRC+SWAN coupled hydrodynamic model of the NGOM to simulate WSE, significant wave height, wave period, and wave direction. ADCIRC+SWAN was run with a 1-second timestep, with advective terms included in the simulation. A 14-day spin-up was run for each storm, allowing the background wind field and the eight major tidal constituents (Q1, O1, P1, K1, N2, M2, S2, & K2) to reach a dynamic equilibrium before hot-starting the simulation at the start time of the NHC best-track. Wetting and drying were enabled.

Background wind speeds were obtained from ERA5 (Hersbach et al., 2020) via the Climate Data Store (Copernicus) website on April 1, 2022. ERA5 offers a 31km spatial resolution and 1-hour temporal resolution (Olauson, 2018). The generalized asymmetric Holland vortex model (GAHM) (Gao et al., 2018) was used to supplement ERA5 by creating a high-resolution cyclonic wind field along the NHC best track (Bilskie et al., 2022). GAHM wind forcing was used between the storm location along the NHC best track and 3 times R_{max} (Figure 3.2, inner circle). Only ERA5 was used beyond 12 times R_{max} away from the storm location (Figure 3.2, outer circle). Between $3R_{max}$ and $12R_{max}$ (Figure 3.2, middle circle) the wind was linearly interpolated for a smooth transition between GAHM and ERA5. Storm simulations using blended ERA5+GAHM wind fields have been shown to predict more accurate wind speeds, WSE, and wave heights than those with ERA5 alone (Bilskie et al., 2022).

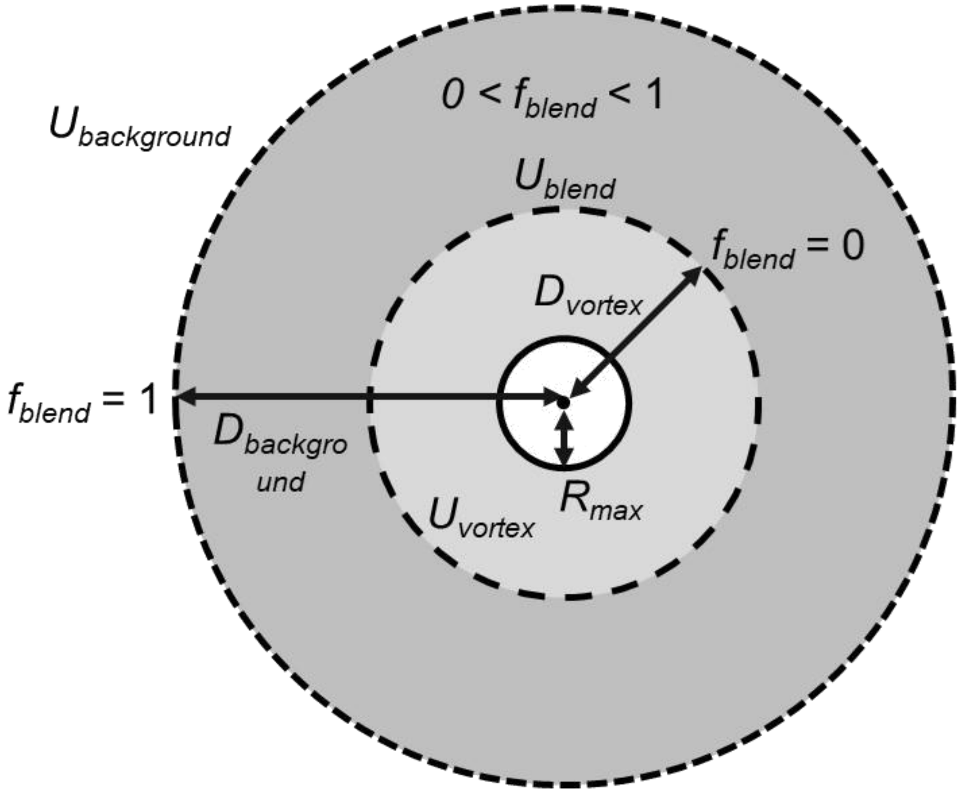

Figure 3.2: Wind blending schematic; outer circle represents ERA5, the inner circle represents GAHM, and the middle circle is the transition area (Bilskie et al., 2022).

Morphological Model: Storm Periods

XBeach was used to simulate beach and dune morphological change during TCs. XBeach is a two-dimensional, depth-averaged model that resolves coupled short wave energy, flow and infragravity wave propagation, sediment transport and bed level change (Roelvink et al. 2009). The code solves the nonlinear shallow water equations and incorporates time-varying wave action balance and roller energy balance. Sediment transport was simulated using a depth-averaged advection-diffusion equation (Galappatti & Vreugdenhil, 1985; Grzegorzewski et al., 2009). The model is capable of simulating morphologic change from the swash, collision, overwash and inundation storm-impact regimes (Sallenger, 2000). XBeach was run in surfbeat hydrostatic mode.

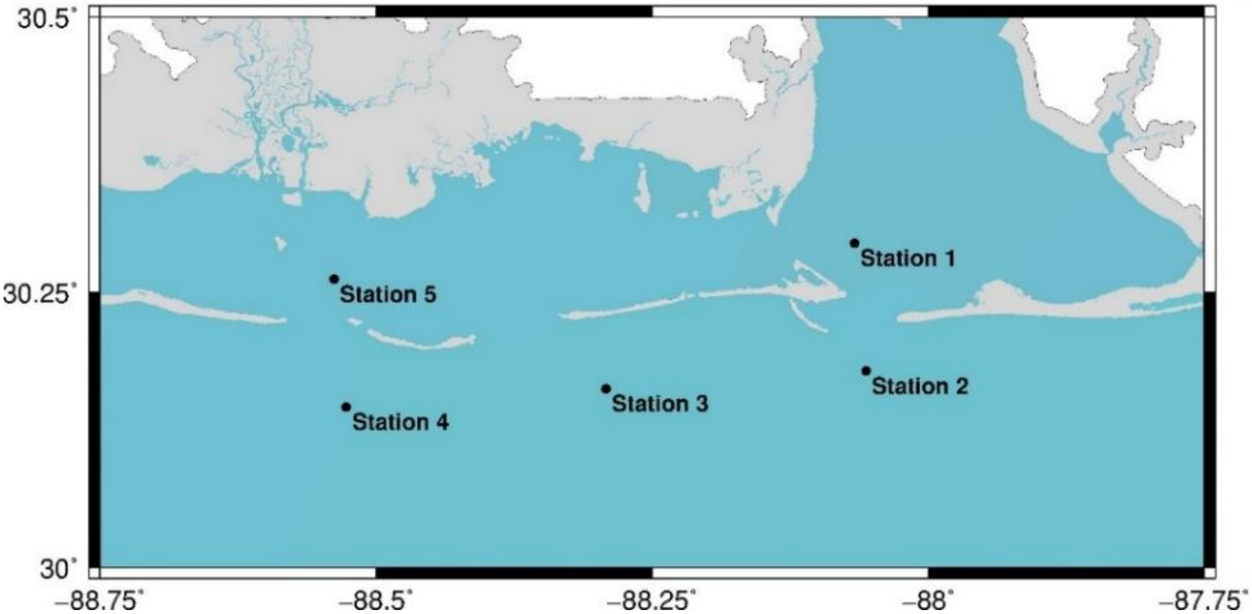

Figure 3.3: Locations where XBeach boundary conditions were input to the model.

The model domain spans from west of Petit Bois Island in Horn Island Pass to east of Dauphin Island in Mobile Inlet (Figure 3.4). The XBeach model domain was comprised of 3045 x 3024 cells and extends approximately 13km in the cross-shore and 45km in the alongshore (Frank-Gilchrist et al., 2023). Grid resolution varies from 3.5 m to 11 m in the cross-shore, and 15 m in the alongshore. The model was previously validated for hurricanes Ivan, Katrina and Sally (Frank-Gilchrist et al., 2023). For the decadal hindcast, the model was forced with hourly water levels forced at the four corners of the grid domain, and hourly wave conditions (peak period, mean direction, significant wave height) at the southern offshore boundary (Figure 3.3).

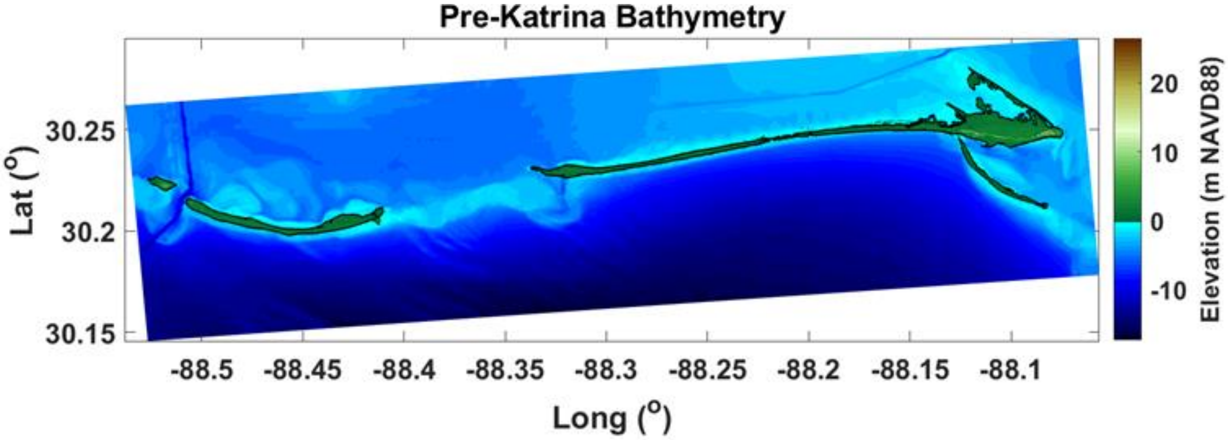

Figure 3.4: XBeach model domain

Morphological Models: Quiescent Periods

For quiescent periods, two empirical models were applied to simulate post-storm dune growth and shoreline change. A previously developed empirical dune growth (EDGR) model was applied to account for post-storm dune recovery. EDGR fit Gaussian curves to cross-shore profiles of the island to represent the island platform, dunes and berms. The model then evolved the foredune of each profile based on growth curves parameterized with observed LiDAR data (Dalyander et al., 2020). EDGR accounts for Aeolian transport without explicitly resolving the underlying physical processes in order to model dune formation and recovery during fair-weather conditions (Dalyander et al., 2020). EDGR was calibrated for each island using LiDAR data, and has produced reliable results with an average RMSE of 0.72 m from 2006-2015.

To resolve quiescent shoreline change, an empirical shoreline change (ESC) model was developed based on decadal shoreline change rates calculated from LiDAR data and previous morphological model simulations (Jenkins et al., 2020); the shoreline change rates were calculated at each of the EDGR cross-shore profiles. Compared to observations, ESC replicated shoreline change with an RSME of 25.91 m across the entirety of Dauphin Island; historic shoreline change rates at Petit Bois Island were not available. The ESC model was then applied to resolve the total shoreline change over each quiescent period at each island. Using the post-storm XBeach elevations as an initial condition, the two empirical models were run sequentially, with shoreline change resolved first and then dune growth for the entirety of the quiescent period. The resulting elevations were then passed back to ADCIRC+SWAN to be interpolated onto the NGOM-RT mesh (Figure 3.5) for the next storm simulation.

EDGR and ESC were not run between Hurricanes Cindy & Dennis (2005) because the NHC best track durations for these storms overlapped. For the period between Hurricanes Ida (2009) and Nate (2017), EDGR and ESC were run until May 2011, and then paused to alter the DEM to account for the installation of the rock wall in Katrina Cut of Dauphin Island in response to the Deepwater Horizon Oil Spill. The rock wall elevations were interpolated onto the DEM and the feature was considered non-erodible in XBeach. EDGR and ESC were then resumed to account for recovery from May 2011 to October 2017 at which point Hurricane Nate occurred. EDGR and ESC were not run after Hurricane Sally (2020) because Sally was the final storm of the study.

DEM Interpolation

ADCIRC+SWAN simulations utilized the unstructured NGOM-RT finite element mesh (Figure 3.5) for its high resolution and computational efficiency (Bilskie et al., 2020). The Post-Ivan DEM (Seymour, 2020), used data collected in 1998 and 2001, and data from the CONED model (1888-2013) for the background topobathy. Topography and nearshore bathymetry elevations for Dauphin and Petit Bois Islands were obtained from survey data collected in April-September 2004 by the USACE, and LiDAR data collected by the USGS and NASA in September 2004 (Seymour, 2020). The Post-Ivan DEM elevations were interpolated onto the NGOM-RT mesh using the cell area averaging (CAA) method (Bilskie et al., 2015). The default CAA value was multiplied by 3 for improved topographic smoothing.

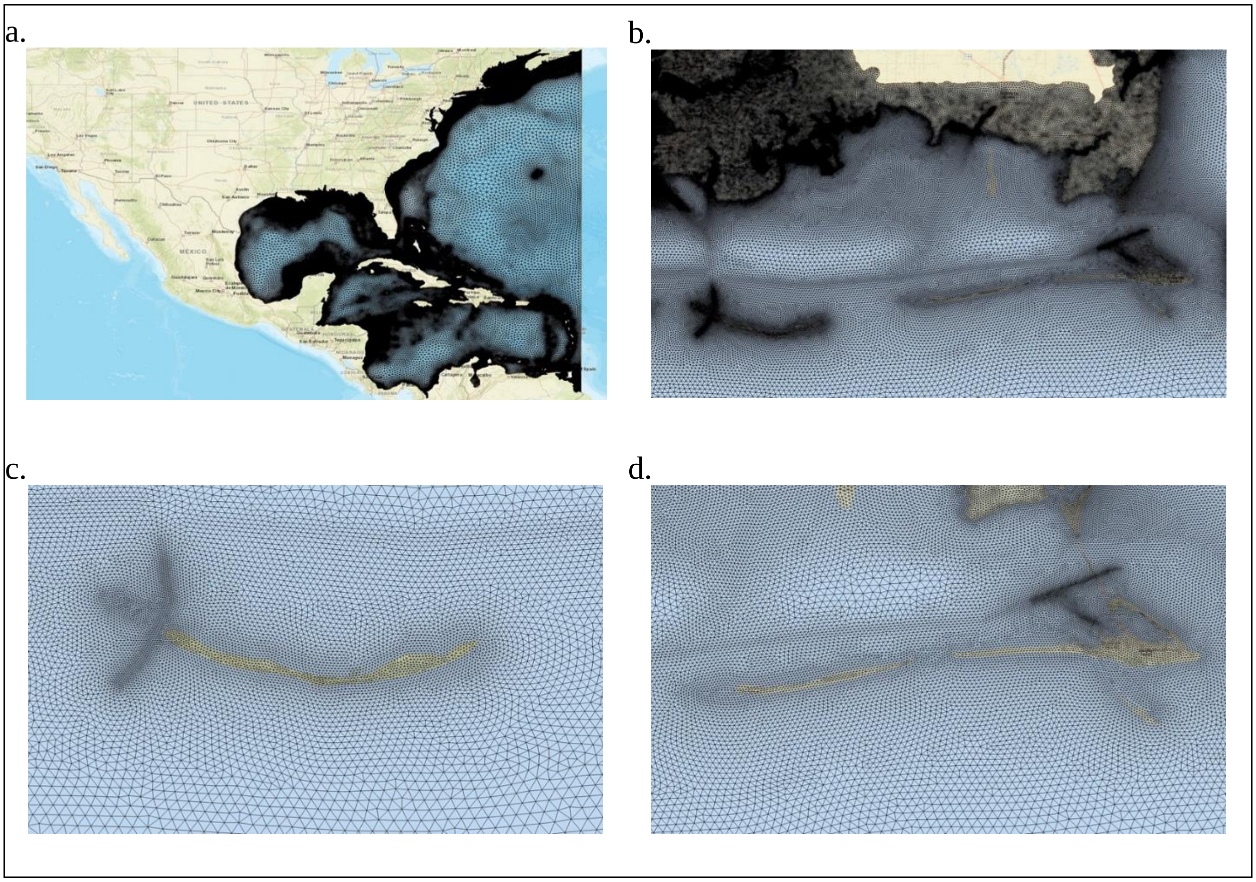

Figure 3.5: NGOM-RT Unstructured Mesh; a. full mesh domain, b. region of interest, c. Petit Bois Island, d. Dauphin Island.

The morphology simulations output topobathy data at 2.5-meter resolution. These outputs were then interpolated onto the Post-Ivan NGOM-RT mesh. Dauphin Island’s vertical features (Bilskie et al., 2015) were flagged to retain dune crest elevations. On Petit Bois Island, flagging vertical features was unnecessary because raised features that prohibit flow were large enough to be captured without being flagged as vertical features, and the lack of flagging did not cause significant elevation errors (Bilskie et al., 2015). This was partly because of the lack of man-made features on Petit Bois Island that are present on Dauphin Island, such as roads, that create drastic sub-mesh-scale elevation changes.

To make the ‘up-to-date’ LiDAR meshes, DEM’s were obtained from NOAA’s Continuously Updated Digital Elevation Model (CUDEM; CIRES, 2014) and USGS’s Coastal National Elevation Database (CoNED; Danielson & Haines, 2023) at all available time steps for Dauphin and Petit Bois Islands and their nearshore bathymetry. The elevations of Petit Bois, West Petit Bois, and Dauphin Islands were interpolated onto the Post-Ivan (2004) DEM using the same method employed for the DEM output by XBeach/EDGR. The vertical features (Bilskie et al., 2015) were flagged on Dauphin Island to retain peak dune heights. Mainland elevations were not updated. Table 3.2 shows which DEM was used for each storm's most up-to-date observed data.

Storm	Landfall Date	Up-to-date LiDAR DEM	DEM Source
Arlene	June 11, 2005	Post-Ivan (2004)	USACE, USGS, NASA
Cindy	July 6, 2005	Post-Ivan (2004)	USACE, USGS, NASA
Dennis	July 7, 2005	Post-Ivan (2004)	USACE, USGS, NASA
Katrina	Aug. 29, 2005	Post-Ivan (2004)	USACE, USGS, NASA
Ida	Nov. 10, 2009	2008 July	USGS CoNED
Nate	Oct. 7, 2017	2016 July-October	USACE
Alberto	May 28, 2018	2016 July-October	USACE
Gordon	Sept. 3, 2018	2016 July-October	USACE
Cristobal	June 7, 2020	2018 Oct-Nov (DI) & 2019 Nov (PB)	USGS, USACE
Sally	Sept. 16, 2020	2018 Oct-Nov (DI) & 2019 Nov (PB)	USGS, USACE

Table 3.2: Chronological list of storms, their year, the time that the most up to date available LiDAR and/or survey data for that DEM was collected, and which organization collected this data.

Model Error Quantification

Hydrodynamic Model Validation

Water level time-series data was available in six-minute intervals from NOAA's tide gauge system (*CO-OPS Map*, 2023). Fourteen stations (4-8 per storm) were located within 100 km of the Dauphin Island NOAA Station (#8735180; Figure 3.1) and had WSE data for all or part of the storm duration. Four total (1-3 per storm) NOAA NDBC stations (*National Data Buoy Center*, 2023) were located within a 120 km radius of NOAA Station #8735180 and had wave direction, period, and/or height data available for all or part of the storm duration.

ADCIRC+SWAN computed WSE time-series, significant wave height, mean wave period, peak wave period, and wave direction at a 1-second time step. These time-series, as well as maximum WSE, were compared to observed values at corresponding geographic coordinates. WSE time-series values were compared to NOAA tide gauge observations using RMSE, MN

Bias, and SI (Equations 3.1, 3.2, and 3.3) for each storm, “where N is the number of observations, $E_i = S_i - O_i$ is the error between the modeled S_i and measured O_i values, and $\bar{E}$ is the mean error” (Dietrich, Westerink, et al., 2011; Hanson et al., 2009). RMSE is measured in meters, and MN Bias and SI are unitless (*Model Performance Statistics Definitions*, 2017). Average values for these metrics were calculated for each storm at all available NOAA tide gauges and NDBC buoys.

Root Mean Squared Error
$$\sqrt{\frac{\sum_{i=1}^{N}(S_i - O_i)^2}{N}} \tag{3.1}$$

Normalized Bias
$$\frac{\frac{1}{N}\sum_{i=1}^{N} E_i}{\frac{1}{N}\sum_{i=1}^{N}|O_i|} \tag{3.2}$$

Scatter Index
$$\frac{\sqrt{\frac{1}{N}\sum_{i=1}^{N}(E_i - \bar{E})^2}}{\frac{1}{N}\sum_{i=1}^{N}|O_i|} \tag{3.3}$$

To verify that using ERA5+GAHM winds improved hydrodynamic model accuracy compared to simulations that used ERA5 only, time-series and peak wind speed and WSE were compared. Observed and simulated wind speed and WSE were compared for simulations run with ERA5 only, and for ERA5+GAHM, on the Post-Ivan DEM. Observed values were pulled from all NOAA stations within 500 km of the NOAA station at eastern Dauphin Island (NOAA #8735180; Figure 3.1) (Table 3.3). For WSE, only stations with data available with respect to NAVD88 or MSL datums were selected. RMSE, MN Bias, and SI were used to quantify error between wind speed and WSE time-series plots throughout the model period. Peak wind speeds and WSE were also regressed against one another, and slope of the regression line and R^2 were quantified.

Station #	**State**	**Years active (WSE)**	**Years active (Wind)**
NOAA 8727520	FL	2005	2005, 2018
NOAA 8728690	FL	2005	N/A
NOAA 8729210	FL	2005	2005, 2017, 2018
NOAA 8729840	FL	N/A	2005, 2009, 2018, 2020
NOAA 8731439	AL	2009	N/A
NOAA 8734673	AL	N/A	2009, 2017, 2018, 2020
NOAA 8735180	AL	2005, 2009, 2017, 2018, 2020	2005, 2009, 2017, 2018, 2020
NOAA 8735181	AL	2005	N/A
NOAA 8735391	AL	2017, 2018, 2020	N/A
NOAA 8735523	AL	2017, 2018, 2020	2018
NOAA 8736897	AL	2009, 2017, 2018, 2020	2009, 2017, 2018, 2020
NOAA 8737048	AL	2009, 2017, 2018, 2020	2018
NOAA 8737138	AL	2017, 2018, 2020	2018
NOAA 8738043	AL	2017, 2018, 2020	2018
NOAA 8739803	AL	2017	2018
NOAA 8741003	MS	N/A	2009, 2018, 2020
NOAA 8741094	MS	N/A	2009, 2017
NOAA 8741196	MS	2005	N/A
NOAA 8741501	MS	N/A	2009, 2017
NOAA 8741533	MS	2009, 2017, 2018, 2020	2018
NOAA 8742221	MS	2005	N/A
NOAA 8743281	MS	2005	2005
NOAA 8744117	MS	2005	N/A
NOAA 8744707	MS	N/A	2009
NOAA 8745557	MS	2009	N/A
NOAA 8745651	MS	N/A	2009
NOAA 8747437	MS	2009, 2017, 2018, 2020	2009, 2017, 2018, 2020
NOAA 8747766	MS	2005	2005
NOAA 8760721	LA	N/A	2017, 2018, 2020
NOAA 8760922	LA	2005, 2009, 2017, 2018, 2020	2005, 2009, 2017, 2018, 2020
NOAA 8761305	LA	2009, 2017, 2018, 2020	2009, 2017, 2018, 2020
NOAA 8761724	LA	2005, 2009, 2017, 2018, 2020	2005, 2009, 2017, 2018, 2020
NOAA 8761927	LA	2009, 2017, 2018, 2020	2009, 2018, 2020
NOAA 8761955	LA	2009, 2017, 2018, 2020	2018
NOAA 8762372	LA	N/A	2005, 2009
NOAA 8762484	LA	N/A	2018
NOAA 8764227	LA	2009, 2017, 2018, 2020	2009, 2017, 2018, 2020
NOAA 8764314	LA	N/A	2017, 2018, 2020
NOAA 8766072	LA	2009, 2017, 2018, 2020	2017, 2018
NOAA 8767961	LA	N/A	2018
NOAA 8768094	LA	2005, 2009, 2017, 2018, 2020	2005, 2009, 2018
NOAA 8769858	LA	2020	N/A

Table 3.3: NOAA Stations used for WSE and wind speed time-series and peak value comparisons between ERA5 and ERA5+GAHM. Years active includes years within the study period (2005-2020) during which at least one of the selected storms occurred.

Island Transects

Simplified -5-meter contour lines (“simplified shorelines”) (Figure 3.6a) were drawn around West Petit Bois, Petit Bois, and Dauphin Islands. The eastern end of Dauphin Island was excluded because this area experiences minimal morphological changes due to urbanization, and was not the focus of this study. Cross-shore transects were created (Figure 3.6b), and extend perpendicularly from the simplified southern shoreline until they intersect with the simplified northern shoreline. The transects were spaced every 1 kilometer in the alongshore direction, expect for at Katrina Cut where they were spaced every 0.5 km. Elevations were extracted at 1-meter intervals along each transect.

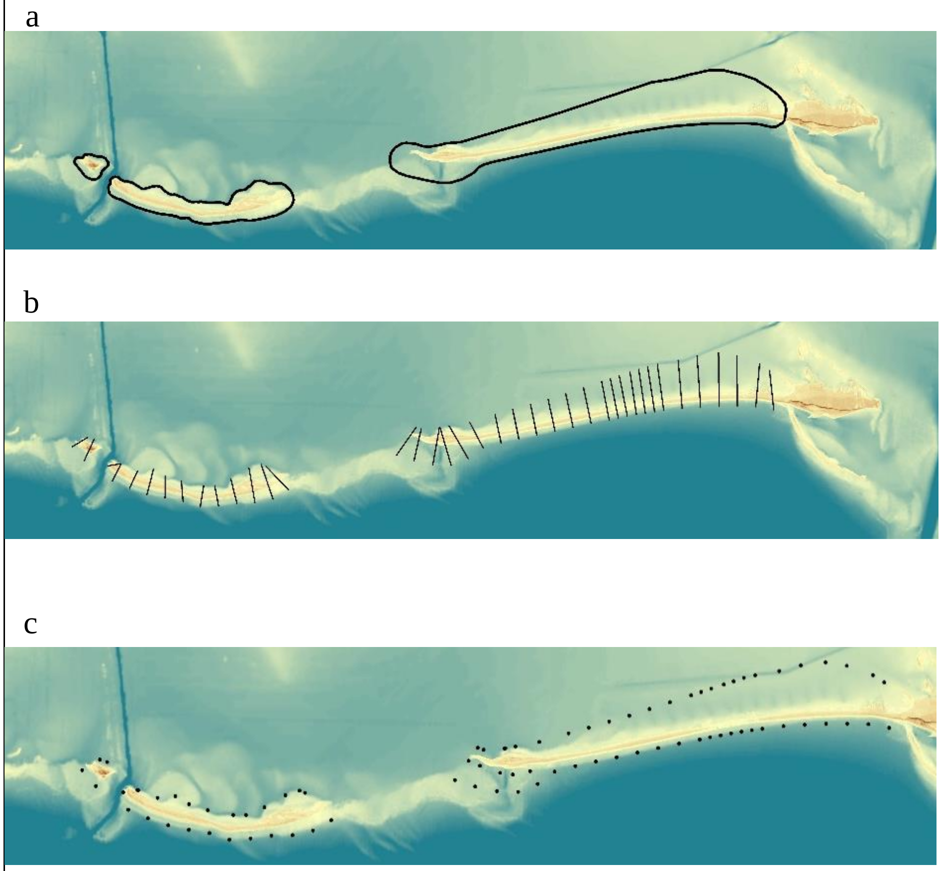

a. Simplified shoreline, roughly located at the -5-meter contour line.

b. Cross-shore transects that begin at the seaward side of the simplified shoreline and extend to the northern side of the simplified shoreline.

c. Nearshore points located at the northernmost and southernmost point of each transect, as well as along the transect closer to the shoreline on western Dauphin Island.

Figure 3.6 – Island transects & nearshore points.

Morphology Error Quantification

The original Post-Ivan, XBeach updated, and up-to-date LiDAR DEM's were compared, with the up-to-date LiDAR DEM's being considered the 'true' value. Beach profiles across island transects (Figure 3.6b) were compared between the three DEM's using RMSE, MN Bias, and SI. The peak elevation height and location, the 0-meter intercept, and the area beneath the transect between the 0-meter bounds were calculated for each transect and then compared between the different DEM's. The location of the 0-meter elevation contour line was compared for each DEM. The area and volume of the island above 0 meters NAVD88 were also calculated.

Nearshore Hydrodynamics

Simulated WSE, significant wave height, wave direction, and mean and peak wave period were extracted from 39 nearshore points (Figure 3.6c) located at the intersection of each transect and the seaward side of the simplified shoreline. Five additional nearshore points, located along the transects, but closer to shore, were also selected on western Dauphin Island. WSE and wave variables were compared between DEMs at these locations using RMSE, MN Bias, and SI. WSE and significant wave height were extracted from 39 points on the back side of the island, where the transects intersect with the northern side of the simplified shoreline. WSE and significant wave height time series and maxima were studied at 40 points at the 0 m contour near the shore of the mainland (Figure 3.8).

High Water Marks

High water mark (HWM) observations for several storms were obtained from LSU's SurgeDAT Data Center (*Surge Database Console*, 2018) and the USGS flood event viewer (*Flood Event Viewer*, 2023). Simulated WSE maxima were regressed against observed HWM data, and the R^2 and the slope of the regression line were quantified. This was repeated for each individual storm, and for all storms at once, for points within 200 km of NOAA Station #8735180 at Dauphin Island (Figure 3.1).

In addition to comparisons to observed data, 40 points on the shoreline of the mainland (Figure 3.8), plus 65 points located along the cross-shore transects (Figure 3.7), were selected for studying the direct localized impacts of topobathy on the simulated HWM. WSE maxima for the same storm on different DEMs were regressed against one another. This was repeated for only mainland points, only points along the cross-shore transects, and for all 105 points. R^2 and the slope of the regression line were quantified.

Figure 3.7: Selected locations on the barrier islands for WSE and significant wave height analysis

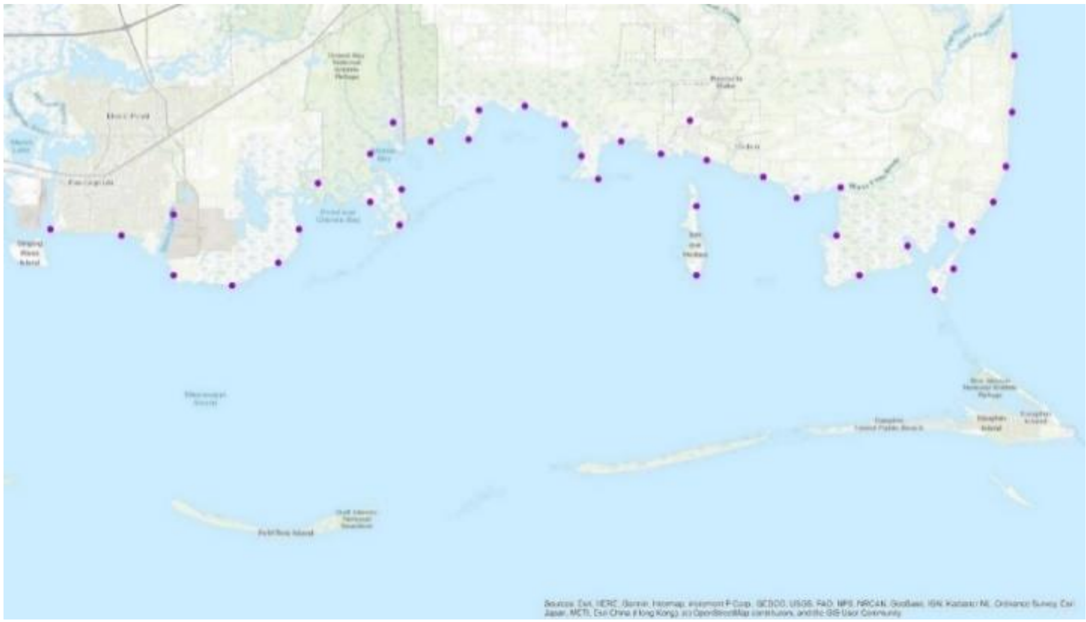

Figure 3.8: Selected points on the mainland for WSE and significant wave height analysis

CHAPTER 4

RESULTS

Hydrodynamic Model Validation

ADCIRC+SWAN hydrodynamic simulations were validated using WSE data from all available NOAA tide gauges within 100 km of Dauphin Island, and wave data from all NDBC stations within 120 km of Dauphin Island, for each storm using RMSE, MN Bias, and SI. NOAA Station 8739803 was excluded from analysis due to consistent overestimation of WSE by greater than 1 m, likely caused by poor mesh resolution at the NOAA station's inland location. NOAA Station 8741196 was also excluded because it was only active for Tropical Storm Arlene. Post-Ivan LiDAR data was the most up-to-date observation for the storms that occurred in 2005. Therefore, only storms post-2005 were simulated using all three DEMs. Hindcasts were completed for all storms on the Post-Ivan DEM, all storms except Arlene on the XBeach-generated DEM, and all storms after 2005 on the LiDAR-derived DEM (Table 4.1).

Storm	# NOAA Stations	# NDBC Stations	Post-Ivan DEM	XBeach DEM	LiDAR DEM
Arlene	5	2	✓		
Cindy	5	1*	✓	✓	
Dennis	5	1*	✓	✓	
Katrina	4	2	✓	✓	
Ida	6	2	✓	✓	✓
Nate	8	2	✓	✓	✓
Alberto	8	2	✓	✓	✓
Gordon	8	2	✓	✓	✓
Cristobal	8	2	✓	✓	✓
Sally	8	2	✓	✓	✓

*No wave direction data available

Table 4.1: Stations used for validation of simulation results, and DEMs used for simulations.

Model Error

Simulated WSE and significant wave height were significantly different from observed values (p = 0.00) according to two-way paired t-tests. WSE error for the three different DEMs, on average across all storms, were not statistically significant from one another ($p \leq 0.10$). Average error across all storms ranged from 0.192 - 0.204 m for RMSE, -0.234 - -0.247 for MN Bias, and 0.319 - 0.347 for SI (Table 4.2). This level of error is consistent with other studies (e.g., Dietrich, Westerink, et al., 2011; Kerr et al., 2013) and constitutes accurate representation of the physical system. Stations that lack data beyond 2005 are listed as "No data" in the LiDAR column. Wave variables were not averaged across all storms due to the limited number of stations with available observational data.

	Post-Ivan WSE Averages			XBeach WSE Averages			LiDAR WSE Averages		
Station	RMSE	MN Bias	SI	RMSE	MN Bias	SI	RMSE	MN Bias	SI
NOAA 8731439	0.149	-0.331	0.288	0.145	-0.357	0.233	0.145	-0.358	0.226
NOAA 8735180	0.150	-0.058	0.305	0.148	-0.079	0.276	0.139	-0.178	0.217
NOAA 8735181	0.142	-0.067	0.298	0.149	-0.062	0.309	No data	No data	No data
NOAA 8735391	0.255	-0.383	0.314	0.255	-0.384	0.310	0.255	-0.384	0.311
NOAA 8735523	0.158	-0.171	0.299	0.156	-0.172	0.292	0.157	-0.173	0.294
NOAA 8736897	0.237	-0.278	0.376	0.231	-0.286	0.355	0.231	-0.287	0.357
NOAA 8737048	0.227	-0.309	0.361	0.222	-0.316	0.340	0.224	-0.318	0.344
NOAA 8737138	0.238	-0.155	0.388	0.236	-0.164	0.383	0.238	-0.157	0.386
NOAA 8738043	0.170	-0.160	0.339	0.167	-0.165	0.326	0.168	-0.167	0.329
NOAA 8741533	0.209	-0.262	0.345	0.200	-0.261	0.318	0.205	-0.270	0.326
NOAA 8742221	0.314	-0.394	0.402	0.385	-0.428	0.476	No data	No data	No data
NOAA 8743281	0.191	-0.280	0.299	0.202	-0.277	0.311	No data	No data	No data
NOAA 8744117	0.195	-0.274	0.349	0.204	-0.266	0.374	No data	No data	No data
NOAA 8745557	0.189	-0.150	0.496	0.159	-0.175	0.397	0.159	-0.176	0.399
Average	0.202	-0.234	0.347	0.204	-0.242	0.336	0.192	-0.247	0.319
Maximum	0.314	-0.058	0.496	0.385	-0.062	0.476	0.255	-0.157	0.399
Minimum	0.142	-0.394	0.288	0.145	-0.428	0.233	0.139	-0.384	0.217

Table 4.2: Average WSE error for all storms at each station. RMSE is in meters.

The NHC best track durations overlapped for Hurricanes Cindy and Dennis (2005). Therefore, statistics for Hurricane Cindy were calculated for July 3, 2005 at 1800 UTC to July 8, 2005 at 0600 UTC, and statistics for Hurricane Dennis began July 8, 2005 at 0600 UTC. During Hurricane Katrina, two of the four NOAA stations stopped collecting data prior to the end of the NHC best track duration, near the peak of the storm on August 29, 2005 at 0600 UTC. NDBC station 42007 also stopped collecting data prior to the end of the storm, on August 29, 2005 at 0700 UTC.

Average RMSE and SI were both lowest for LiDAR DEMs (0.192 m and 0.319) compared to Post-Ivan (0.202 m and 0.347) and XBeach (0.204 m and 0.336) DEMs. Average MN Bias was lowest for the Post-Ivan DEM (-0.234) compared to XBeach (-0.242) and LiDAR (-0.247). It is important to note that variation of these values between DEMs was minimal; RMSE varied by less than one centimeter between DEMs when all stations were averaged.

Wave variables displayed less obvious trends. Simulated significant wave height and peak period most closely matched observed values when the Post-Ivan DEM was used; mean wave period showed the best agreement for simulations run on XBeach DEMs; wave direction best matched observations on the LiDAR DEMs. Again, the range of error was small; on average, the RMSE ranges for significant wave height, peak period, mean period, and wave direction were 0.03 m, 0.80 s, 0.09 s, and 6.68 degrees, respectively. The small sample size (4 stations) limits the weight that these statistics hold, though the results suggest good agreement between modelled and observed data.

ERA5 versus ERA5+GAHM

Model time-series error was quantified for WSE and wind speeds (Table 4.3). For wind speed, average RMSE and SI were lower for ERA5 than ERA5+GAHM. Meanwhile, MN Bias and the absolute value of MN Bias was slightly lower for ERA5+GAHM. For WSE, average RMSE, absolute MN Bias, and SI were lower for ERA5 than ERA5+GAHM, while MN Bias was improved with ERA5+GAHM compared to ERA5. For both wind speed and WSE, differences in average error were slight.

		RMSE	MN Bias	SI	Absolute MN Bias
WSE	ERA5 only	0.23 m	-0.06	0.35	0.34
	ERA5+GAHM	0.24 m	-0.03	0.37	0.34
Wind Speed	ERA5 only	2.96 m/s	0.30	0.60	0.33
	ERA5+GAHM	3.33 m/s	0.28	0.70	0.32

Table 4.3: Error metrics, averaged for all storms at all stations, for WSE and wind speeds.

Peak observed and simulated wind speed and WSE values for all storms at all stations were regressed against one another. The slope of the regression line for observed versus simulated wind speeds was 0.564 for simulations that used ERA5 and 0.414 for simulations that used ERA5+GAHM (Figure 4.1). However, the R^2 was lower for ERA5 peak wind speed comparisons than for ERA5+GAHM simulations (0.299 vs. 0.360, respectively; Figure 4.1). Simulations run with ERA5+GAHM had a more even split of over- and underestimated wind speeds, skewed toward overestimation (58% vs. 42%, Figure 4.1). Simulations which used only ERA5 had substantially fewer overestimations than underestimations (30% vs. 70%, Figure 4.1).

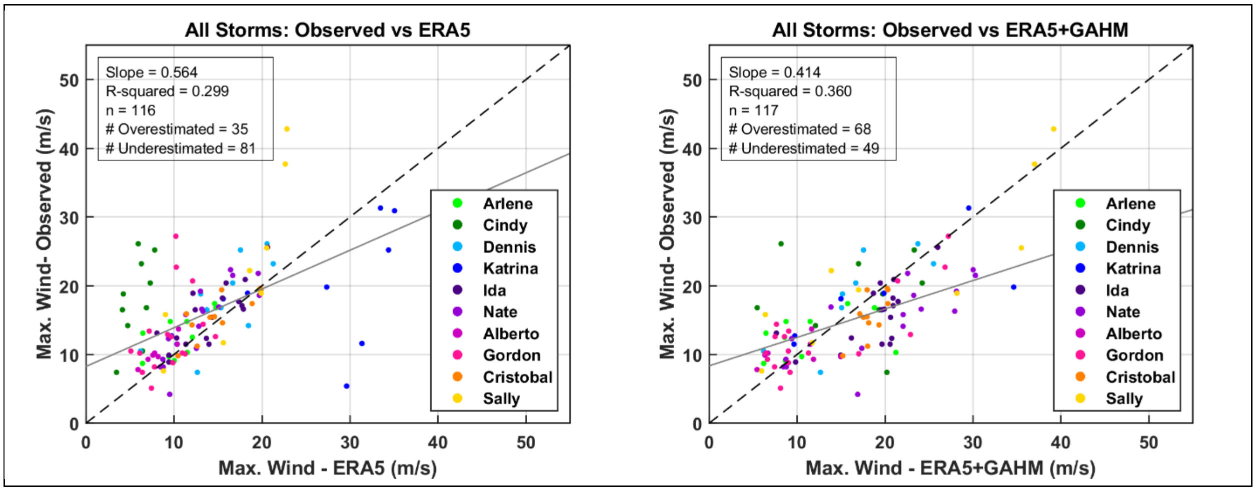

Figure 4.1: Observed and simulated peak wind speeds for simulations run using ERA5 only (left) and ERA5+GAHM (right).

For regressions of observed and simulated peak WSE, instances where observed and simulated values differed by ≥ 5 m were removed, as they indicated faulty observations. The slopes of the regression lines were effectively equal for simulations run using ERA5 only compared to those using ERA5+GAHM (0.546 vs. 0.545, Figure 4.2). The R^2 was lower for simulations run with ERA5 only than for simulations which used ERA5+GAHM (0.483 vs. 0.500, Figure 4.2). Similar to wind speed comparisons, ERA5+GAHM simulations had a more even split between over-and under-estimations (55% vs. 45%), skewed toward overestimations. Simulations which used ERA5 only had substantially more over- than underestimations, 33% vs. 67%.

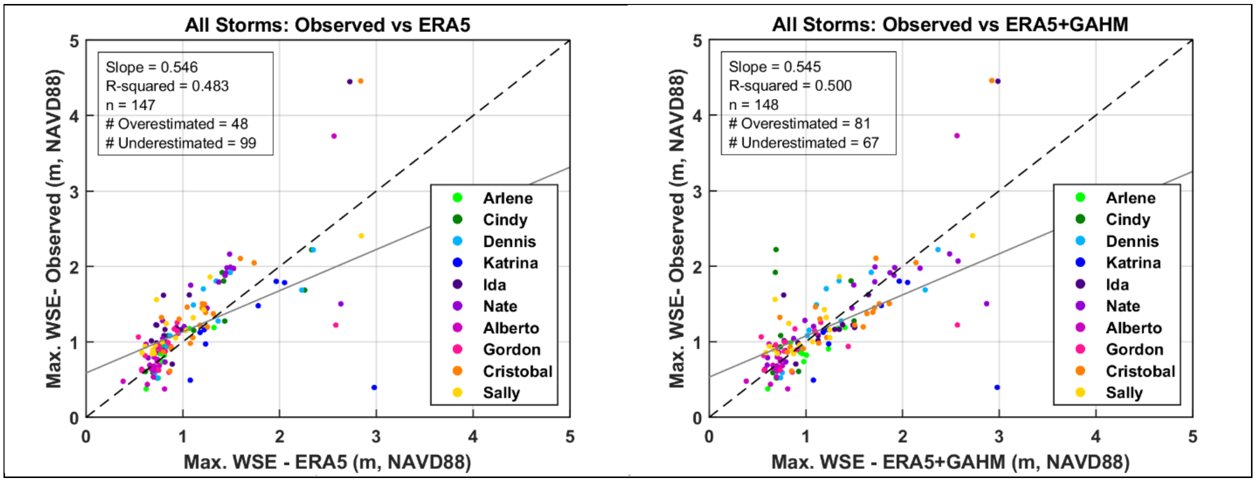

Figure 4.2: Observed and simulated peak WSE for simulations run using ERA5 only (left) and ERA5+GAHM (right).

Nearshore Hydrodynamics

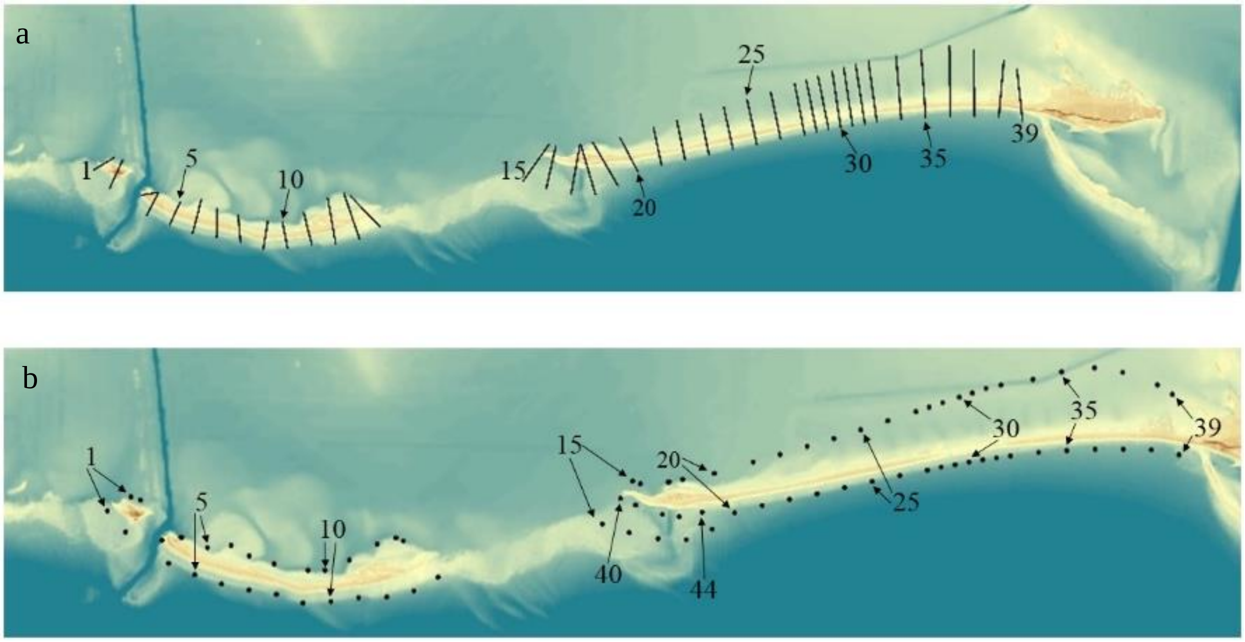

Figure 4.3: Numbered transects (top) and points on the front and back of the islands (bottom).

Water Surface Elevation

WSE was compared between Post-Ivan, XBeach, and LiDAR DEMs on both the seaward (front) side of the islands, and on the back side of the islands for all storms (Figure 4.3b, Table 4.4). Simulated values were not statistically significantly different between DEMs ($p \leq 0.10$) for any storms on either the front or back sides. XBeach and LiDAR DEMs were most similar to one another, with the lowest RMSE (0.007 m) and SI (0.020).

	RMSE (m)	MN Bias	SI
PI v XB	0.018	**0.002**	0.050
back	0.035	*0.005*	0.095
PI v LiDAR	0.020	-0.004	0.058
back	0.029	-0.016	0.081
XB v LiDAR	**0.007**	-0.005	**0.020**
back	*0.023*	-0.016	*0.066*

Table 4.4: Statistics, averaged across all points, comparing WSE for all three DEMs. Minimum error values for the front side of the island are bolded, and those for the back side of the island are italicized.

Differences between DEMs were larger on the back side of the island than the front. For the front side of the islands, differences between DEMs were greatest at points 1, 14, 15, 16, 18, and 23. For the back side of the islands, differences between DEM increased from east to west, with RMSE, MN Bias, and SI all peaking at the transects east of Katrina Cut, Dauphin Island. Hydrodynamic error between simulations run on Post-Ivan and XBeach DEMs and Post-Ivan and LiDAR DEMs did not increase over time.

Averaged for all storms on all DEMs, simulated WSE was 6.8 cm higher behind the island than in front of the island. Post-Ivan DEMs predicted an average 8.2 cm difference, XBeach predicted 7.1 cm, and LiDAR 5.3 cm. Two-tailed paired t-tests ($p \leq 0.05$) showed that simulated water level gradients for all DEMs were significantly different from one another ($p = 0$).

WSE time series and peak WSE were compared between DEMs at 40 points located at the mainland shoreline (Figure 3.7). WSE time series on the mainland were compared using RMSE, MN Bias, and SI. All comparisons showed low RMSE, MN Bias, and SI (Table 4.5), and based on averages of these measures across all storms at all points, there were no two DEMs that were clearly most similar to each other. On average, peak WSE was most similar between the XBeach and LiDAR DEMs, with an average difference of 0.9 cm. The Post-Ivan and XBeach had an average difference of 3.3 cm, and the Post-Ivan and LiDAR DEMs had an average difference of 2.4 cm. The maximum and minimum average differences between DEMs followed the same trend where Post-Ivan vs. XBeach > Post-Ivan vs. LiDAR > XBeach vs. LiDAR. Despite the small differences between peak WSE, two-way paired t-tests showed significant differences ($p \leq 0.05$) between average peaks for all DEMs. Only for Hurricanes Katrina (2005) and Alberto (2018) did one or more comparison showed no statistically significant difference in peak WSE.

	RMSE (m)	MN Bias	SI
PI v XBeach	0.025	**0.002**	0.061
PI v LiDAR	0.017	-0.010	**0.044**
XBeach v LiDAR	**0.016**	-0.008	0.045

Table 4.5 -Statistics, averaged across all points, comparing WSE on the mainland for all three DEMs. Minimum error values are bolded.

Significant Wave Height

Significant wave height was compared between Post-Ivan, XBeach, and LiDAR DEMs on both the seaward side of the islands, and the back side of the islands for all storms (Table 4.6). Simulated values were statistically significantly different between DEMs ($p \leq 0.05$) for some storms at some points (Table A.1, A.2).

	RMSE (m)	MN Bias	SI
PI v XB	0.074	-0.016	0.066
back	0.040	-0.024	0.062
PI v LiDAR	**0.037**	**0.003**	**0.036**
back	*0.036*	-0.027	*0.061*
XB v LiDAR	0.084	0.023	0.080
back	0.037	*0.003*	0.072

Table 4.6: Statistics, averaged across all points, comparing significant wave heights for all three DEMs. Minimum error values for the front side of the island are bolded, and those for the back side of the island are italicized.

For the front side of the islands, differences between DEMs were greatest at transects 1, 14, 15, 16, 23, and 44. For the back side of the islands, differences between all DEMs were elevated at transects across Katrina Cut. Differences between DEMs were also high on West Petit Bois Island and Western Dauphin Island. Errors between Post-Ivan and XBeach and Post-Ivan and LiDAR did not display any noticeable pattern of change over time.

On average, simulated significant wave height was 1.53 m higher in front of the island than behind the island. Post-Ivan DEMs predicted an average of 1.54 m different, XBeach predicted 1.46 m, and LiDAR 1.58 m. Two-tailed paired t-tests ($p \leq 0.05$) showed that simulated wave attenuation values for both Post-Ivan and LiDAR DEMs were significantly different from the XBeach DEM ($p = 0.00$ for both). Wave attenuation for simulations run on Post-Ivan and LiDAR DEMs were not significantly different from one another ($p = 0.086$).

Significant wave height time series and peak significant wave heights were compared for each DEM at 40 points located at the mainland shoreline (Figure 3.7). Significant wave height time series on the mainland were compared using RMSE, MN Bias, and SI. All comparisons showed low RMSE (≤1 cm), MN Bias, and SI; based on these measures the Post-Ivan and XBeach DEMs performed most differently by a slight margin. On average, peak wave heights were most similar between the XBeach and LiDAR DEMs, with an average difference of 0.5 cm. The Post-Ivan and XBeach has an average difference of 1.4 cm, and the Post-Ivan and LiDAR DEMs had an average difference of 0.9 cm. In contrast to the small differences between peak WSE, two-way paired t-tests showed significant differences ($p \leq 0.05$) between average peaks for all DEMs. Only for Hurricanes Dennis (2005), Katrina (2005), and Sally (2020) did one or more comparison showed no statistically significant difference in peak significant wave height.

LiDAR – Post-Ivan Peak Wave Height

LiDAR – XBeach Peak Wave Height

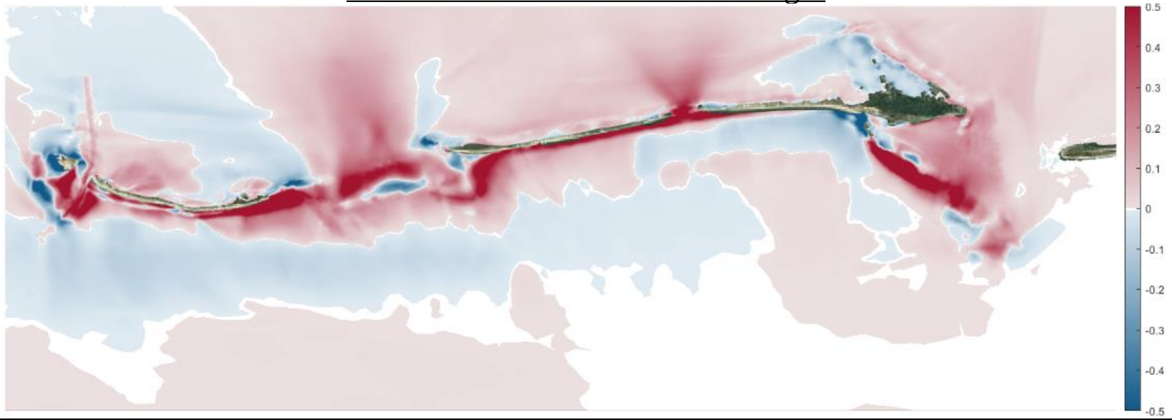

Post-Ivan – XBeach Peak Wave Height

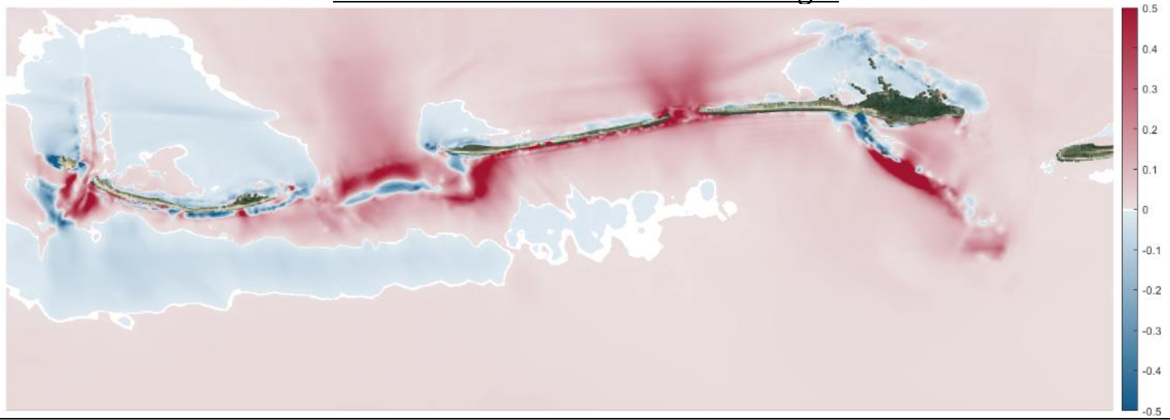

Figure 4.4: Differences between peak wave heights for the three DEMs; red indicates that the wave heights for the first DEM listed were greater than for the second, and vice-versa for blue.

Mean & Peak Period

Mean and peak period were compared between Post-Ivan, XBeach, and LiDAR DEMs on the seaward side of the islands for all storms. For both mean and peak period, Post-Ivan and LiDAR DEMs were the most similar when RMSE and SI were considered. Post-Ivan and

XBeach DEMs had the lowest absolute difference in MN Bias for both measures. XBeach and LiDAR DEMs were least similar for both mean and peak period. Simulated values were statistically significantly different between DEMs ($p \leq 0.05$) for some storms at some points (Table A.3).

	RMSE (s)	MN Bias	SI
PI v XB (Mean)	0.155	**0.003**	0.021
PI v LiDAR (Mean)	**0.115**	-0.003	**0.016**
XB v LiDAR (Mean)	0.178	-0.006	0.025
PI v XB (Peak)	0.233	**0.000**	0.031
PI v LiDAR (Peak)	**0.198**	-0.003	**0.029**
XB v LiDAR (Peak)	0.242	-0.003	0.035

Table 4.7: Statistics, averaged across all points, comparing mean and peak period for all three DEMs. Minimum error values are bolded.

Wave Direction

Wave direction was compared between Post-Ivan, XBeach, and LiDAR DEMs on the seaward side of the islands for all storms. Simulated wave direction was most similar for simulations run on the Post-Ivan and LiDAR DEMs for all error metrics. Simulated values were statistically significantly different between DEMs ($p \leq 0.05$) for some storms at some points (Table A.4).

	RMSE (degrees)	MN Bias	SI
PI v XB	6.218	0.011	0.052
PI v LiDAR	**5.114**	**0.001**	**0.043**
XB v LiDAR	7.579	-0.005	0.056

Table 4.8: Statistics, averaged across all points, comparing wave direction for all three DEMs. Minimum error values are bolded.

High Water Marks

Observed and simulated HWM were regressed for all storms with available data for each DEM. The only storms with observed data that were simulated using all three DEMs were Hurricanes Nate (2017) and Gordon (2018) (Figure 4.5). Simulations run on the XBeach-updated

DEM slightly outperforms the others, though differences between the slope of the regression line and the R^2 were minimal.

Five storms were run on both the XBeach and Post-Ivan DEMs and had HWM data available. When all storms were regressed together, the R^2 and slope were identical. One more point was wetted for the XBeach DEM than the Post-Ivan DEM. No regressions showed a substantial difference between XBeach and Post-Ivan DEMs when compared to observed data.

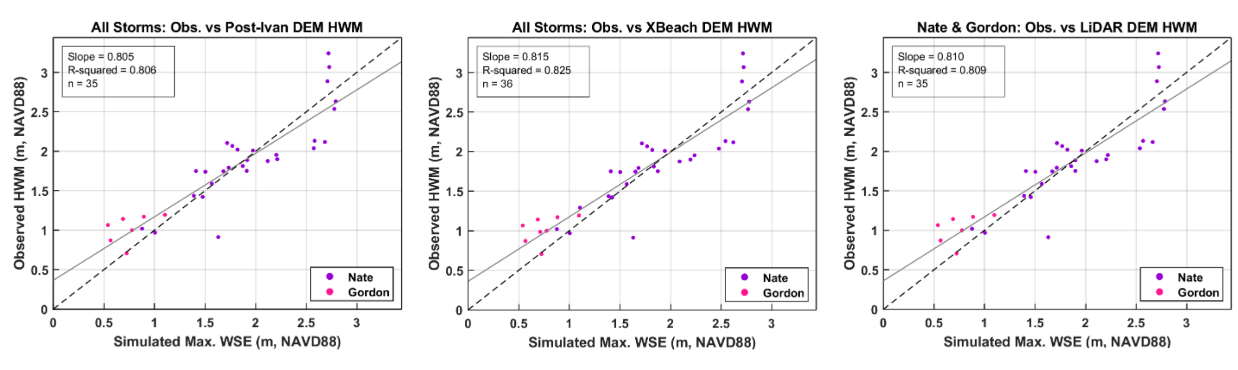

Figure 4.5: Observed vs. simulated HWM within 200 km of the Dauphin Island NOAA station for the Post-Ivan, XBeach, and LiDAR DEMs.

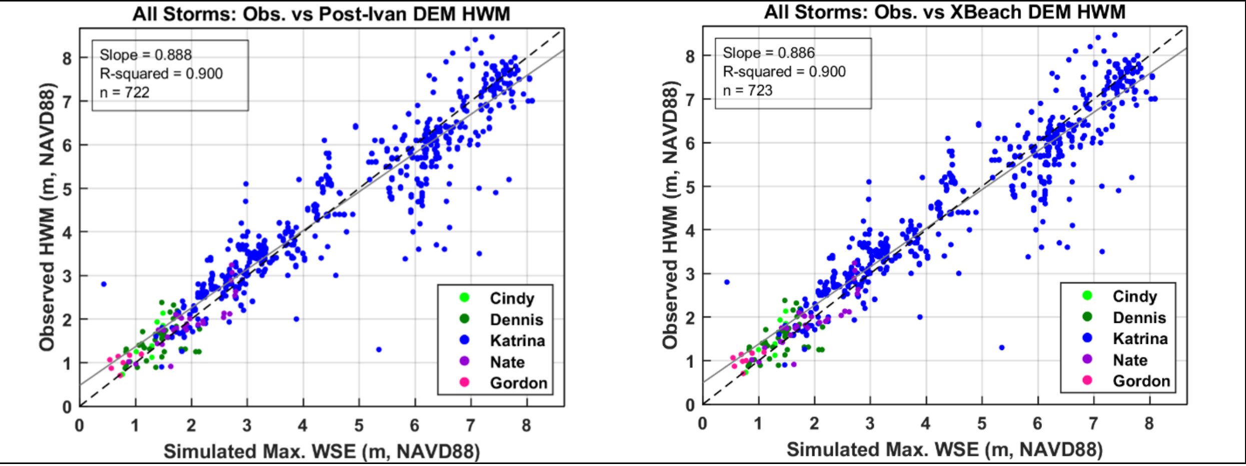

Figure 4.6: Observed vs. simulated HWM within 200 km of the Dauphin Island NOAA stations for the Post-Ivan and XBeach DEMs.

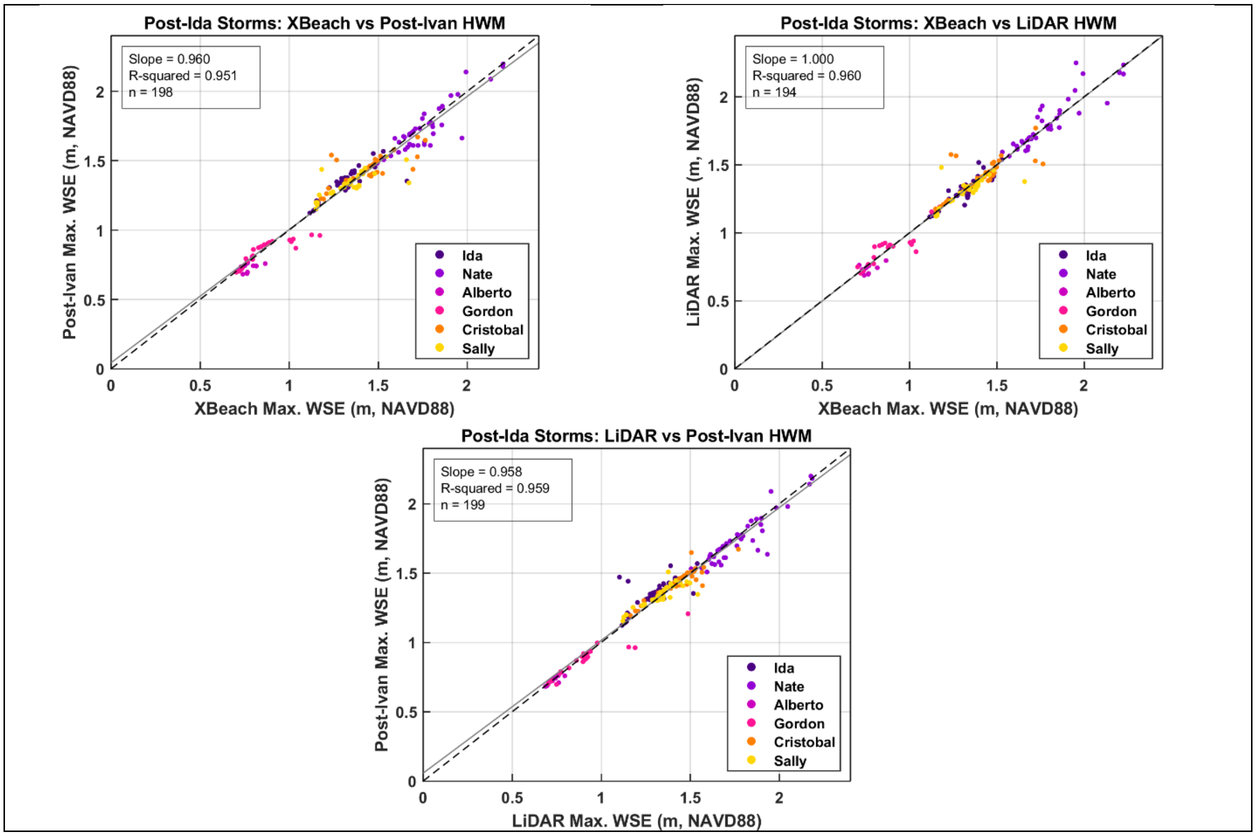

Figure 4.7: Peak WSE comparisons for the 65 points on the barrier islands.

Storm	Post-Ivan DEM			XBeach DEM			LiDAR DEM		
	Slope	R^2	n	Slope	R^2	n	Slope	R^2	n
Cindy	1.65	0.76	7	1.65	0.76	7	N/A	N/A	N/A
Dennis	0.48	0.19	35	0.48	0.19	35	N/A	N/A	N/A
Katrina	0.86	0.87	645	0.86	0.87	645	N/A	N/A	N/A
Nate	0.86	0.72	28	0.87	0.75	28	0.87	0.73	28
Gordon	0.44	0.23	7	0.45	0.23	8	0.44	0.23	7
Nate + Gordon	0.805	0.806	35	0.815	0.825	36	0.810	0.809	35
All	0.888	0.900	722	0.886	0.900	723	N/A	N/A	N/A

Table 4.9: Observed versus simulated correlation statistics for each DEM.

Maximum water levels at 65 points on the barrier islands (Figure 3.8) and 40 points on the mainland shoreline (Figure 3.7) were selected for comparison between DEMs. Simulated maximum WSE was compared at both the mainland and island points together for all storms post-2005. For all storms at all points, LiDAR and Post-Ivan performed most similarly (Table 4.10). However, LiDAR and XBeach perform most similarly when storms were considered individually (Table 4.10). When only points on the mainland were included, all storms perform highly similarly (R^2 = 0.998-0.999, slope = 1.010-1.033; Figure 4.7 & Table 4.10). When only points on the three islands were included, LiDAR and XBeach perform the most similarly (R^2 = 0.960, slope = 1.000), though all correlations were high (Table 4.10). Hurricanes Cindy, Dennis, and Katrina (2005) were only simulated using Post-Ivan and XBeach DEMs; R^2 and slope of the regression line for these storms are presented in Table 4.11.

	Storm	Post-Ivan vs. XBeach		Post-Ivan vs. LiDAR		LiDAR vs. XBeach	
		Slope	R^2	Slope	R^2	Slope	R^2
Mainland Only	Ida	1.131	0.972	1.073	0.981	**1.057**	**0.997**
	Nate	1.045	0.994	1.023	0.998	**1.022**	**0.998**
	Alberto	**0.952**	**0.954**	0.791	0.636	0.867	0.778
	Gordon	1.102	0.993	1.088	**0.998**	**1.013**	0.995
	Cristobal	0.961	0.998	**0.984**	**0.999**	0.976	0.999
	Sally	0.918	0.997	0.932	0.998	**0.986**	**0.999**
	All	1.033	0.998	**1.010**	**0.999**	1.023	0.999
Island Only	Storm	Post-Ivan vs. XBeach		Post-Ivan vs. LiDAR		LiDAR vs. XBeach	
		Slope	R^2	Slope	R^2	Slope	R^2
	Ida	0.756	0.676	0.736	0.523	**0.961**	**0.842**
	Nate	**0.980**	0.798	0.973	**0.842**	0.957	0.824
	Alberto	0.396	0.219	**0.864**	**0.726**	0.418	0.278
	Gordon	0.565	0.744	0.599	**0.857**	**0.815**	0.771
	Cristobal	0.541	0.596	**0.775**	**0.841**	0.652	0.580
	Sally	0.497	0.552	**0.675**	**0.738**	0.646	0.572
	All	0.960	0.951	0.958	0.959	**1.000**	**0.960**
Mainland and Island	Storm	Post-Ivan vs. XBeach		Post-Ivan vs. LiDAR		LiDAR vs. XBeach	
		Slope	R^2	Slope	R^2	Slope	R^2
	Ida	0.916	0.801	0.906	0.742	**1.007**	**0.916**
	Nate	1.086	0.976	1.048	**0.985**	**1.026**	0.979
	Alberto	0.623	0.665	**0.919**	**0.858**	0.627	0.702
	Gordon	1.093	0.942	1.033	0.933	**1.010**	**0.965**
	Cristobal	0.822	0.822	**0.956**	**0.939**	0.845	0.831
	Sally	0.773	0.878	0.860	**0.945**	**0.886**	0.894
	All	**1.000**	0.996	0.997	**0.998**	1.017	0.988

Table 4.10: Slope and R^2 for points only on the mainland (top), only on the three islands (middle), and on all points (bottom) when compared between DEMs. Values closest to 1.000 are bolded.

	Storm	Post-Ivan vs. XBeach	
		Slope	R^2
Mainland Only	Cindy	**0.999**	**0.999**
	Dennis	0.975	**0.998**
	Katrina	**0.984**	**0.999**
Island Only	Cindy	0.827	0.728
	Dennis	0.874	0.809
	Katrina	0.947	0.971
Mainland and Island	Cindy	1.028	0.989
	Dennis	**1.005**	0.972
	Katrina	0.981	0.994

Table 4.11: Statistics for 2005 storms for points only on the mainland (top), only on the three islands (middle), and on all points (bottom). Values closest to 1.000 for each storm are bolded.

Morphology- Island Area & Volume

The area and volume of West Petit Bois + Petit Bois Islands, Dauphin Island, and all three islands above 0 m NAVD88 were computed for each DEM. The change over time for simulated and LiDAR DEMs were studied separately and compared to the area and volume of the original Post-Ivan DEM (Figure 4.8). On Dauphin Island, island area was well-predicted until some time between Hurricane Ida (2009) and Nate (2017), when simulated area begins to exceed observed island area. The 2020 LiDAR dataset lacks data for northern Dauphin Island, leading to underestimations in area and volume for this time step. Simulated DEMs consistently underestimate island volume before 2018.

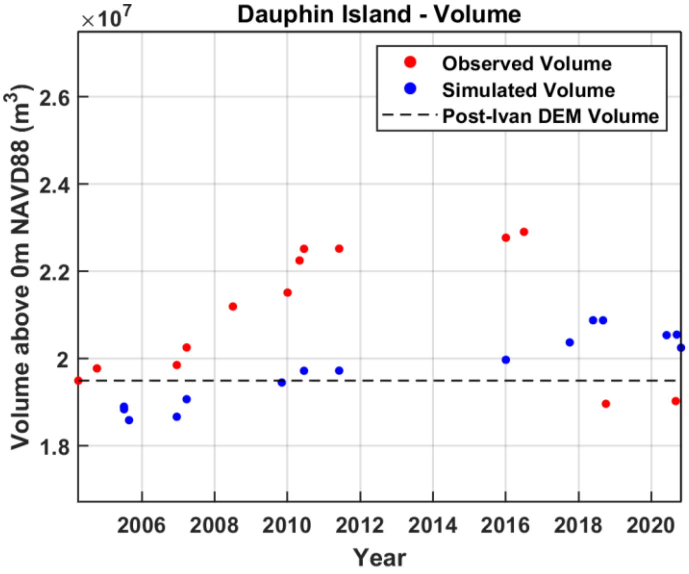

Figure 4.8: Simulated and observed volume of Dauphin Island, including beach nourishment.

For Petit Bois Island, simulated island area increased over time, while observed area decreased over time. Simulated area begins to diverge from the observed early in the study period, just after Hurricane Katrina (2005). Observed volume exceeds the simulated volume until some time between Hurricanes Ida (2019) and Nate (2017). After Hurricane Nate (2017), observed island volume decreased, while simulated volume increased. Due to the overestimation of area and underestimation of volume, simulated average elevation was about 0.2 m greater than observed (Figure 4.9) on both West Petit Bois/Petit Bois and Dauphin Islands.

For total area of the three islands, area was fairly accurately predicted until 2010. After 2010, simulated DEMs begin to overestimate island area. The error increased over time after 2010. The simulated DEMs underestimate island volume until 2018. After 2018, the simulated island volume begins to exceed the observed. After Hurricane Arlene (2005), island volume decreased drastically (by ~8.9e5 m^3), while total area increased by relatively little (2.0e5 m^2). Similar trends were present on both Petit Bois and Dauphin Islands; in all cases the final simulated area and volume both exceeded the observed value.

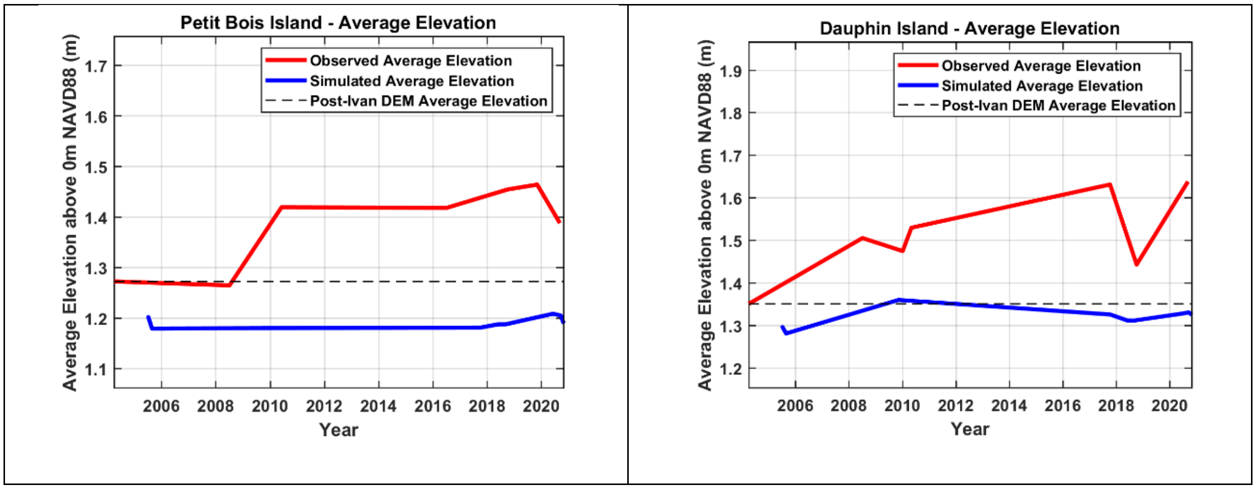

Figure 4.9: Average elevation of Petit Bois & West Petit Bois Islands (left) and Dauphin Island (right), without adjustment for anthropogenic beach nourishment/restoration activity.

Morphology- Island Transects

Peak dune elevation, peak dune height location, island cross-sections (dune profiles), locations of the 0-meter intercept, island width, and island midpoint were calculated at each transect (Figure 4.10). Observations were compared to the simulated values at the nearest time step.

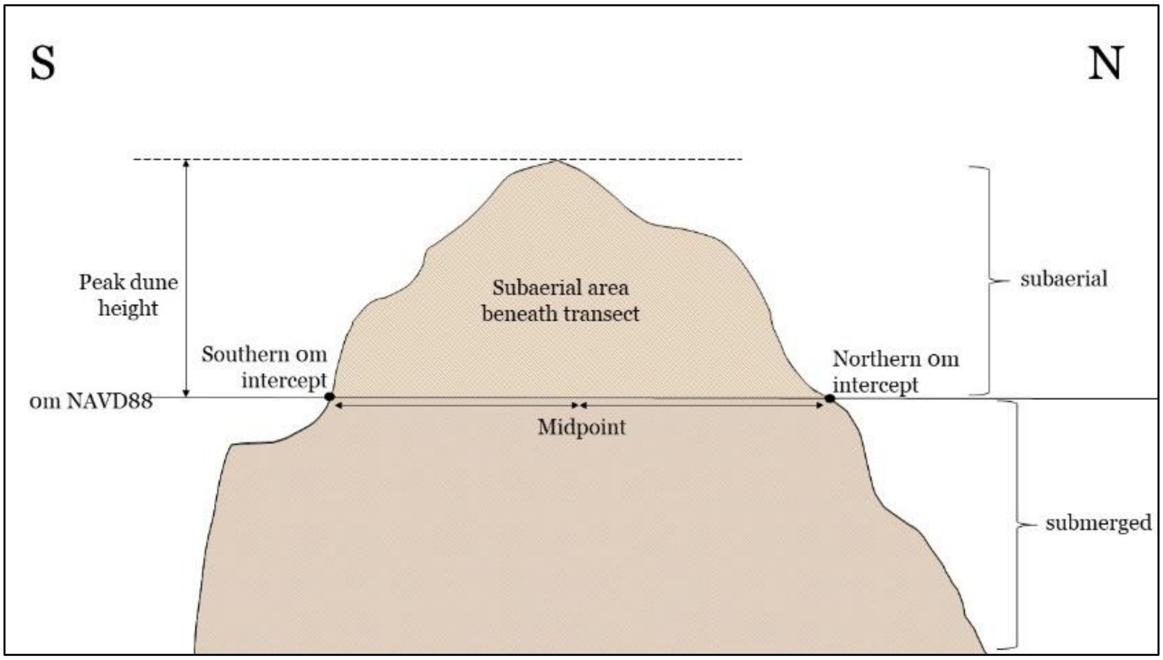

Figure 4.10: Island transect measurements.

Observed DEM	**Simulated DEM**	**Time Difference**
2008 CoNED	Post-Katrina (2009)	16 months
January 2010 LiDAR		2 months
May 2010 LiDAR		6 months
June 2010 LiDAR		7 moths
2016 LiDAR	Post-Ida (2017)	15 months
2018 LiDAR	Post-Alberto (2018)	1 month
2019 LiDAR	Post-Gordon (2020)	7 months
2020 LiDAR	Post-Cristobal (2020)	< 1 month
	Post-Sally (2020)	1 month

Table 4.12: Observed DEMs and the corresponding simulated DEM at the nearest time step

Post-Katrina (XB) vs. July 2008 LiDAR

The Post-Katrina XBeach DEM represents topobathy at October 2009, just prior to Hurricane Ida. All 39 island transects were studied. Low RMSE and MN Bias (1.21 m and 0.10, respectively) indicate good agreement of simulated and observed peak dune heights (). The peak dune height was simulated to be, on average, 63.6 m away from the one observed by LiDAR. Transect 1 has two dunes of similar height (Figure 4.12); the observed and simulated DEMs showed different dunes being the maximum. Therefore, the difference in location between maximum dunes was 456 m. When the peak dune location was adjusted for the same dune to be selected, mean absolute error was reduced to 56.3 m.

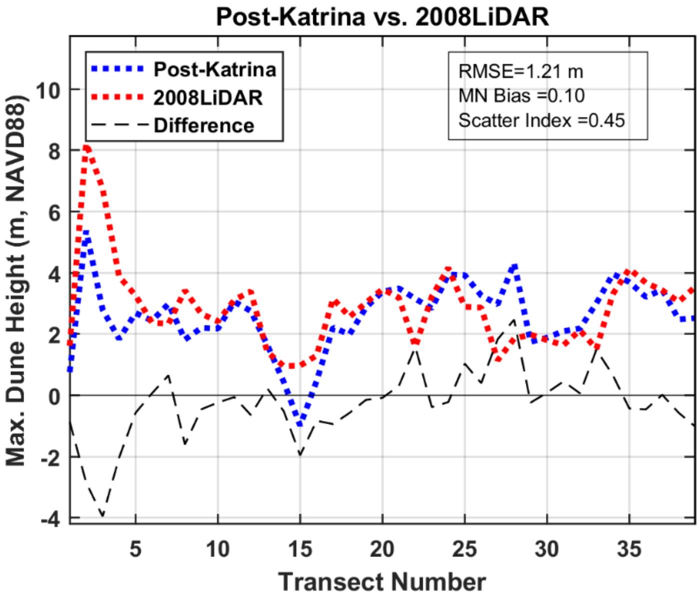

Figure 4.11: Peak dune heights at all 39 transects.

hen all transects were considered, RMSE in elevation across the entire dune profile is, on average, 3.65 m. When only aboveground points were considered, this value decreased to 0.7 m. On average, the aboveground area beneath the transects were underestimated by 30.0 m^2. Underestimation of the area beneath transect 2 was greatest, with 752.7 m^2 difference between simulated and observed area.

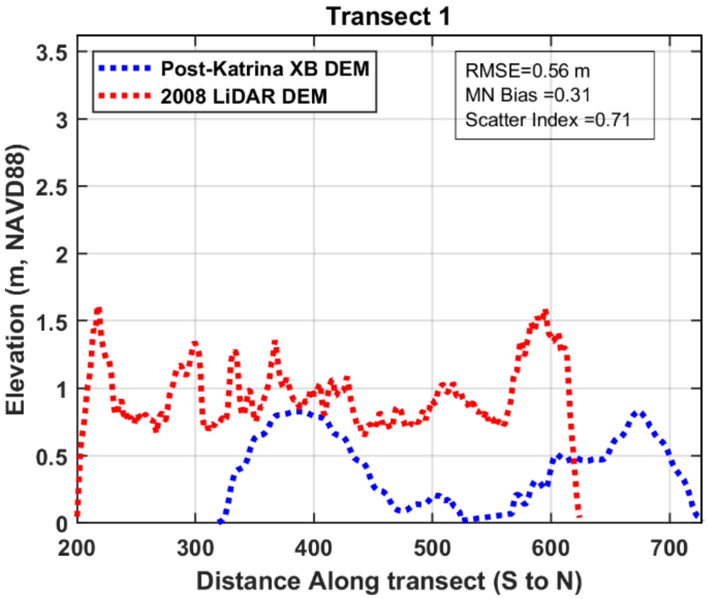

Figure 4.12: Dune profile at transect 1 for Post-Katrina and 2008 LiDAR DEMs.

On average, island width was accurately predicted (Figure 4.13), with an average overestimation of 30.9 m across all transects, and average overestimations of 80.5 m and 19.3 m on Petit Bois (excluding West Petit Bois) and Dauphin Islands, respectively. Transects 2, 13, and 28 had the largest error in transect width (Figure 4.14), with transect 2 underestimating width by 229 m, and transects 13 and 28 overestimating width by 367 and 261 m, respectively. Island midpoint was also poorly simulated at transect 13, with an error of 211.5 m to the south. The average transect midpoint across all transects was predicted to be 26.5 m further south than LiDAR data placed it. On Dauphin Island, the average simulated transect midpoint was 35.0 m south of observed data, and on Petit Bois Island (excluding West Petit Bois Island), the average error was 32.9 m to the south. Shoreline location was well-estimated by the morphological simulations; simulations placed the southern shoreline, on average, 44.1 m further south than LiDAR observations, and the northern shoreline an average of 8.9 m to the south. Only transects

2 and 13 had errors in shoreline location >200 m (Figure 4.14), with the southern shorelines being placed 223 m too far north for transect 2, and 395 m to the south at transect 13.

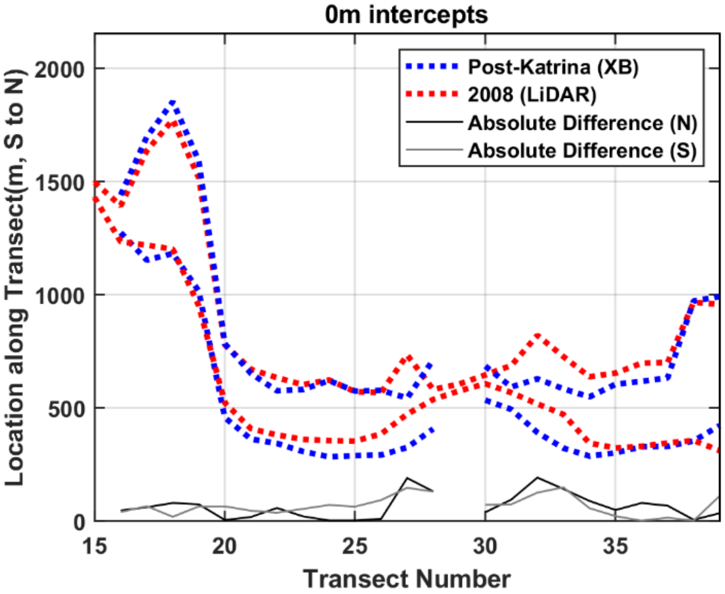

Figure 4.13: 0-meter intercepts for transects 15-39.

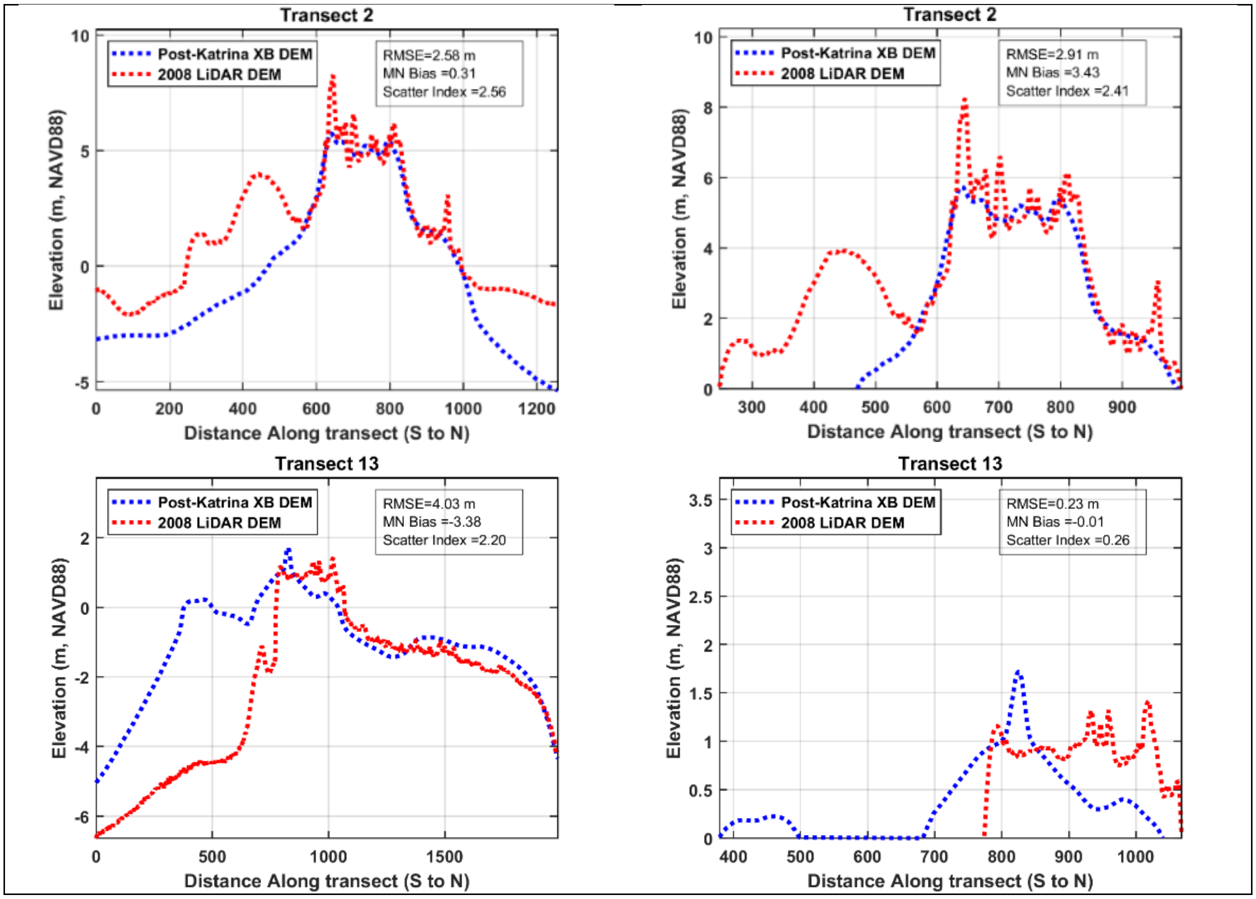

Figure 4.14: Dune profiles for transects 2(top) and 13 (bottom) across the entire profile (left) and for only aboveground points (right).

Post-Katrina (XB) vs. January 2010 LiDAR

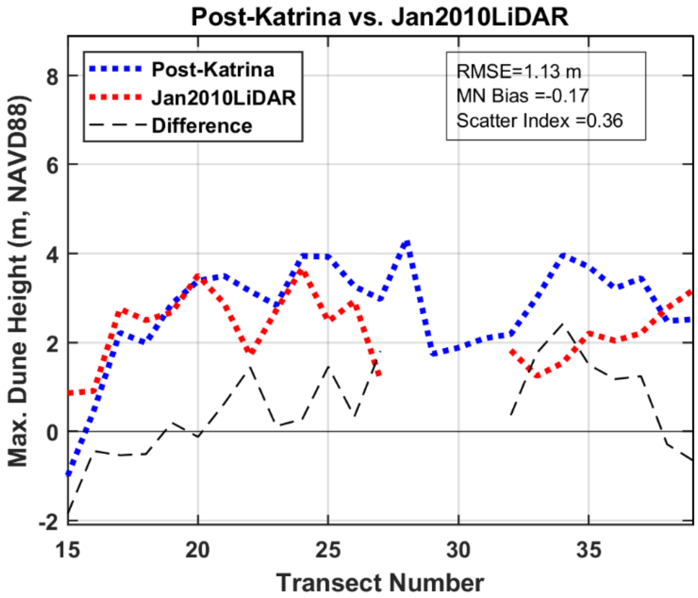

Figure 4.15: Peak elevations for transects 15-39.

21 island transects, all located on Dauphin Island, were studied. The simulated Post-Katrina DEM displays little bias (MN Bias = -0.17) in peak dune height predictions, with an RMSE of 1.13 m (Figure 4.15). Overestimation of peak elevation was most obvious at transect 32-37, on eastern Dauphin Island (Figure 4.3). Average error across the entire island cross section is presented in Table 4.13. The subaerial area beneath the island transects were, on average, underestimated by 41.0 m^2. The only locations where area was overestimated was at transects 18, 25, and 26 on western Dauphin Island (Figure 4.3**Error! Reference source not found.**). Absolute error in peak elevation location was 57.9 m. Error was greatest for transects 18 and 32, which fail to resolve the highest observed dune altogether.

Location	Transect #	All Points			>0 m NAVD88 only		
		RMSE	MN Bias	SI	RMSE	MN Bias	SI
All Transects	15-39	3.37	-2.92	1.64	0.62	0.35	0.68

Table 4.13: Error across the entire island transect, averaged for all transects.

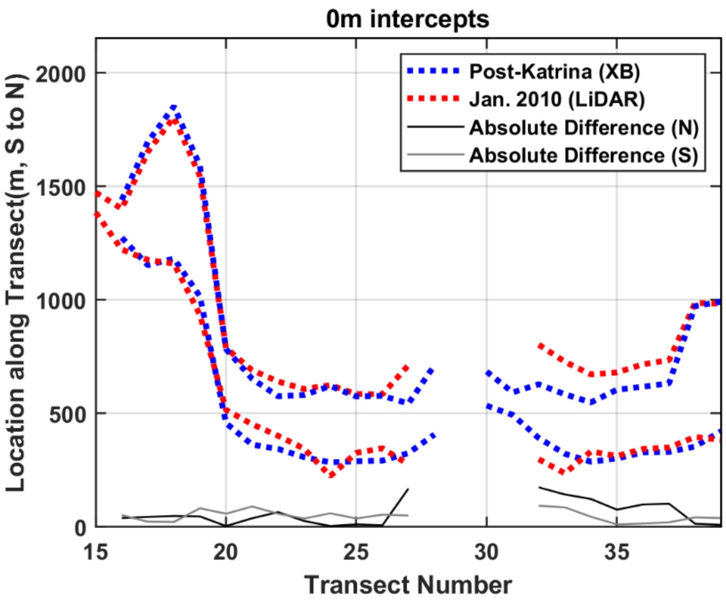

Figure 4.16: 0 m intercepts for Post-Katrina and January, 2010 LiDAR DEMs.

The Post-Katrina XBeach DEM and the January, 2010 LiDAR data showed good agreement when island width was considered (Figure 4.16), with an average underestimation of 45.3 m. Transect 32 showed the greatest variation, with the Post-Katrina DEM underestimating width by 267 meters. Average midpoint location was simulated to be, on average, 43.7 m further south than LiDAR data placed it.

Post-Katrina (XB) vs. May 2010 LiDAR

21 island transects, all located on Dauphin Island, were studied. There was no substantial over- or under-estimation of peak elevation, indicated by the low MN Bias of 0.24 (Figure 4.17). The Post-Katrina DEM overestimated peak dune heights at transects 19-37. Aboveground area beneath the island transects were accurately simulated, with an average underestimation of 36.0 m^2. The peak dune location was poorly simulated at transects 18 and 32, where peak elevation was located 263 m north and 180 m south of where LiDAR data placed it, respectively. Average absolute error in peak dune location was 53.6 m. Island width was fairly accurately simulated at all transects (Figure 4.18) except 27, 32, and 33, all underestimating width by >200 m. On

average, island width was underestimated by 35.9 m. Simulations placed the midpoints of transects, on average, 90.5 m further south than observed by LiDAR.

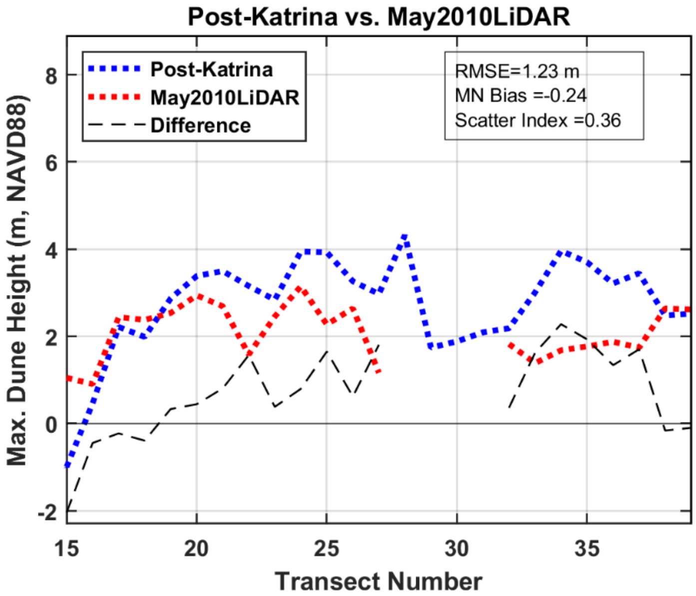

Figure 4.18: Maximum elevations for transects 15-39.

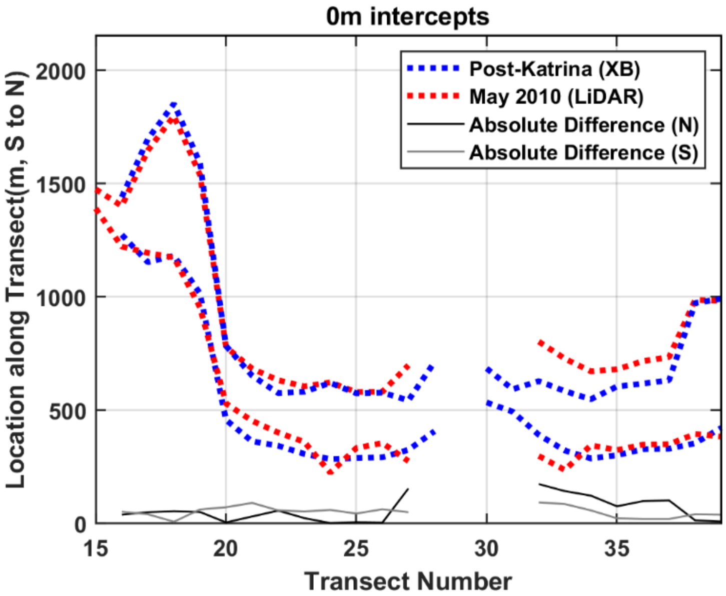

Figure 4.17: Observed and simulated 0-meter intercepts.

Post-Katrina (XB) vs. June 2010 LiDAR

14 island transects located on Petit Bois (12) and West Petit Bois (2) islands were compared. Peak dune heights were underestimated at most transects (Figure 4.19). RMSE is greater when entire transects were considered versus when only aboveground points were

considered (RMSE = 2.83 vs 0.84 m, respectively). For aboveground points only, error was greater on West Petit Bois Island than on Petit Bois Island, though when all points were considered, error was greater on Petit Bois Island (Table 4.14). The area beneath the transects were consistently underestimated, with an average underestimation of 100.6 m^2; area was overestimated at transect 5 only.

Location	Transect #	All Points			>0 m NAVD88 only		
		RMSE	MN Bias	SI	RMSE	MN Bias	SI
All Transects	1-14	2.83	-1.87	2.01	0.834	0.50	0.67
West Petit Bois	1-2	2.29	-0.75	2.08	1.72	1.42	1.43
Petit Bois	3-14	2.93	-2.06	2.00	0.69	0.35	0.54

Table 4.14: Average error across the entire dune profile for Post-Katrina (October 2009) morphology versus June 2010 LiDAR observations.

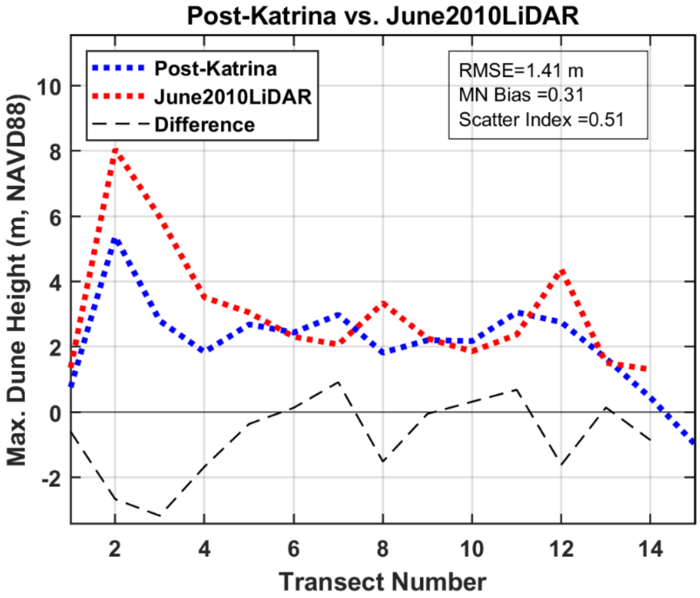

Figure 4.19: Maximum elevations along transects 1-14.

The location of the peak dune was simulated to be, on average, 4.9 m further back on the transect (further north) than LiDAR data placed it, though the average absolute difference was 95.9 m. Error was greatest at transects 1 and 12; both of these transects had two peaks, and different peaks were the greatest for observed and simulated DEMs. When transects 1 and 12 were adjusted so the same dune was selected as the peak for both simulated and observed DEMs, average absolute error was reduced to 57.5 m.

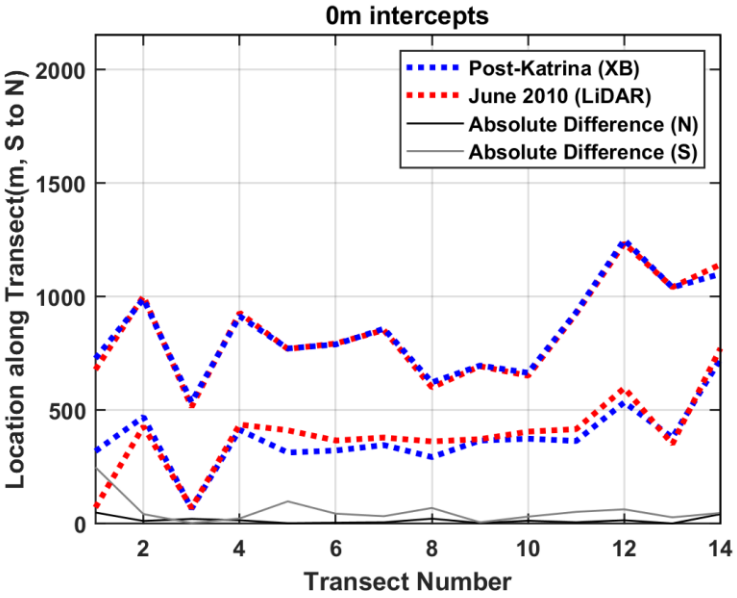

Figure 4.20: Observed and simulated 0-meter intercepts

The 0-meter intercept location was well-predicted on Petit Bois Island (transects 3-14), especially on the north side of the island (Figure 4.20). On average, island width was overestimated by 36.8 meters on Petit Bois Island, and underestimated by an average of 145 meters on West Petit Bois Island. Underestimates were very different between the two transects on West Petit Bois Island, with simulations underestimating width by 19 m at transect 1, and by 54 m at transect 2. On average, the midpoint of Petit Bois Island was simulated to be 17.29 meters to the south of where the LiDAR data placed it. For West Petit Bois Island, midpoint location was simulated to be an average of 81.8 meters further north than LiDAR data placed it; the error for transect 1 was much larger than that for transect 2 (148.5 versus 15 meters difference in midpoint location).

Post-Ida (XB) vs. 2016 LiDAR

The Post-Ida XBeach DEM represents topobathy at September 2017, just before Hurricane Nate (2017). 39 island transects across West Petit Bois (2), Petit Bois (14), and Dauphin Island (23) were compared. Simulated peak dune heights were generally accurate, with

RMSE = 1.21 m and a low MN Bias of 0.15 (Figure 4.21), averaged across all transects. Peak elevation location was well-predicted, with a majority of transects (25/39) predicting the maximum elevation within 30 m of observed data. Error was greatest at transects 1, 14, and 32. Average absolute error in peak dune location is 52.1 m. Peak dune height estimates were most accurate at and around Katrina Cut (transects 29-32).

When the entire dune profile was considered, average RMSE across all transects was 3.64 m; when only aboveground points were included, RMSE decreased to 0.80 m. On average, the area below the transect but above 0 m NAVD88 was underestimated by 13.6 m^2. This was caused by a fairly even split of over- and underestimated transects (18 vs. 21, respectively); absolute error was 105.0 m^2.

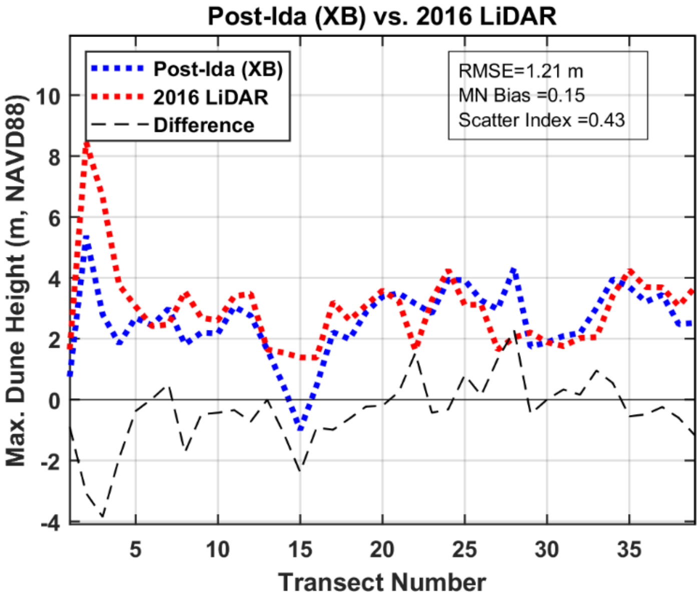

Figure 4.21: Observed and simulated peak dune heights for transect 1-39.

0-meter intercepts (Figure 4.22), island width, and island midpoints were taken at all transects. For transect 15, XBeach predicted no aboveground data. On Petit Bois Island, island width was overestimated by XBeach due to placement of the southern shoreline an average of 115.4 m further south than LiDAR data placed the 0 m contour. XBeach also placed the northern shoreline an average of 18.2 meters further north than LiDAR data, increasing island width by

133.6 m, on average. Simulations placed the midpoints of the Petit Bois Island transects an average of 48.6 m further south than observed by LiDAR.

On Dauphin Island, island width was also overestimated by XBeach, especially at the transects just to the east and west of Katrina Cut (transects 28 and 31, by 318 and 197 meters, respectively). The width of Dauphin Island was overestimated by 77.6 m, on average, across transects 16-39. These overestimations were largely due to the southern shoreline being predicted, on average, 89.0 meters further south than LiDAR placed it. The northern shoreline was also predicted to be 11.5 meters further south than LiDAR data placed it. The location of island midpoints was therefore predicted to be 50.3 m further south than observed by LiDAR.

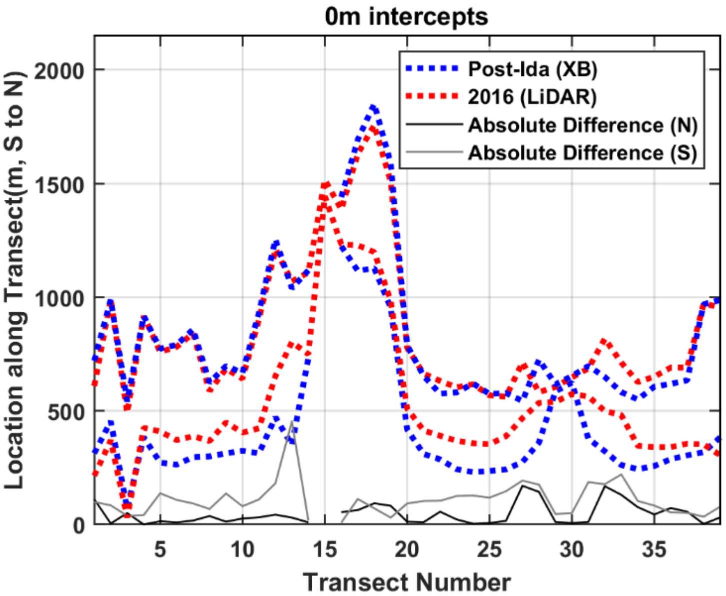

Figure 4.22: 0-meter intercepts at all 39 transects.

Post-Alberto (XB) vs. 2018 LiDAR

The Post-Alberto DEM represents topobathy for August 2018. All 39 island transects were compared. Simulated peak dune heights showed no evidence of consistent over- or under-estimation, evidenced by a low MN Bias of 0.09 (Figure 4.23). Average absolute error in peak dune location was 56.64 m. Average RMSE across all transects was fairly low (0.74 m) when only aboveground (>0 m NAVD88) points were considered. This increased to 3.68 m when the entire transect was considered, indicating relatively poor model representation of nearshore bathymetry compared to subaerial topography (e.g. Figure 4.24). The simulated Post-Alberto DEM was the first that overestimated subaerial area beneath the island transects when compared to the 2018 LiDAR data, simulations overestimate area by 65.3 m^2, on average.

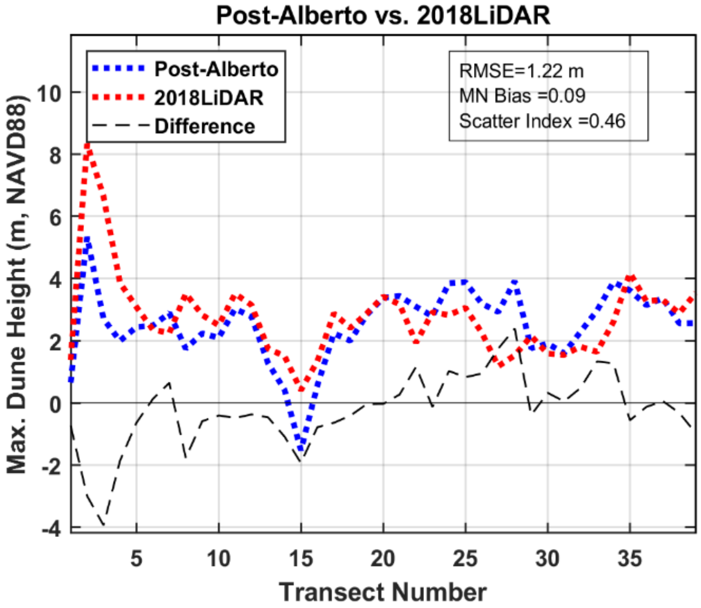

Figure 4.23: Simulated versus observed maximum dune heights along transects 1-39.

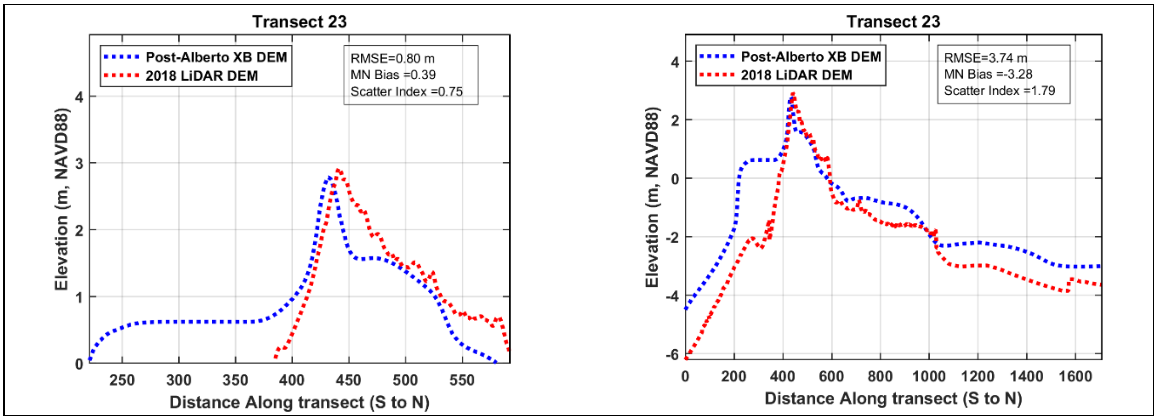

Figure 4.24: Simulated versus observed beach profiles for aboveground only (left) and all (right) locations at Transect 23 on western Dauphin Island.

The simulated DEM predicts a wider island footprint on average across all transects (123.3 m wider than LiDAR data). On average, Petit Bois Island was predicted to be 182.08 m wider than LiDAR data, and Dauphin Island was overestimated by 112.96 meters, on average. Island widths were most drastically overestimated at transects 12 and 13 on eastern Petit Bois

Island by 307 m and 479 m, respectively, and at transect 28 on the western side of Katrina Cut by 326 m. The footprints of Petit Bois and Dauphin Islands were, on average, predicted to be 70.63 and 62.7 m further south than observed. This shift was primarily due to model error in predicting the southern shoreline of the islands; morphological models placed the shoreline 161.7 and 119.2 meters too far to the south on Petit Bois and Dauphin Islands, respectively.

Post-Gordon (XB) vs. 2019 LiDAR

The Post-Gordon DEM represents topobathy for May 2020. 2019 LiDAR data was only available for West Petit Bois and Petit Bois Islands. 14 transects were compared, with 2 located on West Petit Bois and 12 on Petit Bois islands. Peak dune heights were underestimated (RMSE = 1.62 m), at all transects except for 6 and 7, both located on central Petit Bois Island (Figure 4.25). Peak dune locations had an average absolute error of 77.71 m. Across the entire dune profile, when the elevations of only points above 0 m NAVD88 were considered, average RMSE = 0.92 m. When all points were considered, RMSE increased to 3.09 m. The average area beneath the transect was, on average, overestimated by 19.1 m^2, though the absolute error was 154.8 m^2. Nine of the 14 transects had an error >100 m^2.

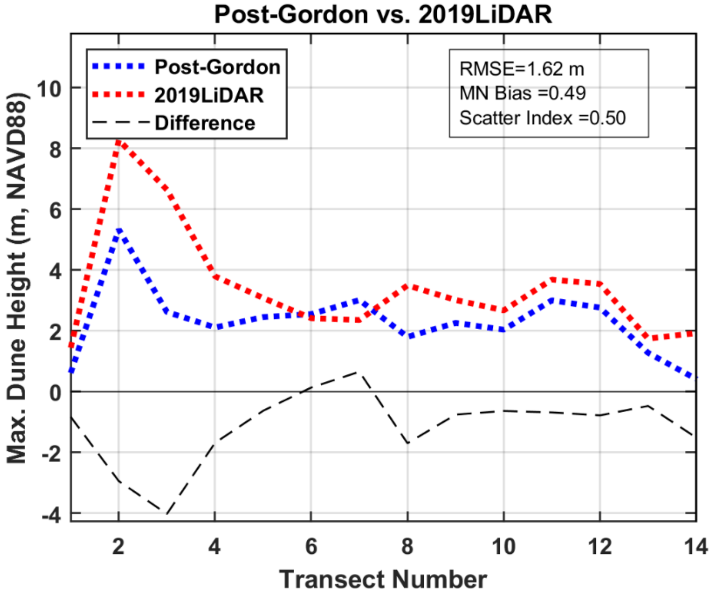

Figure 4.25: Peak dune heights along transects 1-14.

The Post-Gordon XBeach DEM placed the midpoint of West Petit Bois Island an average of 85.3 meters too far north, largely due to a northern shift in both the southern and northern 0 m intercepts on transect 1 by 199 and 139 meters, respectively. Morphological models overpredicted the width of Petit Bois Island by an average of 169.5 meters. The overprediction was especially pronounced on the east side of the island at transects 12 and 13 (312 and 443 meters overprediction, respectively). Transect 14 had a much smaller overestimation of 106 meters. The simulated transect midpoints were located further south than the LiDAR data placed them by an average of 60.9 meters. The change in island midpoint was greatest at transect 13, primarily due to placement of the southern shoreline 479 meters further south than observed by LiDAR.

Post-Cristobal (XB) vs. 2020 LiDAR

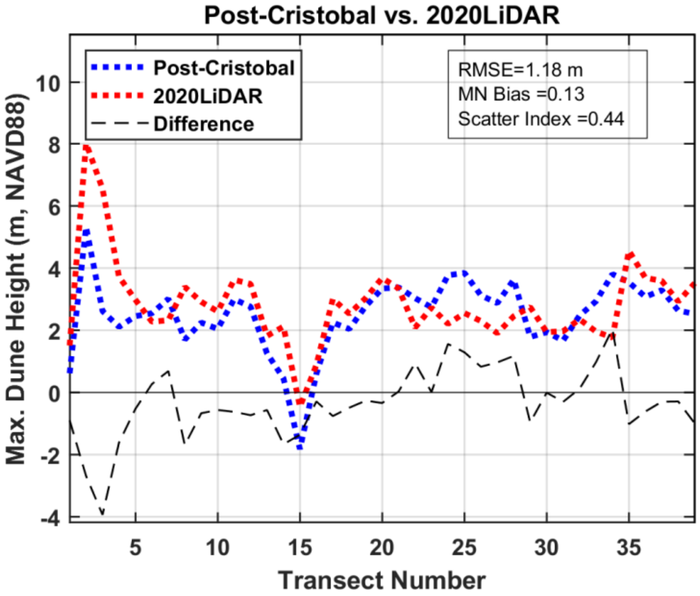

Figure 4.26: Simulated versus observed maximum dune heights at transects 1-39.

The Post-Cristobal DEM represents simulated topobathy as of August 2020. All 39 transects were compared. Peak dune heights displayed low MN Bias of 0.13 and an RMSE of 1.18 m (Figure 4.26). Average absolute error in peak dune location was 63.49 m before transect

1 was corrected so that the same dune was flagged as the peak elevation, and 56.8 m after the corrections were applied. Subaerial area beneath the transect was, on average, overestimated by 49.8 m^2; absolute error was 117.0 m^2. When only aboveground points (elevation > 0 m, NAVD88) were considered, RMSE across the entire dune profile was, on average for all transects, 0.83 m. When all points were included, average RMSE increased to 1.99 m.

The location of West Petit Bois Island was simulated to be, on average, 77.8 m further to the north than LiDAR data placed it, based on the location of transect midpoints. This was mostly due to a 225 m error for the southern shoreline at transect 1 (Figure 4.27). The simulated footprint of Petit Bois Island was an average of 66.3 meters further south than the footprint according to the LiDAR data. The southern shore was simulated to be an average of 157.7 meters further south than the LiDAR footprint, and the north shore 25.1 meters further north, for an average increase in island width by 182.8 meters. The island width at transects 12 and 13 were the most overestimated (Figure 4.27), by 327 and 461, respectively.

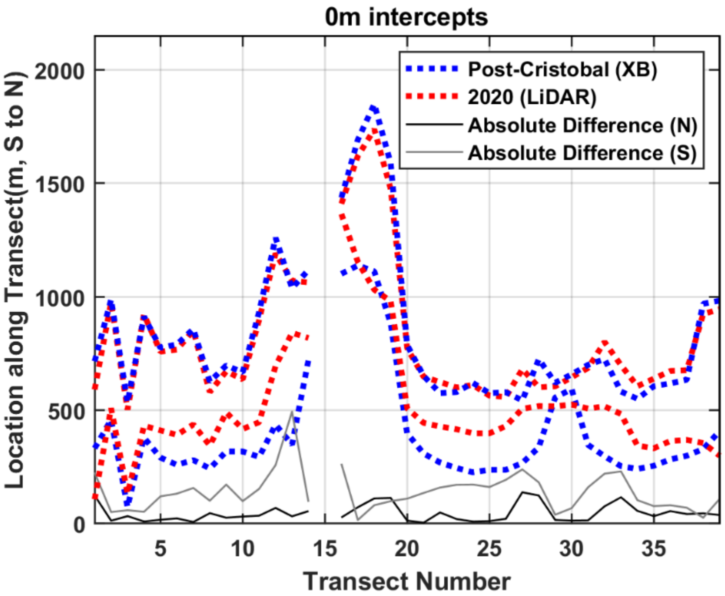

Figure 4.27: Northern- and southern-most 0-meter intercepts on transects 1-39. Transect 15 was fully submerged and therefore has no 0 m intercepts.

Across Dauphin Island, morphological models overestimate island width (Figure 4.27) by an average of 109.0 meters. At transect 16, island width was predicted to be 336 meters, while LiDAR data showed an island width of 45 m, a 291-meter difference. This was primarily caused by the southern shoreline being placed 264 m further south than the LiDAR data located it. On average, the simulated transect midpoints were located 52.6 m further south than the LiDAR data suggests. This error was increased by overly southward predictions at transect 16 (118.5 meter difference in midpoint location) and transects 27, 32, and 33, immediately to the west and east, respectively, of Katrina Cut (188.5, 148, and 173 meter difference in midpoint location).

Post-Sally (XB) vs. 2020 LiDAR

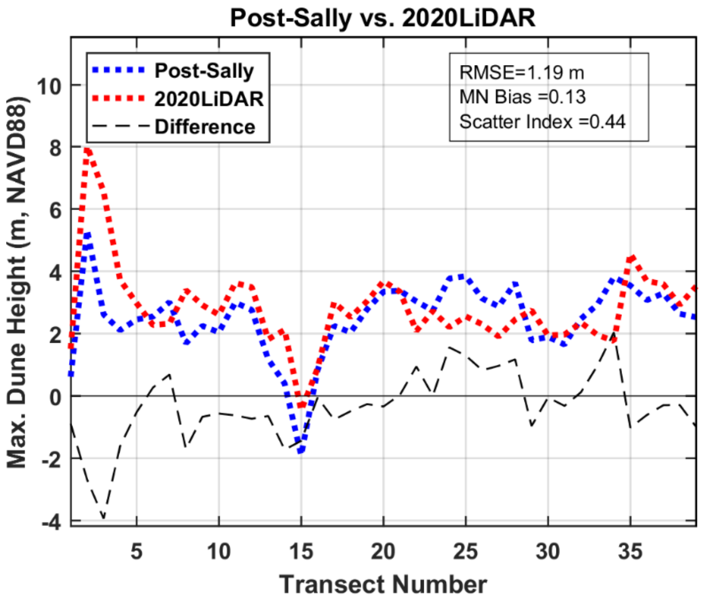

Figure 4.28: Observed and simulated peak dune heights for transects 1-39.

For the Post-Sally DEM, only storm-driven morphological change was simulated; dune recovery simulations were not completed. The Post-Sally DEM represents elevations for October, 2020. All 39 transects were compared. The location of peak elevation had a mean absolute error of 61.54 m. No corrections were necessary for transect 1. Simulated peak dune heights displayed low MN Bias (0.13) with an RMSE = 1.19 m (Figure 4.28). Across the entire dune profile, average RMSE was low when all transects were considered (1.62 m) and when only elevations above 0 m NAVD88 were considered (0.82 m) (Figure 4.29). The area beneath the transect but above 0 m NAVD88 was overestimated, on average, by 38.1 m^2.

Transects 1, 12, and 13 display the largest shifts in the location of the southern shoreline, with simulations placing the 0 m intercept 355 meters to the north, 258 m to the south, and 466 meters to the south, respectively. The error of the northern shorelines of West Petit Bois and Petit Bois Islands was, on average across all transects, 69 and 25.3 meters to the north, respectively. The southern shoreline of Petit Bois Island was predicted to be 151.2 m further south than observed, contributing to an average widening of the island by 176.5 meters. The simulated transect midpoints were located 63 .0 meters, on average, further south than the LiDAR data placed them (Figure 4.30).

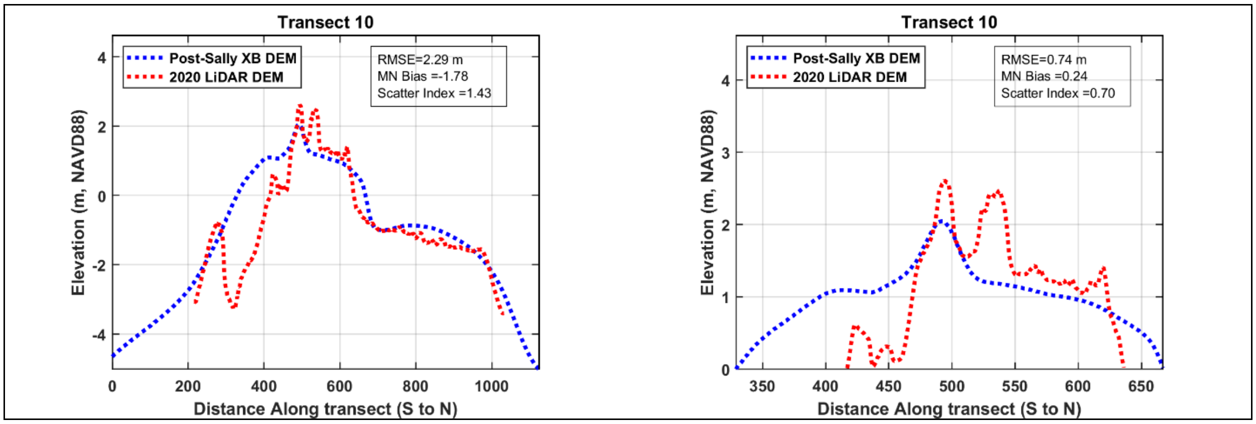

Figure 4.29: Dune profile across the entire island transect (left) and for the aboveground points only (right) at transect 10 on central Petit Bois Island.

On average across Dauphin Island transects, the southern shoreline was simulated to be 105.9 m too far to the south. Transects 16, 27, 32, and 33 had errors >200 m in southern shoreline location. The simulated location of the northern shoreline was highly accurate, on average being located 3.1 m further south than LiDAR data placed it. Only transect 32 had an error >200 m. Due to these southward shoreline errors, the average shift in island midpoint across all transects was 54.5 m to the south. Transect 32 had the greatest error in midpoint location, being 205.5 m further south than observed by LiDAR. On average, island width was overestimated by 102.8 m (Figure 4.30).

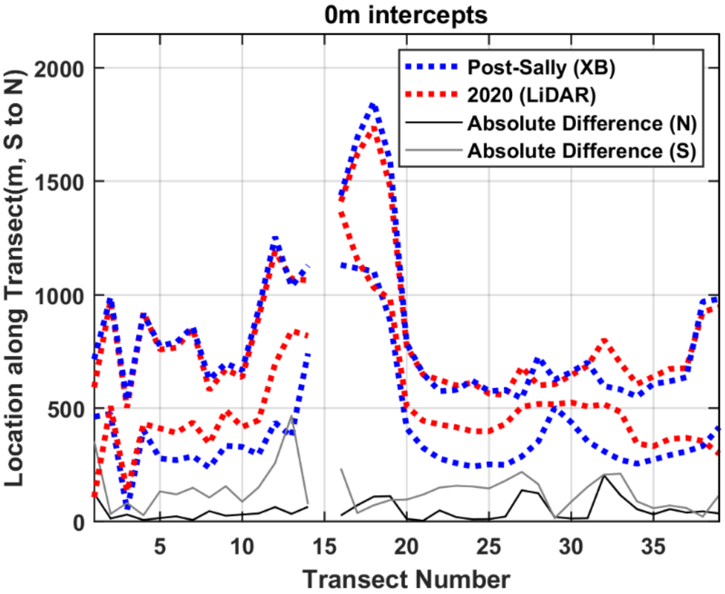

Figure 4.30: 0-meter intercept locations for the simulated Post-Sally DEM at transects 1-39.

CHAPTER 5

DISCUSSION

Hydrodynamics

Overall, WSE and waves were similar for all simulations run on each of the three DEMs, especially when compared to observed data. Offshore RMSE ranged from, on average, 19.2 cm for LiDAR DEMs to 20.4 cm for XBeach-derived DEMs across all storms and NOAA stations. Error for Post-Ivan DEMs was, on average, 20.2 cm (Table 4.2). These errors are consistent with those from other studies (Dietrich, Westerink, et al., 2011; Kerr et al., 2013) and indicate fairly good agreement between modeled and observed values. The 1 cm differences in RMSE for the WSE of simulations run on the three different DEMs represent a small and insignificant difference relative to the ~20 cm RMSE (Table 4.2). It is important to note that the quality of observed data is imperfect, especially during extreme conditions like TCs, and may contribute to some of these errors.

Differences in RMSE for WSE between DEMs was quantified. For the offshore NOAA Stations, differences ranged from, on average for all storms, 3.0 cm at NOAA Station #8745557 at Gulfport, MS, to 0.0 cm at Dog River Bridge, AL, about 10 miles south of Mobile, AL, on the west side of Mobile Bay. At Eastern Dauphin Island, AL, RMSE ranged from 13.9 cm to 15.0 cm (1.1 cm difference) (Table 4.2). This shows minimal influence of changes to the DEM on the quality of observed data between 0 to 100 km away from the nearest changes.

Observed HWM data were regressed against simulated peak WSE obtained from models run on the different DEMs. Minimal differences in model agreement were present when the regressions were compared. This is likely due to a combination of the large study area (200 km radius from Dauphin Island) needed to gather sufficient data to run regressions (e.g. Figure 5.1), and the lack of storms with well-documented data. There was also little to no data in the immediate study area (~10-15 points on Dauphin Island and 0 points on Petit Bois Island). Since hydrodynamic differences were most prominent in locations proximate to the morphological differences, the lack of nearby observations reduced the relevance of this metric. Future studies should improve water level data collection, especially on barrier islands and in uninhabited coastal areas.

WSE and significant wave height time series and peak values were compared between the three DEMs at nearshore points, points on the islands, and on the mainland (Figure 5.2). At all locations, XBeach and LiDAR DEMs performed most similarly for both significant wave height and WSE measurements (Figure 5.3). This indicates that simulating DEM updates improve hydrodynamic hindcasts compared to using the Post-Ivan (2004) DEM (Seymour, 2020) for the entire duration.

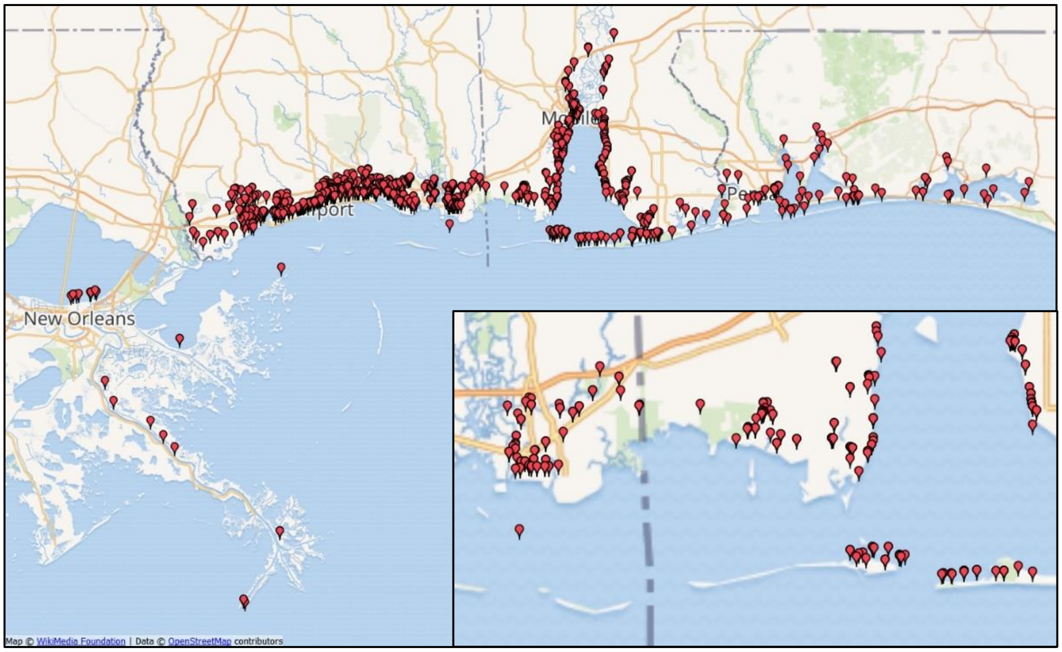

Map © WikiMedia Foundation | Data © OpenStreetMap contributors

Figure 5.1: Map of all observed HWM data points within 200 km of Dauphin Island. Inlay shows points most proximate to the study area.

Figure 5.2: a. Nearshore points (see Figure 3.6), b. On-island points (see Figure 3.7), and c. Mainland points (see Figure 3.8).

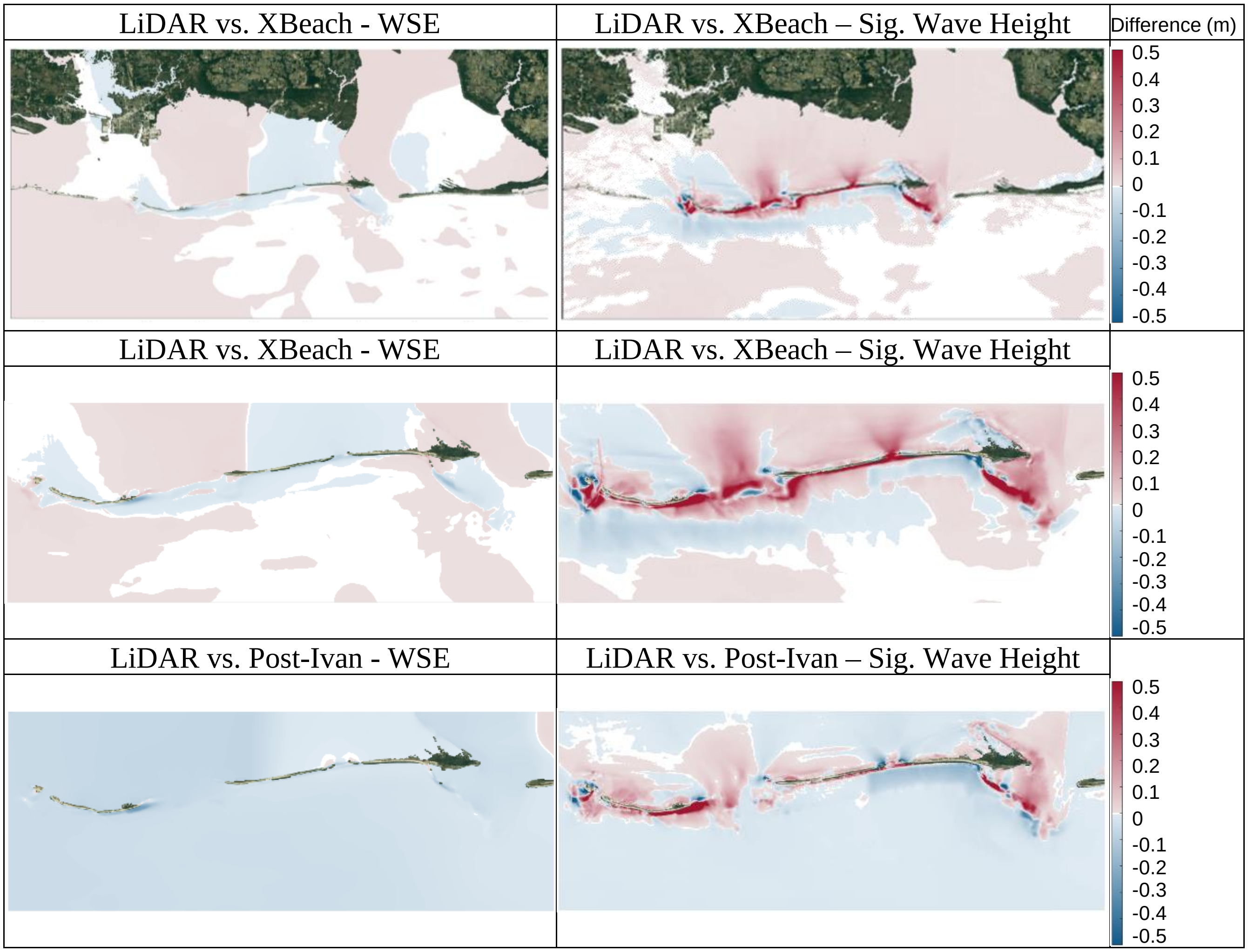

Figure 5.3: Peak WSE and significant wave height difference plots for Hurricane Ida (2009). Reds indicate LiDAR simulating greater values than XBeach (or Post-Ivan), and vice-versa for blue. The middle and bottom figures show zoomed-in images of the barrier islands for LiDAR vs. XBeach and LiDAR vs. Post-Ivan, respectively.

Differences between DEMs were most pronounced at dynamic locations with high morphological change, such as near Katrina Cut, between Petit Bois and Dauphin Islands, and near southeast Dauphin Island (Figure 5.3). For WSE, even the maximum differences at nearshore points (Figure 5.2a) were <12 cm, with an 11.7 cm difference at the southeasternmost point studied on Petit Bois Island during Hurricane Ida. On the back side of the islands, errors were even less. This indicates minimal impact of morphological changes to simulated WSE for points at -5 m depth (NAVD88). On the mainland shoreline (near 0 m NAVD88, Figure 5.2c), the only instances of differences >10 cm were during Hurricane Nate when the Post-Ivan and XBeach DEMs were compared. The highest errors all occurred north of Petit Bois Island. Average differences between DEMs were very low (<6.5 cm), suggesting that variations in WSE caused by minor changes to the barrier islands are highly localized, and likely depend on a number of factors such as storm track and intensity.

Significant wave heights followed a similar spatial pattern as differences in WSE between DEMs, but with greater differences in magnitude (Figure 5.3). Average RMSE for significant wave height time-series compared between DEMs ranged from 3.7-8.4 cm. However, when only peak wave height values were considered (as in Figure 5.3), differences on the front side of the island reached up to 91.3 cm for Hurricane Ida at point 14, near southeastern Petit Bois Island (Figure 5.4). This is a very morphologically dynamic area that is difficult to accurately model, especially for the storm in the study immediately following Hurricane Katrina, explaining the timing and location of the discrepancy. However, average peak differences between DEMs on the front side of the islands averaged around 0.427 m, showing that a difference this extreme was an anomaly.

The back side of the island experienced smaller average and peak differences in significant wave height, likely because of the substantial wave attenuation that the barrier islands offered (Figure 5.5). The greatest difference on the back side of the island was 65.7 cm, during Hurricane Gordon (2018) between Petit Bois and West Petit Bois Islands. Again, this is a dynamic and relatively poorly simulated area, morphologically, explaining the location of the discrepancy. Average peak differences were 22.6 cm, substantially less than the average difference on the front side of the island, and the peak difference for the back side of the islands.

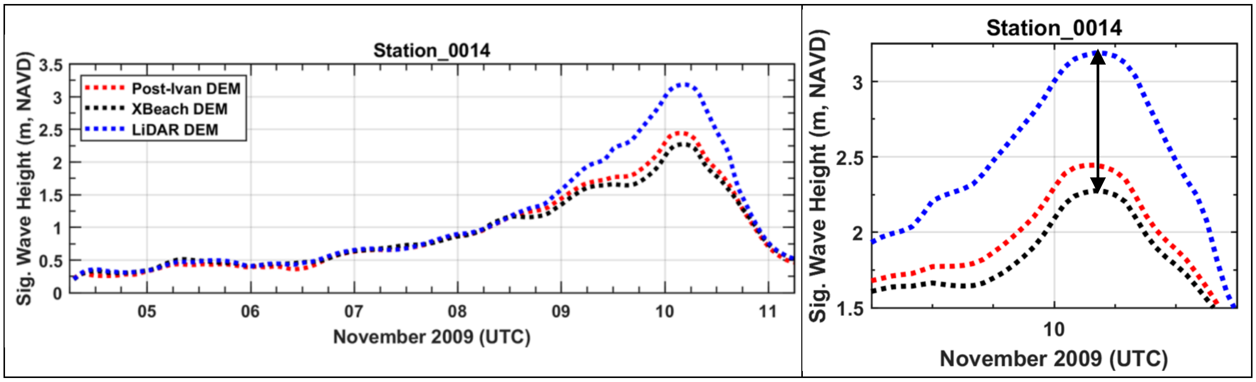

Figure 5.4: Time-series plot of significant wave height for Hurricane Ida at the station with the greatest difference between any DEMs for any storm.

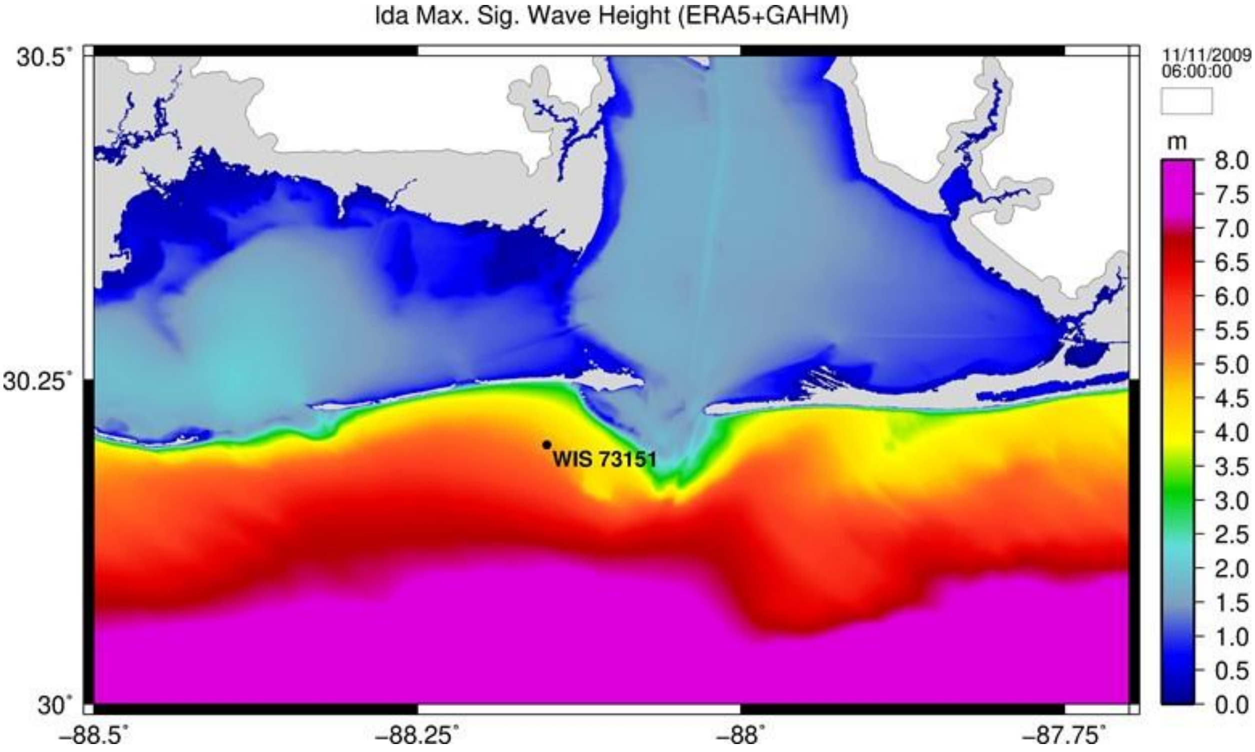

Figure 5.5: Significant wave height map for Hurricane Ida (2009), showing the decrease in significant wave height on the bay side of the islands.

When peak WSE was compared at mainland, on-island, and the mainland and on-island points together, agreement is very high ($R^2 > 0.95$) between all DEMs when all storms were plotted together. When individual storms were considered, all peak WSE regressions had greater correlation coefficients on the mainland than on the islands (Table 4.10, Table 4.11). This indicates a relationship between proximity to the morphological changes and the hydrodynamic impacts of these morphological changes.

Morphology

Simulated DEMs were consistently overly flattened, with lower peak dune heights and greater areas than observed by LiDAR. The overestimation of island area coupled with the underestimation of subaerial volume implies flattening of the island and offshore transport. Further studies should examine the flow path and ultimate location of the sediment that moves from the subaerial portion of the island.

Model performance tended to be best at undeveloped transects far from the open Gulf, such as central Petit Bois Island and parts of Western Petit Bois Island. Peak dune heights and locations may be most accurate on undeveloped transects because incorporating anthropogenic impacts into the morphological models is highly challenging. Additionally, the highest point along the transect is not necessarily the peak dune height; it may represent a road or some natural high-elevation area behind the dune. In developed areas, it is far more likely that the dune profile is tampered with by development or dune nourishment initiatives. These factors cannot be accurately accounted for in models. To remedy this, visual analysis of each transect is necessary, rather than automated extraction of the highest point.

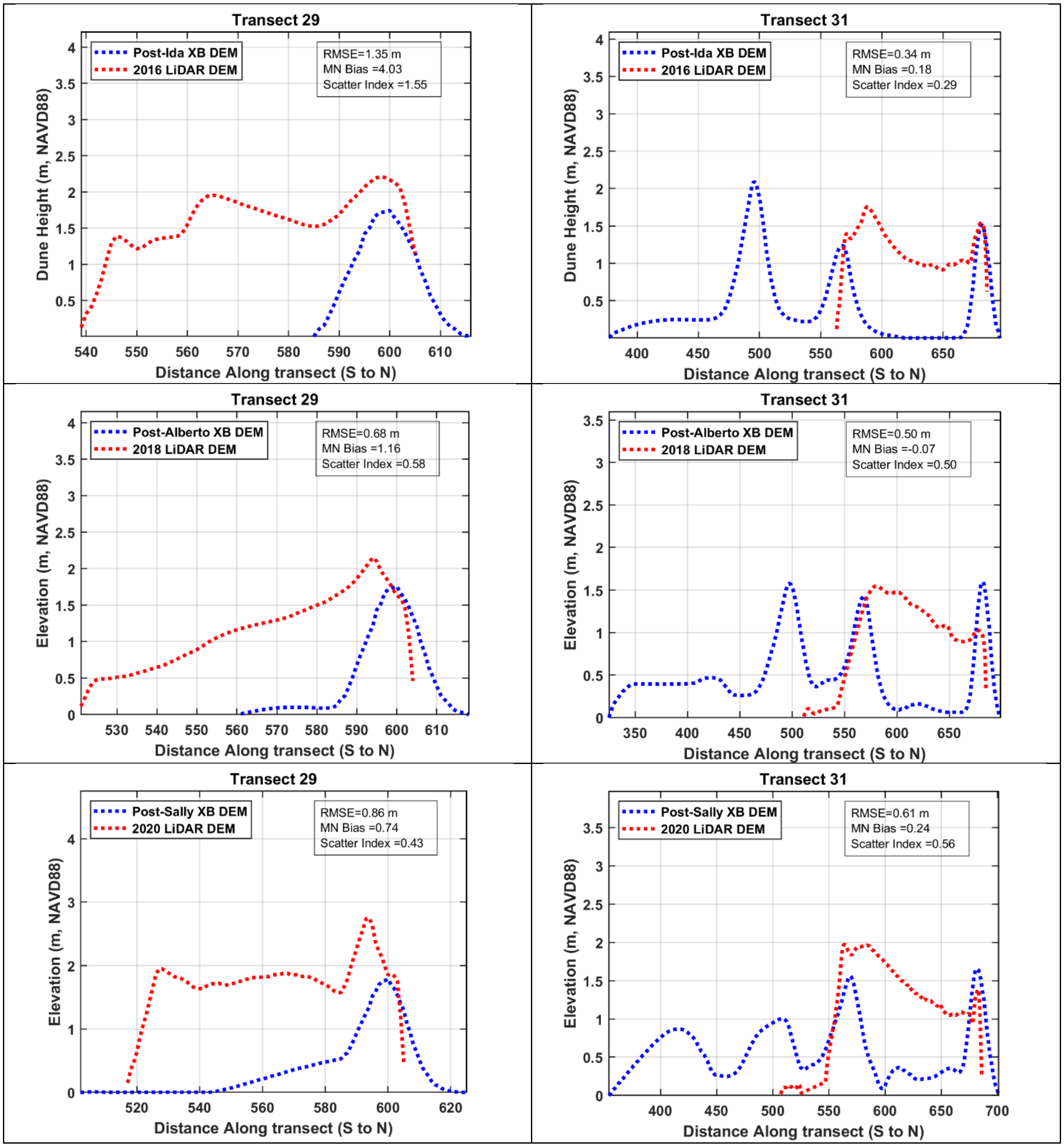

Figure 5.6: Aboveground dune profiles at transects 29 (left) and 31 (right) for 2016 vs. Post-Ida DEM (top), 2018 vs. Post-Alberto DEM (middle), and 2020 vs. Post-Sally DEM (bottom).

A shortcoming of numerical morphological models is the inability to include anthropogenic impacts to the island, including beach and dune nourishment efforts, infrastructure development, and post-storm recovery (i.e., clearing roads). For hindcasts, this can be remedied by ending the simulation prior to the beginning of some anthropogenic-driven change to morphology, adding the impacts of the human activity, then continuing the simulation. This was completed for this project during the installation of a rock wall at Katrina Cut in 2011; the EDGR model was paused, the DEM was edited to include the rock wall, then EDGR was resumed. This resulted in fairly accurate peak dune heights (e.g. Figure 4.21, Figure 4.26, & Figure 4.28), and peak dune location (Figure 5.6), though the shape of the dune profile, and the subaerial width of the island were poorly estimated (Figure 5.6). Though this method improves dune recovery simulations by including anthropogenic impacts, storm-driven morphological change and shoreline change during quiescent periods did not include any anthropogenic impacts. This hindcast only included the rock wall construction, and smaller human-driven morphological impacts were ignored. Including small-scale and future anthropogenic morphological impacts is more challenging and should be addressed in future projects.

Change in Error Over Time

It was hypothesized that the LiDAR and simulated (XBeach) DEMs would diverge from the Post-Ivan DEM, and each other, over time. In theory, errors in the morphological simulations would compound over time, reducing the accuracy of the simulated DEM when compared to the LiDAR data as the study period progresses. Because of the expected increase in morphological differences between 2005 and 2020, simulated WSE and significant wave heights were also expected to diverge.

For nearshore points (Figure 5.2a), error in WSE between Post-Ivan and XBeach and Post-Ivan and LiDAR DEMs did not increase over time. Rather, error is noticeably higher for Hurricane Ida. This is likely due to a combination of its position as next to be simulated after Hurricane Katrina, and four years apart chronologically from Katrina. During Hurricane Katrina, major morphological change occurred, and errors likely compounded as the empirical models were run during the quiescent period. However, comparisons between XBeach and LiDAR yielded consistent WSE error over time, including for Hurricane Ida (2009). This suggests that observed and simulated DEMs have a consistent level of error that does not change for multi-year time scales.

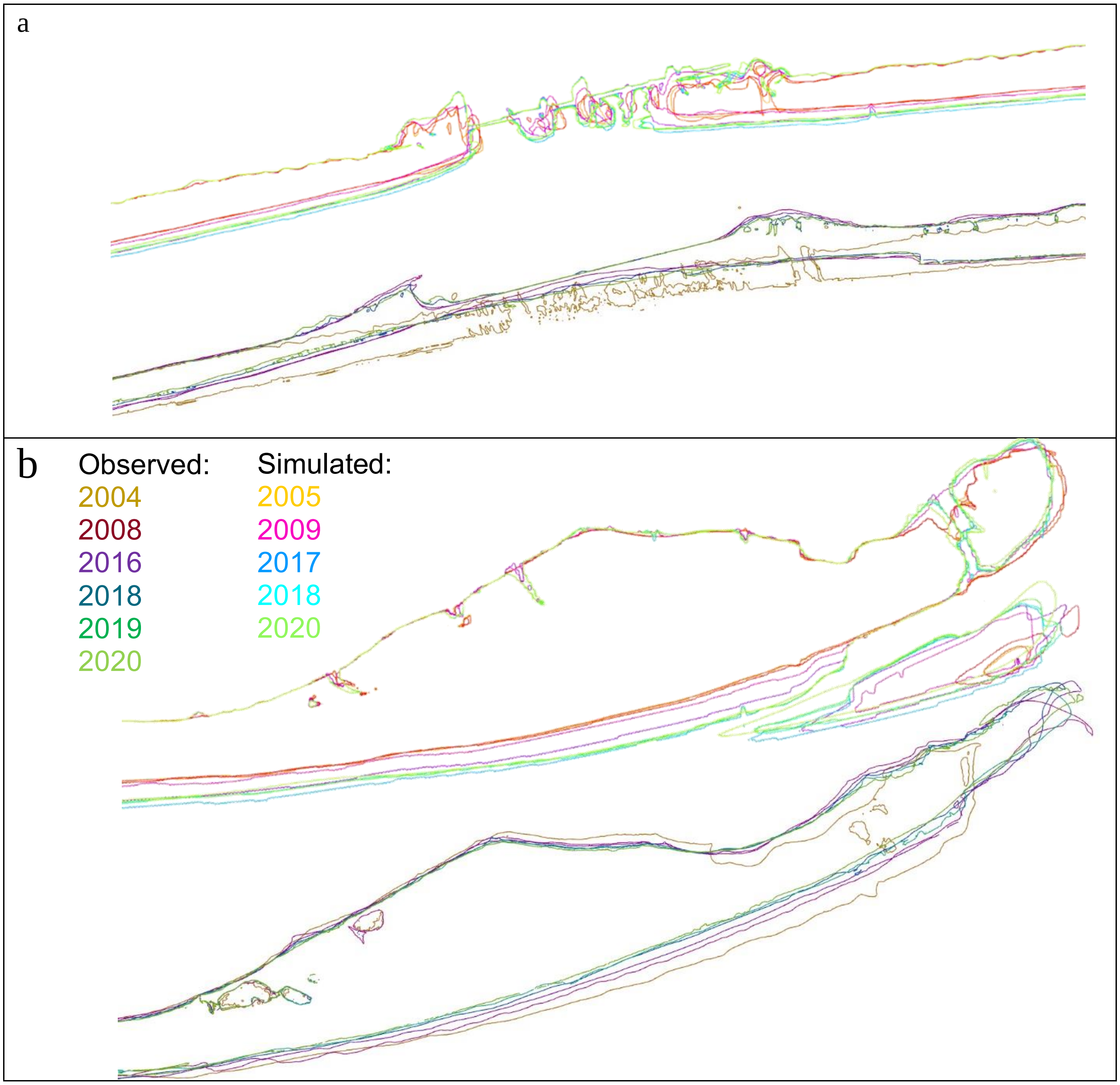

Figure 5.7: Simulated and observed 0 m contour change over time at a. Katrina Cut and b. Eastern Petit Bois Island (not to scale).

Simulated and observed 0 m contours were compared. Simulations predicted a southern shift in the southern shoreline over time and minimal change in the northern shoreline. However, observational data showed a northward migration of the southern shoreline over time, and slight movement of the northern shoreline (Figure 5.7, Figure 5.8). Therefore, the error in island width at many locations increased over time.

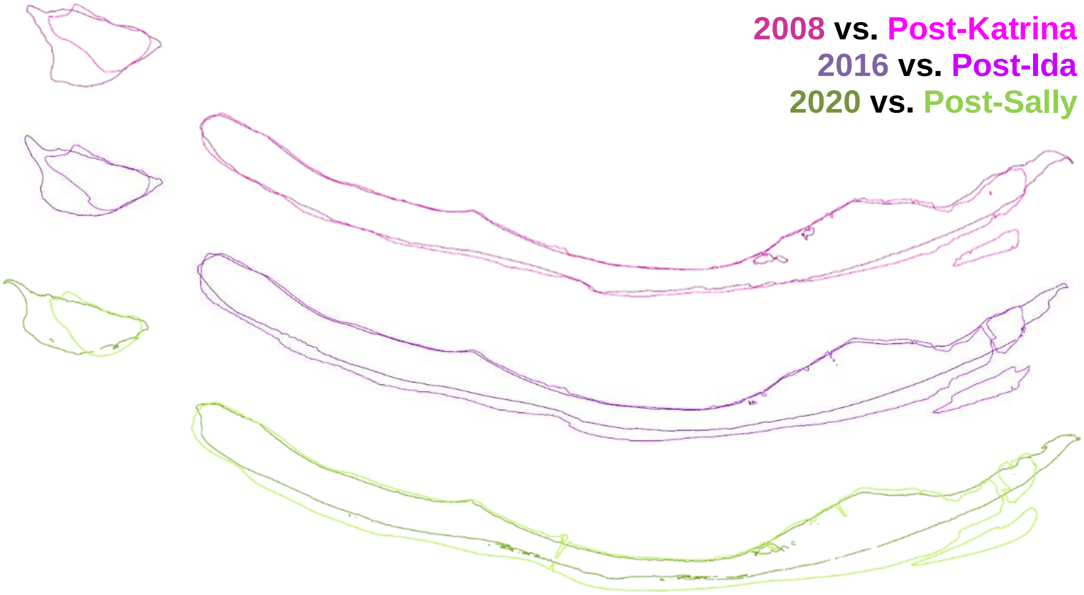

Figure 5.8: Observed and simulated 0 m contour of Petit Bois Island in 2008, 2016, and 2020.

The simulated area and volume diverge farther from the observations as time progresses. This is partially caused by incomplete LiDAR data for 2020, which excludes a small portion of northeast Dauphin Island (Figure 5.9). Even when corrected for the study period to end in 2018 (for Dauphin Island & all islands) or 2019 (for Petit Bois Island), the trend persists. For volume on Dauphin Island and all islands, observed island volume peaked around 2016 then decreased in 2018, while the simulated island volume increased with a relatively linear trend. This caused error to increase rapidly early in the study period, then continue to increase at a slower rate later in the study. Error increased exponentially over time for Dauphin, Petit Bois, and all islands together.

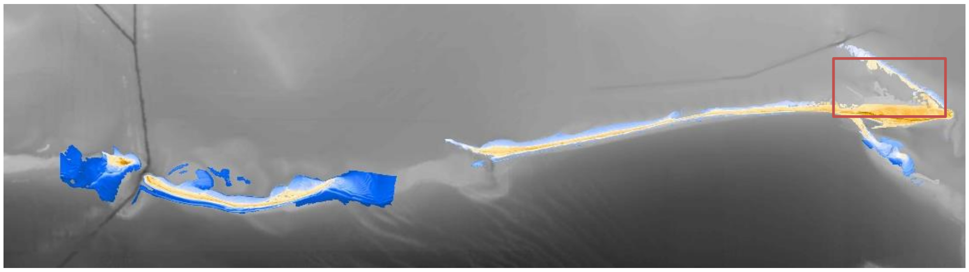

Figure 5.9: LiDAR data (colored) overlayed on the Post-Ivan DEM (black & white). Part of northeast Dauphin Island is not included in the LiDAR dataset.

Limitations, Recommendations & Future Work

This study could have been improved by more observational data to verify simulation results, and the inclusion of anthropogenic impacts in the morphological models. The comparison between both offshore WSE and wave data, and HWM data on land, could have been improved with more observational data. The observed WSE and wave data were limited to 14 and 4 NOAA stations, respectively. In addition, relatively few data collection buoys were present in the study area and had WSE data available during the 10 storms studied (Figure 3.1). Improving data collection methods during severe storms and abundance can help improve model calibration for local scales.

Alternatively, partner institutions could be contacted prior to the hindcast to obtain past observed data collected for other purposes or projects that can be used to verify the model. The amount and quality of observational data was particularly lacking in rural and undeveloped areas and on the barrier islands. Future work should involve a field component of the study area during at least one storm during the study period to better verify the model. The limited morphological data also limited the accuracy of the study; the LiDAR observations rarely aligned with the dates of the simulated DEMs. Even the small (~1 year) differences between these observations could encompass another TC, major storm, anthropogenic morphological change, and natural dune and shoreline changes, leading to greater model error than actually exists. An improvement in the frequency of LiDAR surveys existed throughout the study period.

Morphological model setup and performance reduced the accuracy of some morphological results. For example, shoreline change during quiescent periods consistently overestimated island width, especially on the south side of the islands. This is most likely due to a combination of several model simplifications. Alongshore sediment transport was not included in the shoreline change model; some of the sediment that migrated offshore in the southward direction was likely swept westward with the current (Rosati & Stone, 2009) either onto another transect or out to sea. This trend was not observed on the north side of the island primarily because shoreline change was only resolved on the Gulf side of the islands due to a lack of observed shoreline change data for the back side of the islands. Additional error was likely introduced because XBeach was not forced with winds, which could contribute to some proportion of observed sediment transport via currents.

The inability for the model to account for anthropogenically-driven morphological change also hindered the study. On Dauphin Island especially, dune nourishment and post-storm clean up are frequent due to the economic importance of the island to the state of Alabama. The anthropogenic changes would have to be input manually, such as for the rock wall at Katrina Cut in 2011; these projects occurred frequently and on relatively small scales, and budgetary and time constraints limit the amount of detail that can be afforded for these morphological projects. This presents further challenges for forecasts, as human activity is notoriously difficult to predict; beach nourishment and road clearing projects rely heavily on tax revenue and state and federal budgets, which change between administrations and on decadal scales as the economy grows and recesses.

When conducting hydrodynamic and morphological forecasts of dynamic barrier island systems similar to this study, it is recommended that a sensitivity analysis of hydrodynamic conditions to slight morphological changes is conducted. By studying where the most morphologically dynamic locations are, perturbing them, and analyzing differences in WSE and significant wave height, the level of uncertainty can be quantified for localized areas. For example, a forecast of morphological and hydrodynamic conditions conducted on the Mississippi and Alabama coasts would have very high uncertainty in the locations where differences between DEMs were large (e.g., SE Petit Bois Island, Katrina Cut, West Petit Bois Island, and Pelican Island), and low uncertainty in offshore locations, uniform portions of the mainland coast, and in the northern portion of Mobile Bay.

Further research can be completed to determine decadal or centuries- scale changes in hydrodynamic error in response to simulated DEM updates. The lack of a clear relationship over time between Post-Ivan and XBeach and Post-Ivan and LiDAR DEMs suggests that, 1. Morphological changes to the island are not becoming increasingly different from the Post-Ivan state, and/or, 2. The morphological differences that do occur do not substantially impact hydrodynamics at the points of interest.

CHAPTER 6

CONCLUSIONS

Storm surge presents a major threat to low-lying areas of the NGOM due to the frequency and intensity of TCs, and the low land elevations of this coastline. Under SLR and climate change, storm surge magnitudes (Bilskie, Hagen, Alizad, et al., 2016; Smith et al., 2010) and associated risks (Lindsey, 2022; Mudd et al., 2014) are expected to increase nonlinearly. Barrier islands reduce the wind fetch that acts on the water (Bilskie, Hagen, Alizad, et al., 2016), and physically blocks (Sebastian et al., 2014) the oncoming surge, reducing the maximum potential magnitudes of surge that ultimately reach the mainland. However, these landforms are highly susceptible to storm-induced breaching, overwash, and inundation (Coogan et al., 2019), often because of their low elevations and the high-energy conditions that they encounter. When a barrier island is breaches, decreases in elevation, or otherwise morphologically changes, the flow path and magnitude of storm surge changes (Bilskie et al., 2014). Often, this reduces the amount of protection that they offer the mainland (Rosati & Stone, 2009).

Hindcasting TCs using ADCIRC+SWAN is a reliable and accurate method of representing storm-driven hydrodynamics (Dietrich, Westerink, et al., 2011; Hope et al., 2013; Kerr et al., 2013; Musinguzi et al., 2022). For this study, ten TCs that passed within 200 km of Dauphin or Petit Bois Islands between 2005-2020 were simulated. The model used the ERA5 reanalysis wind product (Hersbach et al., 2020) for the background wind fields, supplemented with GAHM vortex model along the storms' tracks. After each storm, storm-driven morphological change was modeled using XBeach on Petit Bois and Dauphin Islands. Then, dune recovery during the quiescent periods between storms was simulated using the EDGR model. Shoreline changes during the quiescent periods were determined using an empirical equation. The hydrodynamic outputs of the ADCIRC+SWAN simulations run on the Post-Ivan (2004) DEM (Seymour, 2020), the simulated DEM, and contemporary LiDAR data were compared to one another, and to observed data. Simulated DEMs were compared to contemporary LiDAR data.

Barrier islands offer substantial protection to the mainland from threats such as storm surge and wind-driven waves, especially during TCs. Despite the minimal differences in simulated hydrodynamic values when different DEMs were used, all simulations showed a reduction in significant wave height on the back side of the islands. The location and degree of protection varied slightly as storm-driven and quiescent morphological changes occurred in-situ and in simulations; however, the overall trend of mainland protection remained largely the same. Because of the relatively small degree of morphological change, and the distance between the mainland and the islands, the differences in WSE and significant wave heights were minimal, on the order of 5-10 cm.

This 15-year hindcast of TC activity and resultant morphological change represents a short geologic and meteorologic time scale. Therefore, results were likely different than if the study were longer (e.g., 200 years), or during periods with more severe or frequent TC activity (e.g., 2100). Many of the storms simulated were relatively weak on the Saffir-Simpson Wind Scale, and resulted in minimal morphological change, in contrast to Hurricane Katrina (2005), for example. If other storms of similar strength had occurred during the study period, the difference in attenuation abilities over time would have likely been greater than observed for this study. Future studies should focus on longer time-scales, and conduct a forecast of future conditions under various restoration, SLR, and TC intensification scenarios.

Despite the overall lack of extreme hydrodynamic differences caused by morphological change, simulated hydrodynamic conditions (particularly significant wave heights) were very different in the most morphologically dynamic areas (Figure 5.3). Because of the morphological instability in itself, and the vast differences in simulated hydrodynamic conditions at these locations, a larger margin of error and greater uncertainty should be accounted for when designing infrastructure or restoration initiatives. Specifically, because hydrodynamic conditions on the mainland shoreline change by <10 cm, on average, between different DEMs, engineers can expect minimal change in conditions over the following 15 years due to morphological change alone, barring the occurrence of any anomalously intense storms. However, for developers on Dauphin Island, or restoration planners on Dauphin and Petit Bois Islands, a larger margin of error must be accounted for. Even slight differences in elevation inputs can lead to ~0.5-meter differences in simulated significant wave heights; restoration and development designs should account for this level of error, as it is difficult to collect up-to-date elevation data and interpolate them onto the mesh used for the hydrodynamic simulations in enough detail to not introduce some level of error. Overall, greater caution should be taken on the barrier islands than on the mainland.

Because of the increasing storm surge risk and magnitudes on the NGOM coast, it is important to study factors that can mitigate this risk such as barrier islands. However, barrier islands are highly dynamic and susceptible to morphological change, altering their protective abilities. Little research has been done to determine how simulating morphological change between TCs can improve long-term hindcasts. Overall, simulating morphological changes to barrier islands led to noticeable and often large differences in significant wave heights proximate to the most morphologically dynamic locations. Further research is needed to better understand how simulating morphological changes improves agreement to observed hydrodynamic data, and how climate change may impact the region using the methods presented in this study.

REFERENCES

Adams, S., Friedland, C. J., & Levitan, M. L. (2010). *Unmanned Aerial Vehicle Data Acquisition for Damage Assessment in Hurricane Events*. https://www.researchgate.net/publication/228453510

Akbar, M. K., Kanjanda, S., & Musinguzi, A. (2017). Effect of Bottom Friction, Wind Drag Coefficient, and Meteorological Forcing in Hindcast of Hurricane Rita Storm Surge Using SWAN + ADCIRC Model. *Journal of Marine Science and Engineering 2017, Vol. 5, Page 38*, *5*(3), 38. https://doi.org/10.3390/JMSE5030038

Akpınar, A., & Bingölbali, B. (2016). Long-term variations of wind and wave conditions in the coastal regions of the Black Sea. *Natural Hazards*, *84*(1), 69–92. https://doi.org/10.1007/s11069-016-2407-9

Alizad, K., Hagen, S. C., Medeiros, S. C., Bilskie, M. V., Morris, J. T., Balthis, L., & Buckel, C. A. (2018). Dynamic responses and implications to coastal wetlands and the surrounding regions under sea level rise. *PLOS ONE*, *13*(10), e0205176. https://doi.org/10.1371/journal.pone.0205176

Arcement, G., & Schneider, V. (1989). *Guide for selecting Manning's roughness coefficients for natural channels and flood plains* (Vol. 2339). US Government Printing Office.

Bell, B., Hersbach, H., Simmons, A., Berrisford, P., Dahlgren, P., Horányi, A., Muñoz-Sabater, J., Nicolas, J., Radu, R., Schepers, D., Soci, C., Villaume, S., Bidlot, J. R., Haimberger, L., Woollen, J., Buontempo, C., & Thépaut, J. N. (2021). The ERA5 global reanalysis:

Preliminary extension to 1950. *Quarterly Journal of the Royal Meteorological Society*, *147*(741), 4186–4227. https://doi.org/10.1002/QJ.4174

Bilskie, M. V., Asher, T. G., Miller, P. W., Fleming, J. G., Hagen, S. C., & Luettich, R. A. (2022). Real-Time Simulated Storm Surge Predictions during Hurricane Michael (2018). *Weather and Forecasting*, *37*(7), 1085–1102. https://doi.org/10.1175/WAF-D-21-0132.1

Bilskie, M. V., Coggin, D., Hagen, S. C., & Medeiros, S. C. (2015). Terrain-driven unstructured mesh development through semi-automatic vertical feature extraction. *Advances in Water Resources*, *86*, 102–118. https://doi.org/10.1016/J.ADVWATRES.2015.09.020

Bilskie, M. V., Hagen, S. C., Alizad, K., Medeiros, S. C., Passeri, D. L., Needham, H., & Cox, A. (2016). Dynamic simulation and numerical analysis of hurricane storm surge under sea level rise with geomorphologic changes along the northern Gulf of Mexico. *Earth's Future*, *4*(5), 177–193. https://doi.org/10.1002/2015EF000347

Bilskie, M. V., Hagen, S. C., & Medeiros, S. C. (2020). Unstructured finite element mesh decimation for real-time Hurricane storm surge forecasting. *Coastal Engineering*, *156*, 103622. https://doi.org/10.1016/J.COASTALENG.2019.103622

Bilskie, M. V., Hagen, S. C., Medeiros, S. C., Cox, A. T., Salisbury, M., & Coggin, D. (2016). Data and numerical analysis of astronomic tides, wind-waves, and hurricane storm surge along the northern Gulf of Mexico. *Journal of Geophysical Research: Oceans*, *121*(5), 3625–3658. https://doi.org/10.1002/2015JC011400

Bilskie, M. V., Hagen, S. C., Medeiros, S. C., & Passeri, D. L. (2014). Dynamics of sea level rise and coastal flooding on a changing landscape. *Geophysical Research Letters*, *41*(3), 927–934. https://doi.org/10.1002/2013GL058759

Björkqvist, J. V., Vähä-Piikkiö, O., Alari, V., Kuznetsova, A., & Tuomi, L. (2019). WAM, SWAN and WAVEWATCH III in the Finnish archipelago – the effect of spectral performance on bulk wave parameters. *Https://Doi.Org/10.1080/1755876X.2019.1633236*, *13*(1), 55–70. https://doi.org/10.1080/1755876X.2019.1633236

Brown, J. M., Souza, A. J., & Wolf, J. (2010). An 11-year validation of wave-surge modelling in the Irish Sea, using a nested POLCOMS–WAM modelling system. *Ocean Modelling*, *33*(1–2), 118–128. https://doi.org/10.1016/J.OCEMOD.2009.12.006

Buizza, R., Poli, P., Rixen, M., Alonso-Balmaseda, M., Bosilovich, M. G., BrönniMann, S., Compo, G. P., Dee, D. P., Desiato, F., Doutriaux-Boucher, M., Fujiwara, M., Kaiser-Weiss, A. K., Kobayashi, S., Liu, Z., Masina, S., Mathieu, P. P. Pp., Rayner, N., Richter, C., Seneviratne, S. I., … Vaselali, A. (2018). Advancing Global and Regional Reanalyses. *Bulletin of the American Meteorological Society*, *99*(8), ES139–ES144. https://doi.org/10.1175/BAMS-D-17-0312.1

Bunya, S., Dietrich, J. C., Westerink, J. J., Ebersole, B. A., Smith, J. M., Atkinson, J. H., Jensen, R., Resio, D. T., Luettich, R. A., Dawson, C., Cardone, V. J., Cox, A. T., Powell, M. D., Westerink, H. J., & Roberts, H. J. (2010). A High-Resolution Coupled Riverine Flow, Tide, Wind, Wind Wave, and Storm Surge Model for Southern Louisiana and Mississippi. Part I: Model Development and Validation. *Monthly Weather Review*, *138*(2), 345–377. https://doi.org/10.1175/2009MWR2906.1

Chen, Q., Wang, L., & Tawes, R. (2008). Hydrodynamic Response of Northeastern Gulf of Mexico to Hurricanes on JSTOR. *Springer*, *31*(6), 1098–1116. https://www.jstor.org/stable/40663503?seq=1

Cid, A., Castanedo, S., Abascal, A. J., Menéndez, M., & Medina, R. (2014). A high resolution hindcast of the meteorological sea level component for Southern Europe: the GOS dataset.

Climate Dynamics, *43*(7–8), 2167–2184. https://doi.org/10.1007/S00382-013-2041-0/FIGURES/12

Coogan, J., Webb, B., Smallegan, S., & Puleo, J. (2019). Geomorphic changes measured on Dauphin Island, AL, during Hurricane Nate. *Shore & Beach*, 16–22. https://doi.org/10.34237/1008742

CO-OPS Map. (2023). NOAA Tides & Currents. https://tidesandcurrents.noaa.gov/map/index.html?type=TidePredictions&region=

Costanza, R., Pérez-Maqueo, O., Martinez, L. M., Sutton, P., Anderson, S. J., & Mulder, K. (2008). The Value of Coastal Wetlands for Hurricane Protection on JSTOR. *Ambio*, *37*(4), 241–248. https://www.jstor.org/stable/25547893?casa_token=wOucLo7NVnMAAAAA%3AXwG-x_edJTEg6DRZou4thrZ_oK8MsmpL83N91iIuI2nQMZDxApTKuUTvQCmEE5Hzb6PzzzS3EKxNy9mZidsvTnVbVVlGSFaBA3emvgZi4rqoOrTK59o#metadata_info_tab_contents

Cowell, P. J., Stive, M., Niedoroda, A., de Vriend, H., Swift, D. J. P., Kaminsky, G., & Capobianco, M. (2003). The Coastal-Tract (Part 1): A Conceptual Approach to Aggregated Modeling of Low-Order Coastal Change. *Journal of Coastal Research*, *19*, 812–827.

Dalyander, P. S., Mickey, R. C., Passeri, D. L., & Plant, N. G. (2020). Development and application of an empirical dune growth model for evaluating barrier island recovery from storms. *Journal of Marine Science and Engineering*, *8*(12), 1–23. https://doi.org/10.3390/jmse8120977

Danielson, J. J., & Haines, J. (2023). *CoNED*. Coastal National Elevation Database (CoNED) Applications Project.

Davis, J., Mitsova, D., Briggs, T. C., & Roberts, T. (2019). Post-Hurricane Michael damage assessment using ADCIRC storm surge hindcast, image classification, and LiDAR. *Shore & Beach*, *87*(4), 3–14. https://par.nsf.gov/servlets/purl/10302289

Day, J. W., Pont, D., Hensel, P. F., Ibañez, C., & Ibanez, C. (1995). Impacts of Sea-Level Rise on Deltas in the Gulf of Mexico and the Mediterranean: The Importance of Pulsing Events to Sustainability. *Estuaries*, *18*(4), 636. https://doi.org/10.2307/1352382

Dietrich, J. C., Dawson, C. N., Proft, J. M., Howard, M. T., Wells, G., Fleming, J. G., Luettich, R. A., Westerink, J. J., Cobell, Z., Vitse, M., Lander, H., Blanton, B. O., Szpilka, C. M., & Atkinson, J. H. (2013). *Real-Time Forecasting and Visualization of Hurricane Waves and Storm Surge Using SWAN+ADCIRC and FigureGen*. 49–70. https://doi.org/10.1007/978-1-4614-7434-0_3

Dietrich, J. C., Tanaka, S., Westerink, J. J., Dawson, C. N., Luettich, R. A., Zijlema, M., Holthuijsen, L. H., Smith, J. M., Westerink, L. G., & Westerink, H. J. (2011). Performance of the Unstructured-Mesh, SWAN+ADCIRC Model in Computing Hurricane Waves and Surge. *Journal of Scientific Computing 2011 52:2*, *52*(2), 468–497. https://doi.org/10.1007/S10915-011-9555-6

Dietrich, J. C., Westerink, J. J., Kennedy, A. B., Smith, J. M., Jensen, R. E., Zijlema, M., Holthuijsen, L. H., Dawson, C., Luettich, R. A., Powell, M. D., Cardone, V. J., Cox, A. T., Stone, G. W., Pourtaheri, H., Hope, M. E., Tanaka, S., Westerink, L. G., Westerink, H. J., & Cobell, Z. (2011). Hurricane Gustav (2008) Waves and Storm Surge: Hindcast, Synoptic Analysis, and Validation in Southern Louisiana. *Monthly Weather Review*, *139*(8), 2488–2522. https://doi.org/10.1175/2011MWR3611.1

Dietrich, J. C., Woodruff, J., Gorski, J., Knowles, J., & Cuevas Lopez, T. (2022). *SWAN+ADCIRC | Coastal & Computational Hydraulics Team*. North Carolina State University. https://ccht.ccee.ncsu.edu/swanadcirc/

Doran, K. S., Long, J. W., Birchler, J. J., Brenner, O. T., Hardy, M. W., Morgan, K. L. M., Stockdon, H. F., & Torres, M. L. (2017). *Lidar-derived beach morphology (dune crest, dune toe, and shoreline) for U.S. sandy coastlines (ver. 5.0, August 2023): U.S. Geological Survey data release*.

Dullaart, J. C. M., Muis, S., Bloemendaal, N., & Aerts, J. C. J. H. (2020). Advancing global storm surge modelling using the new ERA5 climate reanalysis. *Climate Dynamics*, *54*(1–2), 1007–1021. https://doi.org/10.1007/S00382-019-05044-0

Flood Event Viewer. (2023). USGS. https://stn.wim.usgs.gov/fev/

Frank-Gilchrist, D. P., Passeri, D. L., & Bilskie, M. V. (2023). Hindcast of Hurricane Sally Impacts on Barrier Islands in the Gulf of Mexico. *Coastal Sediments 2023*, 2220–2227. https://doi.org/10.1142/9789811275135_0204

Freer, J., Beven, K. J., Neal, J., Schumann, G., Hall, J., & Bates, P. (2013). Flood risk and uncertainty. In *Risk and Uncertainty Assessment for Natural Hazards* (pp. 190–233). Cambridge University Press. https://doi.org/10.1017/CBO9781139047562.008

Galappatti, G., & Vreugdenhil, C. B. (1985). A depth-integrated model for suspended sediment transport. *Journal of Hydraulic Research*, *23*(4), 359–377. https://doi.org/10.1080/00221688509499345

Gao, J., Luettich, R., Blanton, B., Dietrich, C., Rosman, J., & Bane, J. (2018). ON THE SURFACE WIND STRESS FOR STORM SURGE MODELING. *University of North Carolina- Chapel Hill*, 1–109.

Goff, J. A., Allison, M. A., & Gulick, S. P. S. (2010). Offshore transport of sediment during cyclonic storms: Hurricane Ike (2008), Texas Gulf Coast, USA. *Geology*, *38*(4), 351–354. https://doi.org/10.1130/G30632.1

Grzegorzewski, A. S., Cialone, M., Lansen, A. J., van Ledden, M., Smith, J., & Wamsley, T. (2009). The Influence of Barrier Islands on Hurricane-Generated Storm Surge and Waves in Louisiana and Mississippi. *Coastal Engineering 2008*, 1037–1049. https://doi.org/10.1142/9789814277426_0087

Gutierrez, B. T., Plant, N. G., & Thieler, E. R. (2011). A Bayesian network to predict coastal vulnerability to sea level rise. *Journal of Geophysical Research: Earth Surface*, *116*(F2). https://doi.org/10.1029/2010JF001891

Hanson, J. L., Tracy, B. A., Tolman, H. L., & Scott, R. D. (2009). Pacific Hindcast Performance of Three Numerical Wave Models. *Journal of Atmospheric and Oceanic Technology*, *26*(8), 1614–1633. https://doi.org/10.1175/2009JTECHO650.1

Hersbach, H., Bell, B., Berrisford, P., Hirahara, S., Horányi, A., Muñoz-Sabater, J., Nicolas, J., Peubey, C., Radu, R., Schepers, D., Simmons, A., Soci, C., Abdalla, S., Abellan, X., Balsamo, G., Bechtold, P., Biavati, G., Bidlot, J., Bonavita, M., … Thépaut, J. N. (2020). The ERA5 global reanalysis. *Quarterly Journal of the Royal Meteorological Society*, *146*(730), 1999–2049. https://doi.org/10.1002/QJ.3803

Hope, M. E., Westerink, J. J., Kennedy, A. B., Kerr, P. C., Dietrich, J. C., Dawson, C., Bender, C. J., Smith, J. M., Jensen, R. E., Zijlema, M., Holthuijsen, L. H., Luettich, R. A., Powell, M. D., Cardone, V. J., Cox, A. T., Pourtaheri, H., Roberts, H. J., Atkinson, J. H., Tanaka, S., … Westerink, L. G. (2013). Hindcast and validation of Hurricane Ike (2008) waves, forerunner, and storm surge. *Journal of Geophysical Research: Oceans*, *118*(9), 4424–4460. https://doi.org/10.1002/JGRC.20314

Irish, J. L., Frey, A. E., Rosati, J. D., Olivera, F., Dunkin, L. M., Kaihatu, J. M., Ferreira, C. M., & Edge, B. L. (2010). Potential implications of global warming and barrier island degradation on future hurricane inundation, property damages, and population impacted. *Ocean & Coastal Management*, *53*(10), 645–657. https://doi.org/10.1016/j.ocecoaman.2010.08.001

Irish, J. L., Resio, D. T., & Cialone, M. A. (2009). A surge response function approach to coastal hazard assessment. Part 2: Quantification of spatial attributes of response functions. *Natural Hazards*, *51*(1), 183–205. https://doi.org/10.1007/S11069-009-9381-4/FIGURES/18

Islek, F., Yuksel, Y., Sahin, C., & Guner, H. A. A. (2021). Long-term analysis of extreme wave characteristics based on the SWAN hindcasts over the Black Sea using two different wind fields. *Dynamics of Atmospheres and Oceans*, *94*, 101165. https://doi.org/10.1016/J.DYNATMOCE.2020.101165

Jenkins, R. L., Long, J. W., Dalyander, P. S., Thompson, D. M., Mickey, R. C., & Survey, U. S. G. (2020). Development of a process-based littoral sediment transport model for Dauphin Island, Alabama. In *Open-File Report*. https://doi.org/10.3133/ofr20201011

Jenkins, R. L., Passeri, D. L., Smith, C. G., Thompson, D. M., & Smith, K. E. L. (2023). Modeling the effects of interior headland restoration on estuarine sediment transport processes in a marine-dominant estuary. *Frontiers in Marine Science*, *10*. https://doi.org/10.3389/fmars.2023.1217830

Kerr, P. C., Donahue, A. S., Westerink, J. J., Luettich, R. A., Zheng, L. Y., Weisberg, R. H., Huang, Y., Wang, H. V., Teng, Y., Forrest, D. R., Roland, A., Haase, A. T., Kramer, A. W., Taylor, A. A., Rhome, J. R., Feyen, J. C., Signell, R. P., Hanson, J. L., Hope, M. E., … Cox, A. T. (2013). U.S. IOOS coastal and ocean modeling testbed: Inter-model evaluation of tides, waves, and hurricane surge in the Gulf of Mexico. *Journal of Geophysical Research: Oceans*, *118*(10), 5129–5172. https://doi.org/10.1002/JGRC.20376

Kirk, K., Dusek, G., Tissot, P., & Sweet, W. (2022). An Approach to Approximate Wave Height from Acoustic Tide Gauges. *Journal of Atmospheric and Oceanic Technology*, *39*(6), 721–738. https://doi.org/10.1175/JTECH-D-20-0212.1

Lindsey, R. (2022). *Climate Change: Global Sea Level | NOAA Climate.gov*. https://www.climate.gov/news-features/understanding-climate/climate-change-global-sea-level

Luettich, R. A. (2018). *ADCIRC.org*. UNC Chapel Hill. https://adcirc.org/

Luettich, R. A., Wright, L. D., Signell, R., Friedrichs, C., Friedrichs, M., Harding, J., Fennel, K., Howlett, E., Graves, S., Smith, E., Crane, G., & Baltes, R. (2013). Introduction to special section on The U.S. IOOS Coastal and Ocean Modeling Testbed. *Journal of Geophysical Research: Oceans*, *118*(12), 6319–6328. https://doi.org/10.1002/2013JC008939

McTaggart-Cowan, R., Bosart, L. F., Gyakum, J. R., & Atallah, E. H. (2007). Hurricane Katrina (2005). Part I: Complex Life Cycle of an Intense Tropical Cyclone. *Monthly Weather Review*, *135*(12), 3905–3926. https://doi.org/10.1175/2007MWR1875.1

Menendez, M., García-Díez, M., Fita, L., Fernández, J., Méndez, F. J., & Gutiérrez, J. M. (2014). High-resolution sea wind hindcasts over the Mediterranean area. *Climate Dynamics*, *42*(7–8), 1857–1872. https://doi.org/10.1007/S00382-013-1912-8/FIGURES/9

Merz, B., & Thieken, A. H. (2005). Separating natural and epistemic uncertainty in flood frequency analysis. *Journal of Hydrology*, *309*(1–4), 114–132. https://doi.org/10.1016/J.JHYDROL.2004.11.015

Miller-Way, T. L., Dardeau, M., & Crozier, G. (1996). *Weeks Bay National Estuarine Research Reserve: an estuarine profile and bibliography*.

Model Performance Statistics Definitions. (2017).

Morton, R. A. (2008). Historical Changes in the Mississippi-Alabama Barrier-Island Chain and the Roles of Extreme Storms, Sea Level, and Human Activities. *Journal of Coastal Research*, *24*(6 (246)), 1587–1600. https://doi.org/10.2112/07-0953.1

Mousavi, M. E., Irish, J. L., Frey, A. E., Olivera, F., & Edge, B. L. (2011). Global warming and hurricanes: the potential impact of hurricane intensification and sea level rise on coastal flooding. *Climatic Change*, *104*, 575–597. https://doi.org/10.1007/s10584-009-9790-0

Mudd, L., Asce, S. M., Wang, Y., Asce, M., Letchford, C., Asce, F., & Rosowsky, D. (2014). Assessing Climate Change Impact on the U.S. East Coast Hurricane Hazard: Temperature, Frequency, and Track. *Natural Hazards Review*, *15*(3), 04014001. https://doi.org/10.1061/(ASCE)NH.1527-6996.0000128

Musinguzi, A., Reddy, L., & Akbar, M. K. (2022). Evaluation of Wave Contributions in Hurricane Irma Storm Surge Hindcast. *Atmosphere 2022, Vol. 13, Page 404*, *13*(3), 404. https://doi.org/10.3390/ATMOS13030404

National Data Buoy Center. (2023). US Department of Commerce- NOAA NWS.

National Hurricane Center. (2022, July 27). https://www.nhc.noaa.gov/

Needham, H., & Keim, B. D. (2011). Storm Surge: Physical Processes and an Impact Scale. In A. Lupo (Ed.), *Recent Hurricane Research- Climate, Dynamics, and Societal Impacts* (pp. 385–406). InTech. www.intechopen.com

Needham, H., Keim, B. D., & Sathiaraj, D. (2015). A review of tropical cyclone-generated storm surges: Global data sources, observations, and impacts. *Reviews of Geophysics*, *53*(2), 545–591. https://doi.org/10.1002/2014RG000477

Niedoroda, A. W., Resio, D. T., Toro, G. R., Divoky, D., Das, H. S., & Reed, C. W. (2010). Analysis of the coastal Mississippi storm surge hazard. *Ocean Engineering*, *37*(1), 82–90. https://doi.org/10.1016/J.OCEANENG.2009.08.019

Olauson, J. (2018). ERA5: The new champion of wind power modelling? *Renewable Energy*, *126*, 322–331. https://doi.org/10.1016/J.RENENE.2018.03.056

Onea, F., & Rusu, L. (2017). A Long-Term Assessment of the Black Sea Wave Climate. *Sustainability 2017, Vol. 9, Page 1875*, *9*(10), 1875. https://doi.org/10.3390/SU9101875

Passeri, D. L., Bilskie, M. V., Hagen, S. C., Mickey, R. C., Dalyander, P. S., & Gonzalez, V. M. (2021). Assessing the Effectiveness of Nourishment in Decadal Barrier Island Morphological Resilience. *Water*, *13*(7), 944. https://doi.org/10.3390/w13070944

Passeri, D. L., Bilskie, M. V., Plant, N. G., Long, J. W., & Hagen, S. C. (2018). Dynamic modeling of barrier island response to hurricane storm surge under future sea level rise. *Climatic Change*, *149*(3–4), 413–425. https://doi.org/10.1007/s10584-018-2245-8

Passeri, D. L., Dalyander, P. S., Long, J. W., Mickey, R. C., Jenkins, R. L., Thompson, D. M., Plant, N. G., Godsey, E. S., & Gonzalez, V. M. (2020). The Roles of Storminess and Sea Level Rise in Decadal Barrier Island Evolution. *Geophysical Research Letters*, *47*(18), e2020GL089370. https://doi.org/10.1029/2020GL089370

Passeri, D. L., Hagen, S. C., Bilskie, M. V., & Medeiros, S. C. (2015). On the significance of incorporating shoreline changes for evaluating coastal hydrodynamics under sea level rise scenarios. *Natural Hazards*, *75*(2), 1599–1617. https://doi.org/10.1007/s11069-014-1386-y

Passeri, D. L., Hagen, S. C., Medeiros, S. C., & Bilskie, M. V. (2015). Impacts of historic morphology and sea level rise on tidal hydrodynamics in a microtidal estuary (Grand Bay, Mississippi). *Continental Shelf Research*, *111*, 150–158. https://doi.org/10.1016/J.CSR.2015.08.001

Passeri, D. L., Hagen, S. C., Plant, N. G., Bilskie, M. V., Medeiros, S. C., & Alizad, K. (2016). Tidal hydrodynamics under future sea level rise and coastal morphology in the Northern Gulf of Mexico. *Earth's Future*, *4*(5), 159–176. https://doi.org/10.1002/2015EF000332

Passeri, D. L., Long, J. W., Plant, N. G., Bilskie, M. V., & Hagen, S. C. (2018). The influence of bed friction variability due to land cover on storm-driven barrier island morphodynamics. *Coastal Engineering*, *132*, 82–94. https://doi.org/10.1016/j.coastaleng.2017.11.005

Plant, N. G., Robert Thieler, E., & Passeri, D. L. (2016). Coupling centennial-scale shoreline change to sea-level rise and coastal morphology in the Gulf of Mexico using a Bayesian network. *Earth's Future*, *4*(5), 143–158. https://doi.org/10.1002/2015EF000331

Purvis, M. J., Bates, P. D., & Hayes, C. M. (2008). A probabilistic methodology to estimate future coastal flood risk due to sea level rise. *Coastal Engineering*, *55*(12), 1062–1073. https://doi.org/10.1016/J.COASTALENG.2008.04.008

Resio, D. T., Irish, J., & Cialone, M. (2009). A surge response function approach to coastal hazard assessment - Part 1: Basic concepts. *Natural Hazards*, *51*(1), 163–182. https://doi.org/10.1007/S11069-009-9379-Y

Resio, D. T., & Irish, J. L. (2015). Tropical Cyclone Storm Surge Risk. *Current Climate Change Reports*, 74–84. https://doi.org/https://doi.org/10.1007/s40641-015-0011-9

Resio, D. T., Irish, J. L., Westerink, J. J., & Powell, N. J. (2013). The effect of uncertainty on estimates of hurricane surge hazards. *Natural Hazards*, *66*(3), 1443–1459. https://doi.org/10.1007/S11069-012-0315-1/FIGURES/5

Resio, D. T., J. Powell, N., A. Cialone, M., Das, H. S., & Westerink, J. J. (2017). Quantifying impacts of forecast uncertainties on predicted storm surges. *Natural Hazards*, *88*(3), 1423–1449. https://doi.org/10.1007/S11069-017-2924-1/FIGURES/12

Resio, D. T., & Westerink, J. J. (2008). Modeling the physics of storm surges. *Physics Today*, *61*(9), 33. https://doi.org/10.1063/1.2982120

Rosati, J. D., & Stone, G. W. (2009). Geomorphologic Evolution of Barrier Islands along the Northern U.S. Gulf of Mexico and Implications for Engineering Design in Barrier Restoration. *Journal of Coastal Research*, *25*(1), 8–22. https://doi.org/10.2112/07-0934.1

Rusu, L., Pilar, P., & Guedes Soares, C. (2008). Hindcast of the wave conditions along the west Iberian coast. *Coastal Engineering*, *55*(11), 906–919. https://doi.org/10.1016/J.COASTALENG.2008.02.029

Saffir-Simpson Hurricane Wind Scale. (2012). National Hurricane Center. https://www.nhc.noaa.gov/aboutsshws.php

Sallenger, A. H. Jr. (2000). Storm Impact Scale for Barrier Islands. *Journal of Coastal Research*, *16*(3), 890–895.

Sebastian, A., Proft, J., Dietrich, J. C., Du, W., Bedient, P. B., & Dawson, C. N. (2014). Characterizing hurricane storm surge behavior in Galveston Bay using the

SWAN + ADCIRC model. *Coastal Engineering*, *88*, 171–181. https://doi.org/10.1016/J.COASTALENG.2014.03.002

Seim, H. E., Kjerfve, B., & Sneed, J. E. (1987). Tides of Mississippi Sound and the adjacent continental shelf. *Estuarine, Coastal and Shelf Science*, *25*(2), 143–156. https://doi.org/10.1016/0272-7714(87)90118-1

Seymour, A. (2020). *Petit Bois and Dauphin Island Point Cloud Filtering and DEM Fusion*.

Smith, J. M., Cialone, M. A., Wamsley, T. V., & McAlpin, T. O. (2010). Potential impact of sea level rise on coastal surges in southeast Louisiana. *Ocean Engineering*, *37*(1), 37–47. https://doi.org/10.1016/j.oceaneng.2009.07.008

Sotillo, M. G., Ratsimandresy, A. W., Carretero, J. C., Bentamy, A., Valero, F., & González-Rouco, F. (2005). A high-resolution 44-year atmospheric hindcast for the Mediterranean Basin: Contribution to the regional improvement of global reanalysis. *Climate Dynamics*, *25*(2–3), 219–236. https://doi.org/10.1007/S00382-005-0030-7/FIGURES/11

Surge Database Console. (2018). Louisiana State University. https://surgedat.climate.lsu.edu/surge/

Swain, J. (1997). *Simulation of Wave Climate for the Arabian Sea and Bay of Bengal*.

Taylor, N. R., Irish, J. L., Udoh, I. E., Bilskie, M. V., & Hagen, S. C. (2015). Development and uncertainty quantification of hurricane surge response functions for hazard assessment in coastal bays. *Natural Hazards*, *77*(2), 1103–1123. https://doi.org/10.1007/S11069-015-1646-5/TABLES/3

Teng, J., Jakeman, A. J., Vaze, J., Croke, B. F. W., Dutta, D., & Kim, S. (2017). Flood inundation modelling: A review of methods, recent advances and uncertainty analysis.

Environmental Modelling & Software, *90*, 201–216. https://doi.org/10.1016/J.ENVSOFT.2017.01.006

Valmassoi, A., Keller, J. D., Kleist, D. T., English, S., Ahrens, B., Ďurán, I. B., Bauernschubert, E., Bosilovich, M. G., Fujiwara, M., Hersbach, H., Lei, L., Löhnert, U., Mamnun, N., Martin, C. R., Moore, A., Niermann, D., Ruiz, J. J., & Scheck, L. (2022). Current challenges and future directions in data assimilation and reanalysis. *Bulletin of the American Meteorological Society*, *1*(aop). https://doi.org/10.1175/BAMS-D-21-0331.1

Vuik, V., Jonkman, S. N., Borsje, B. W., & Suzuki, T. (2016). Nature-based flood protection: The efficiency of vegetated foreshores for reducing wave loads on coastal dikes. *Coastal Engineering*, *116*, 42–56. https://doi.org/10.1016/J.COASTALENG.2016.06.001

Wamsley, T. V., Cialone, M. A., Smith, J. M., Atkinson, J. H., & Rosati, J. D. (2010). The potential of wetlands in reducing storm surge. *Ocean Engineering*, *37*(1), 59–68. https://doi.org/10.1016/j.oceaneng.2009.07.018

Wang, S., McGrath, R., Hanafin, J., Lynch, P., Semmler, T., & Nolan, P. (2008). The impact of climate change on storm surges over Irish waters. *Ocean Modelling*, *25*(1–2), 83–94. https://doi.org/10.1016/J.OCEMOD.2008.06.009

Wang, Y., Mao, X., & Jiang, W. (2018). Long-term hazard analysis of destructive storm surges using the ADCIRC- SWAN model: A case study of Bohai Sea, China. *International Journal of Applied Earth Observation and Geoinformation*, *73*, 52–62. https://doi.org/10.1016/J.JAG.2018.03.013

Weaver, R. J., & Luettich, R. A. (2010). 2D vs. 3D Storm Surge Sensitivity in ADCIRC: Case Study of Hurricane Isabel. *Proceedings of the International Conference on Estuarine and Coastal Modeling*, *388*, 762–779. https://doi.org/10.1061/41121(388)44

Welander, P. (1961). Numerical Prediction of Storm Surges. *Advances in Geophysics*, *8*(C), 315–379. https://doi.org/10.1016/S0065-2687(08)60343-X

Westerink, J. J., Luettich, R. A., Feyen, J. C., Atkinson, J. H., Dawson, C., Roberts, H. J., Powell, M. D., Dunion, J. P., Kubatko, E. J., & Pourtaheri, H. (2008). A Basin- to Channel-Scale Unstructured Grid Hurricane Storm Surge Model Applied to Southern Louisiana. *Monthly Weather Review*, *136*(3), 833–864. https://doi.org/10.1175/2007MWR1946.1

Zerger, A., Smith, D. I., Hunter, G. J., & Jones, S. D. (2002). Riding the storm: A comparison of uncertainty modelling techniques for storm surge risk management. *Applied Geography*, *22*(3), 307–330. https://doi.org/10.1016/S0143-6228(02)00010-3

APPENDICES

APPENDIX A: WAVE STATISTICS

TABLE A.1: Front side of islands

Significant Wave Height - Front side of Islands								
Storm	Station no.	DEMs	p-value		Storm	Station no.	DEMs	p-value
Cindy	1	Post-Ivan and XBeach	0.012		Alberto	1	Post-Ivan and XBeach	0.047
Dennis	1	Post-Ivan and XBeach	0.000		Alberto	1	XBeach and LiDAR	0.011
Dennis	15	Post-Ivan and XBeach	0.006		Gordon	1	Post-Ivan and XBeach	0.000
Dennis	16	Post-Ivan and XBeach	0.009		Gordon	1	XBeach and LiDAR	0.000
Katrina	1	Post-Ivan and XBeach	0.016		Gordon	18	Post-Ivan and XBeach	0.001
Katrina	15	Post-Ivan and XBeach	0.049		Gordon	18	XBeach and LiDAR	0.016
Ida	1	Post-Ivan and XBeach	0.000		Cristobal	1	Post-Ivan and XBeach	0.001
Ida	1	XBeach and LiDAR	0.000		Cristobal	1	Post-Ivan and LiDAR	0.033
Ida	14	XBeach and LiDAR	0.029		Cristobal	1	XBeach and LiDAR	0.000
Ida	15	Post-Ivan and XBeach	0.013		Cristobal	3	Post-Ivan and XBeach	0.008
Ida	15	XBeach and LiDAR	0.022		Cristobal	3	XBeach and LiDAR	0.007
Ida	23	XBeach and LiDAR	0.036		Cristobal	14	Post-Ivan and LiDAR	0.024
Nate	1	Post-Ivan and XBeach	0.000		Cristobal	14	XBeach and LiDAR	0.018
Nate	1	Post-Ivan and LiDAR	0.000		Cristobal	15	Post-Ivan and XBeach	0.028
Nate	1	XBeach and LiDAR	0.000		Cristobal	15	XBeach and LiDAR	0.036
Nate	2	Post-Ivan and LiDAR	0.000		Sally	1	Post-Ivan and XBeach	0.000
Nate	2	XBeach and LiDAR	0.000		Sally	2	XBeach and LiDAR	0.000
Nate	15	Post-Ivan and XBeach	0.000		Sally	3	XBeach and LiDAR	0.044
Nate	15	XBeach and LiDAR	0.000		Sally	14	Post-Ivan and LiDAR	0.020
Nate	16	Post-Ivan and XBeach	0.000		Sally	14	XBeach and LiDAR	0.011
Nate	16	Post-Ivan and LiDAR	0.000		Sally	15	Post-Ivan and XBeach	0.006
Nate	17	Post-Ivan and XBeach	0.005		Sally	15	XBeach and LiDAR	0.009
Nate	17	XBeach and LiDAR	0.047		Sally	16	Post-Ivan and XBeach	0.004
Nate	18	Post-Ivan and XBeach	0.000		Sally	16	XBeach and LiDAR	0.001
Nate	18	Post-Ivan and LiDAR	0.008		Sally	18	Post-Ivan and XBeach	0.038
Nate	21	XBeach and LiDAR	0.008		Sally	23	Post-Ivan and XBeach	0.024
Nate	23	Post-Ivan and XBeach	0.002		Sally	23	XBeach and LiDAR	0.024
Nate	23	XBeach and LiDAR	0.001					

TABLE A.2: Significant wave height for back side of islands

Significant Wave Height - Back side of Islands								
Storm	Station no.	DEMs	p-value		Storm	Station no.	DEMs	p-value
Cindy	28	Post-Ivan and XBeach	0.008		Alberto	29	Post-Ivan and XBeach	0.008
Cindy	29	Post-Ivan and XBeach	0.004		Alberto	29	Post-Ivan and LiDAR	0.034
Cindy	30	Post-Ivan and XBeach	0.003		Alberto	30	Post-Ivan and XBeach	0.004
Cindy	31	Post-Ivan and XBeach	0.003		Alberto	31	Post-Ivan and XBeach	0.007
Cindy	32	Post-Ivan and XBeach	0.009		Alberto	32	Post-Ivan and XBeach	0.032
Dennis	27	Post-Ivan and XBeach	0.002		Gordon	27	Post-Ivan and XBeach	0.002
Dennis	28	Post-Ivan and XBeach	0.000		Gordon	27	Post-Ivan and LiDAR	0.006
Dennis	29	Post-Ivan and XBeach	0.000		Gordon	28	Post-Ivan and XBeach	0.000
Dennis	30	Post-Ivan and XBeach	0.000		Gordon	28	Post-Ivan and LiDAR	0.001
Dennis	31	Post-Ivan and XBeach	0.000		Gordon	29	Post-Ivan and XBeach	0.000
Dennis	32	Post-Ivan and XBeach	0.000		Gordon	29	Post-Ivan and LiDAR	0.001
Dennis	33	Post-Ivan and XBeach	0.005		Gordon	30	Post-Ivan and XBeach	0.000
Ida	27	Post-Ivan and XBeach	0.023		Gordon	30	Post-Ivan and LiDAR	0.004
Ida	28	Post-Ivan and XBeach	0.003		Gordon	31	Post-Ivan and XBeach	0.001
Ida	28	XBeach and LiDAR	0.005		Gordon	31	Post-Ivan and LiDAR	0.014
Ida	29	Post-Ivan and XBeach	0.003		Gordon	32	Post-Ivan and XBeach	0.013
Ida	29	XBeach and LiDAR	0.011		Cristobal	15	Post-Ivan and LiDAR	0.006
Ida	30	Post-Ivan and XBeach	0.004		Cristobal	15	XBeach and LiDAR	0.000
Ida	30	XBeach and LiDAR	0.022		Cristobal	27	Post-Ivan and XBeach	0.001
Ida	31	Post-Ivan and XBeach	0.008		Cristobal	27	Post-Ivan and LiDAR	0.001
Ida	31	XBeach and LiDAR	0.028		Cristobal	28	Post-Ivan and XBeach	0.000
Ida	32	Post-Ivan and XBeach	0.035		Cristobal	28	Post-Ivan and LiDAR	0.000
Nate	15	XBeach and LiDAR	0.001		Cristobal	29	Post-Ivan and XBeach	0.000
Nate	27	Post-Ivan and XBeach	0.000		Cristobal	29	Post-Ivan and LiDAR	0.000
Nate	27	Post-Ivan and LiDAR	0.000		Cristobal	30	Post-Ivan and XBeach	0.000
Nate	28	Post-Ivan and XBeach	0.000		Cristobal	30	Post-Ivan and LiDAR	0.000
Nate	28	Post-Ivan and LiDAR	0.000		Cristobal	31	Post-Ivan and XBeach	0.000
Nate	29	Post-Ivan and XBeach	0.000		Cristobal	31	Post-Ivan and LiDAR	0.000
Nate	29	Post-Ivan and LiDAR	0.000		Cristobal	32	Post-Ivan and XBeach	0.000
Nate	30	Post-Ivan and XBeach	0.000		Cristobal	32	Post-Ivan and LiDAR	0.000
Nate	30	Post-Ivan and LiDAR	0.000		Cristobal	33	Post-Ivan and XBeach	0.003
Nate	30	XBeach and LiDAR	0.017		Cristobal	33	Post-Ivan and LiDAR	0.012
Nate	31	Post-Ivan and XBeach	0.000		Sally	2	Post-Ivan and LiDAR	0.005
Nate	31	Post-Ivan and LiDAR	0.001		Sally	2	XBeach and LiDAR	0.002
Nate	31	XBeach and LiDAR	0.035		Sally	27	Post-Ivan and XBeach	0.048
Nate	32	Post-Ivan and XBeach	0.000		Sally	28	Post-Ivan and XBeach	0.008
Nate	32	Post-Ivan and LiDAR	0.014		Sally	29	Post-Ivan and XBeach	0.006
Nate	33	Post-Ivan and XBeach	0.006		Sally	30	Post-Ivan and XBeach	0.007
Alberto	28	Post-Ivan and XBeach	0.014		Sally	31	Post-Ivan and XBeach	0.018
Alberto	28	Post-Ivan and LiDAR	0.031					

TABLE A.3: Mean and peak wave period

Wave period - Front side of Islands										
Storm	Mean or Peak	Station no.	DEMs	p-value		Storm	Mean or Peak	Station no.	DEMs	p-value
Katrina	Peak	5	Post-Ivan and XBeach	0.015		Katrina	Peak	31	Post-Ivan and XBeach	0.003
Katrina	Peak	6	Post-Ivan and XBeach	0.015		Katrina	Peak	32	Post-Ivan and XBeach	0.003
Katrina	Peak	7	Post-Ivan and XBeach	0.015		Katrina	Peak	33	Post-Ivan and XBeach	0.009
Katrina	Peak	8	Post-Ivan and XBeach	0.009		Katrina	Peak	34	Post-Ivan and XBeach	0.009
Katrina	Peak	9	Post-Ivan and XBeach	0.009		Katrina	Peak	35	Post-Ivan and XBeach	0.009
Katrina	Peak	10	Post-Ivan and XBeach	0.005		Katrina	Peak	36	Post-Ivan and XBeach	0.009
Katrina	Peak	11	Post-Ivan and XBeach	0.005		Katrina	Peak	37	Post-Ivan and XBeach	0.003
Katrina	Peak	12	Post-Ivan and XBeach	0.005		Katrina	Peak	38	Post-Ivan and XBeach	0.003
Katrina	Peak	13	Post-Ivan and XBeach	0.009		Katrina	Peak	39	Post-Ivan and XBeach	0.003
Katrina	Peak	14	Post-Ivan and XBeach	0.048		Katrina	Peak	40	Post-Ivan and XBeach	0.003
Katrina	Peak	15	Post-Ivan and XBeach	0.047		Katrina	Peak	41	Post-Ivan and XBeach	0.003
Katrina	Peak	17	Post-Ivan and XBeach	0.015		Katrina	Peak	42	Post-Ivan and XBeach	0.003
Katrina	Peak	18	Post-Ivan and XBeach	0.014		Katrina	Peak	43	Post-Ivan and XBeach	0.003
Katrina	Peak	19	Post-Ivan and XBeach	0.009		Katrina	Peak	44	Post-Ivan and XBeach	0.003
Katrina	Peak	20	Post-Ivan and XBeach	0.015		Alberto	Peak	1	Post-Ivan and XBeach	0.027
Katrina	Peak	21	Post-Ivan and XBeach	0.003		Alberto	Peak	1	XBeach and LiDAR	0.048
Katrina	Peak	22	Post-Ivan and XBeach	0.003		Alberto	Peak	4	Post-Ivan and XBeach	0.027
Katrina	Peak	23	Post-Ivan and XBeach	0.003		Alberto	Peak	4	XBeach and LiDAR	0.048
Katrina	Peak	24	Post-Ivan and XBeach	0.003		Alberto	Peak	5	Post-Ivan and XBeach	0.027
Katrina	Peak	25	Post-Ivan and XBeach	0.003		Alberto	Peak	5	XBeach and LiDAR	0.048
Katrina	Peak	26	Post-Ivan and XBeach	0.003		Nate	Mean	16	Post-Ivan and LiDAR	0.018
Katrina	Peak	27	Post-Ivan and XBeach	0.003		Nate	Mean	16	XBeach and LiDAR	0.034
Katrina	Peak	28	Post-Ivan and XBeach	0.003		Nate	Mean	44	Post-Ivan and LiDAR	0.042
Katrina	Peak	29	Post-Ivan and XBeach	0.003		Sally	Mean	16	XBeach and LiDAR	0.016
Katrina	Peak	30	Post-Ivan and XBeach	0.003						

TABLE A.4: Wave direction

Wave Direction - Front side of Islands								
Storm	Station no.	DEMs	p-value		Storm	Station no.	DEMs	p-value
Cindy	1	Post-Ivan and XBeach	0.000		Gordon	1	Post-Ivan and XBeach	0.000
Cindy	4	Post-Ivan and XBeach	0.001		Gordon	1	Post-Ivan and LiDAR	0.002
Cindy	15	Post-Ivan and XBeach	0.009		Gordon	1	XBeach and LiDAR	0.000
Cindy	16	Post-Ivan and XBeach	0.000		Gordon	2	Post-Ivan and XBeach	0.004
Cindy	18	Post-Ivan and XBeach	0.001		Gordon	2	XBeach and LiDAR	0.000
Cindy	21	Post-Ivan and XBeach	0.000		Gordon	3	XBeach and LiDAR	0.035
Dennis	1	Post-Ivan and XBeach	0.000		Gordon	4	Post-Ivan and XBeach	0.004
Dennis	2	Post-Ivan and XBeach	0.006		Gordon	4	XBeach and LiDAR	0.008
Dennis	4	Post-Ivan and XBeach	0.000		Gordon	5	Post-Ivan and LiDAR	0.029
Dennis	15	Post-Ivan and XBeach	0.005		Gordon	9	Post-Ivan and LiDAR	0.040
Dennis	16	Post-Ivan and XBeach	0.000		Gordon	10	Post-Ivan and LiDAR	0.034
Dennis	18	Post-Ivan and XBeach	0.000		Gordon	11	XBeach and LiDAR	0.006
Dennis	21	Post-Ivan and XBeach	0.000		Gordon	15	Post-Ivan and XBeach	0.030
Katrina	1	Post-Ivan and XBeach	0.000		Gordon	15	XBeach and LiDAR	0.004
Katrina	4	Post-Ivan and XBeach	0.019		Gordon	16	Post-Ivan and XBeach	0.000
Katrina	16	Post-Ivan and XBeach	0.000		Gordon	16	Post-Ivan and LiDAR	0.000
Katrina	18	Post-Ivan and XBeach	0.000		Gordon	16	XBeach and LiDAR	0.000
Katrina	21	Post-Ivan and XBeach	0.001		Gordon	18	Post-Ivan and XBeach	0.003
Ida	1	Post-Ivan and XBeach	0.001		Gordon	18	Post-Ivan and LiDAR	0.001
Ida	1	XBeach and LiDAR	0.000		Gordon	21	Post-Ivan and XBeach	0.000
Ida	2	Post-Ivan and XBeach	0.013		Gordon	21	XBeach and LiDAR	0.000
Ida	11	XBeach and LiDAR	0.017		Gordon	23	Post-Ivan and XBeach	0.000
Ida	14	Post-Ivan and LiDAR	0.047		Gordon	23	XBeach and LiDAR	0.000
Ida	15	XBeach and LiDAR	0.001		Cristobal	1	Post-Ivan and XBeach	0.000
Ida	16	Post-Ivan and XBeach	0.000		Cristobal	1	Post-Ivan and LiDAR	0.000
Ida	16	XBeach and LiDAR	0.000		Cristobal	1	XBeach and LiDAR	0.000
Ida	18	Post-Ivan and XBeach	0.007		Cristobal	2	Post-Ivan and XBeach	0.000
Ida	18	Post-Ivan and LiDAR	0.039		Cristobal	2	Post-Ivan and LiDAR	0.004
Ida	18	XBeach and LiDAR	0.000		Cristobal	2	XBeach and LiDAR	0.000
Ida	21	Post-Ivan and XBeach	0.001		Cristobal	4	Post-Ivan and XBeach	0.000
Ida	21	XBeach and LiDAR	0.016		Cristobal	4	XBeach and LiDAR	0.000
Nate	1	Post-Ivan and XBeach	0.000		Cristobal	5	Post-Ivan and LiDAR	0.046
Nate	1	Post-Ivan and LiDAR	0.000		Cristobal	11	XBeach and LiDAR	0.023
Nate	1	XBeach and LiDAR	0.000		Cristobal	15	XBeach and LiDAR	0.037
Nate	2	Post-Ivan and XBeach	0.000		Cristobal	16	Post-Ivan and XBeach	0.000
Nate	2	XBeach and LiDAR	0.000		Cristobal	16	Post-Ivan and LiDAR	0.009
Nate	4	Post-Ivan and XBeach	0.000		Cristobal	16	XBeach and LiDAR	0.000

Wave Direction - Front side of Islands (continued)

Storm	Station no.	DEMs	p-value		Storm	Station no.	DEMs	p-value
Nate	4	XBeach and LiDAR	0.000		Cristobal	18	Post-Ivan and LiDAR	0.002
Nate	5	Post-Ivan and XBeach	0.018		Cristobal	20	Post-Ivan and LiDAR	0.001
Nate	5	Post-Ivan and LiDAR	0.000		Cristobal	20	XBeach and LiDAR	0.003
Nate	8	Post-Ivan and XBeach	0.046		Cristobal	21	Post-Ivan and XBeach	0.000
Nate	9	Post-Ivan and LiDAR	0.023		Cristobal	21	XBeach and LiDAR	0.000
Nate	10	Post-Ivan and LiDAR	0.005		Sally	1	Post-Ivan and XBeach	0.000
Nate	10	XBeach and LiDAR	0.043		Sally	1	XBeach and LiDAR	0.000
Nate	11	XBeach and LiDAR	0.000		Sally	3	Post-Ivan and XBeach	0.000
Nate	12	Post-Ivan and LiDAR	0.021		Sally	3	XBeach and LiDAR	0.000
Nate	13	Post-Ivan and LiDAR	0.049		Sally	16	Post-Ivan and XBeach	0.000
Nate	15	Post-Ivan and XBeach	0.014		Sally	16	Post-Ivan and LiDAR	0.002
Nate	15	XBeach and LiDAR	0.001		Sally	16	XBeach and LiDAR	0.000
Nate	16	Post-Ivan and XBeach	0.000		Sally	17	Post-Ivan and XBeach	0.001
Nate	16	Post-Ivan and LiDAR	0.000		Sally	17	XBeach and LiDAR	0.001
Nate	16	XBeach and LiDAR	0.000		Sally	18	Post-Ivan and XBeach	0.036
Nate	18	Post-Ivan and LiDAR	0.000		Sally	18	XBeach and LiDAR	0.033
Nate	18	XBeach and LiDAR	0.000		Sally	21	Post-Ivan and XBeach	0.015
Nate	21	Post-Ivan and XBeach	0.000		Sally	21	XBeach and LiDAR	0.010
Alberto	1	Post-Ivan and XBeach	0.035					
Alberto	1	XBeach and LiDAR	0.002					
Alberto	3	Post-Ivan and XBeach	0.016					
Alberto	3	XBeach and LiDAR	0.021					